



Search for gauge-mediated supersymmetry in events with photons and a Z boson at CMS

von

Sebastian Wuchterl

Masterarbeit in Physik

vorgelegt der

Fakultät für Mathematik, Informatik und Naturwissenschaften der
RWTH Aachen

im

November 2018

angefertigt im

I. Physikalischen Institut B

bei

Gutachter: Prof. Dr. Lutz Feld

Zweitgutachter: Prof. Dr. Thomas Hebbeker

Contents

1. Introduction	5
2. Theoretical introduction and motivation	7
2.1. System of units	7
2.2. The standard model of particle physics	7
2.3. Supersymmetry	10
2.3.1. General Gauge Mediation	13
2.3.2. Signal scenarios	13
2.3.3. Status of SUSY searches at the Large Hadron Collider	15
3. The experiment	19
3.1. The Large Hadron Collider	19
3.2. The Compact Muon Solenoid	21
3.2.1. The tracker system	22
3.2.2. The electromagnetic calorimeter	22
3.2.3. The hadron calorimeter	24
3.2.4. The solenoid magnet	24
3.2.5. The muon system	24
3.2.6. The trigger system	25
4. Simulation, data processing, and event reconstruction	27
4.1. Data sets	28
4.2. Monte-Carlo simulation	28
4.3. Event reconstruction and particle identification	30
4.3.1. Particle flow	31
4.3.2. Primary vertex and quality requirements	32
4.3.3. Muons	32
4.3.4. Electrons	33
4.3.5. Photons	33
4.3.6. Jets	34

4.4. Definition of observables	35
4.5. Lepton pair selection	36
4.6. Triggers and trigger efficiency measurement	37
5. Analysis strategy and background estimation	41
5.1. Event selection	41
5.1.1. Preselection	41
5.1.2. Signal region	42
5.1.3. Control regions	42
5.1.4. Validation region	44
5.2. Background estimation	45
5.2.1. Top pair production	49
5.2.2. WZ diboson production	51
5.2.3. ZZ diboson production	51
5.2.4. Drell-Yan and $Z\gamma$ production	52
5.2.5. Other standard model backgrounds	54
5.2.6. Validation of the background estimation	55
5.2.7. Signal contamination	57
5.3. Study of systematic uncertainties	58
5.3.1. Background uncertainties	58
5.3.2. Signal uncertainties	59
6. Results and interpretation	61
6.1. Results	61
6.2. Statistical interpretation	63
6.2.1. Limit calculation	65
6.2.2. Exclusion limits	66
7. Summary & Conclusion	69
Bibliography	71
A. Data sets	81
B. Simulated data sets	83
C. Signal properties	85
D. Trigger paths	89

Introduction

The understanding of the world around us is one of the main reasons for science. Driven by the urge for knowledge and striving to combine all observed phenomena in a unified description gave rise to more and more successful and comprehensive models in all fields of physics.

The state-of-the-art understanding in particles physics is characterized by the standard model (SM), which describes all observations in high energy particle physics successfully. Essential parameters of the SM have been studied at particle accelerators for years with very high precision. It provides a combined description of three of the four fundamental forces and a classification of all building blocks of matter. The most recent remarkable success of the standard model is the observation of a Higgs boson in 2012 [1–3]. Since then, the properties and couplings of the Higgs boson have been studied also with great interest and effort.

Nevertheless, the SM is not capable of explaining various physical observations, such as the existence of neutrino masses or the origin of dark matter. Several theoretical extensions to the SM could supply answers to the different shortcomings. Driven by the attractive concept of symmetry [4] with regard to the theory, one possible solution is supersymmetry (SUSY). SUSY postulates partner particles to each particle of the SM, introducing a symmetry between fermions and bosons, although the supersymmetric partners must be much heavier in mass compared to their SM equivalents.

Bigger and more complex, and such more expensive, experiments are needed to study elementary particles at the high energy frontier. The currently largest and most powerful particle accelerator is the Large Hadron Collider (LHC) at CERN near Geneva. Here, billions of protons are accelerated to almost the speed of light and are collided every second. The large amount of data arising thereby is recorded with the Compact Muon Solenoid (CMS) detector located at one of the four collision points of the LHC. The data sample being analyzed in this thesis consists of events recorded in 2016 based on proton-proton collisions with a center-of-mass energy of 13 TeV. CMS shows an excellent performance with regard to event reconstruction and particle identification, based on the combined reconstruction from all CMS subdetectors, such as the tracking system, the electromagnetic and hadronic calorimeters, and the muon system.

Supersymmetric particles are expected to have masses that might be accessible at the LHC. In order to differentiate between the masses of the SM particles and their partners, a symmetry breaking mechanism needs to be introduced. One scenario is gauge-mediated supersymmetry breaking (GMSB), where the second lightest supersymmetric particle is expected to decay to SM bosons, such as the Z boson and the photon, and the lightest supersymmetric particle (LSP), which is the gravitino (\tilde{G}). The LSP is supposed to be undetectable, thus leading to an imbal-

ance in the measured transverse momentum sum, called missing transverse momentum. These theoretical models are mainly motivating the presented search.

Searches for SUSY with photons in the final states have been carried out using the 2016 data set [5–8], but in this thesis a new independent final state is investigated, complementing the existing searches. By targeting events with photons, a Z boson decaying to charged leptons, and missing transverse momentum, the search is sensitive to various production channels for SUSY particles. It is also able to study phase space regions, where not so much energy is transferred to the final state particles due to low requirements on the lepton and photon momenta.

The analyzed data set is based on events where at least two same-flavor opposite-charge leptons are reconstructed, being a part of the total 2016 data set corresponding to a total integrated luminosity of 35.9 fb^{-1} .

Standard model processes leading to the same final state are considered as background throughout this thesis. They are estimated using an approach based on Monte-Carlo simulated events that are normalized to data in various control regions. In the signal sensitive region, a counting experiment is performed, comparing SM prediction with supersymmetric signal expectations. The considered SUSY signals are based on three different signal scenarios, all established within the General Gauge Mediation (GGM) framework.

This analysis has been endorsed by the CMS collaboration, and is documented in detail in an official CMS analysis note [9].

This thesis is structured as follows. Firstly, a theoretical introduction to the SM and supersymmetry is given in Section 2, where SUSY in general is discussed, before in particular gauge-mediated supersymmetry breaking is explained, and the relevant signal models are introduced. Afterwards, the Large Hadron Collider and the CMS experiment are presented in Section 3. In Section 4, the basic event processing, including reconstruction and triggering, together with event simulation is explained, and properties of the used data sets are introduced. Moreover, the identification principle of physical objects, the definition of important high level variables, as well as the event selection and trigger efficiency measurement are discussed. The basic analysis strategy and background prediction is explained in detail in Section 5, while the definition of the control, validation, and signal regions are given. In addition, the estimation of the background and validation of the background estimation are discussed. The determination of systematic uncertainties is also presented. Final results are discussed in Section 6 together with their interpretation in the context of various signal models. In Section 7, the thesis is briefly summed up, and conclusions are made.

2

Theoretical introduction and motivation

Contents

2.1. System of units	7
2.2. The standard model of particle physics	7
2.3. Supersymmetry	10

In this chapter, at first the relevant unit system is introduced. Afterwards, the standard model of particle physics is explained by discussing its particle content and the interactions between the particles. Thereafter, the important properties and concepts of supersymmetry are outlined, while focusing in particular on gauge-mediated supersymmetry and considered signal scenarios. In the end, a brief overview of the current status of searches for supersymmetry at the LHC is given.

2.1. System of units

For simplicity, the unit system commonly used in particle physics is the natural unit system [10]. In natural units, the reduced Planck constant \hbar and the speed of light c are set to unity:

$$\hbar = c = 1. \quad (2.1)$$

The observables used most frequently in particle physics are the energy, the momentum, and the mass. They are given in magnitudes of eV in the natural unit system. For other variables, such as length and time, the metric unit system is used. Cross sections are given in barn ($1 \text{ b} = 10^{-28} \text{ m}^2$). Integrated luminosities are therefore given in b^{-1} . Electric charges are given in dependence of the elementary charge e .

2.2. The standard model of particle physics

The standard model of particle physics (SM) is a gauge theory describing three of the four fundamental forces, namely the electromagnetic, the weak, and the strong interactions [11]. The gravitational force is described by general relativity [12], which is not described in a quantum field theory as the other three forces.

All particles can be divided into two categories: Particles of integer spin, called bosons, and particles of half-integer spin, called fermions.

The matter content is given by the fermions. Fermions are divided into two subgroups, called quarks and leptons. Leptons take part only in electroweak interactions, while quarks carry also a color charge and therefore interact via the strong force. There are three generations of fermions,

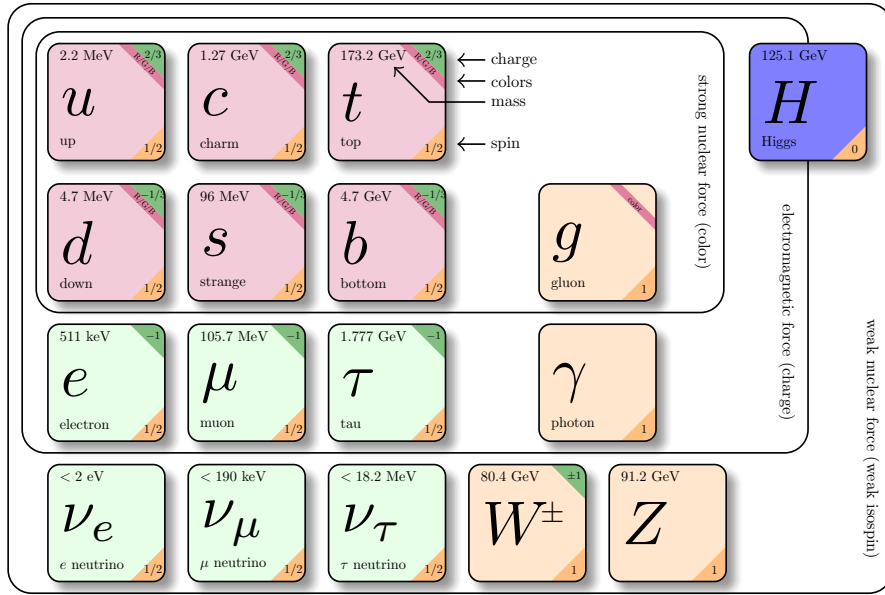


Figure 2.1.: Complete particle content of the standard model [13]. For each particle important properties such as mass, spin, and charges are given. The values are taken from [14].

which include each two leptons and two quark flavors. The quark flavors are the down, up, strange, charm, bottom, and top quarks, while the lepton flavors are made up of three electrically charged particles, the electron (e), the muon (μ), and the tau lepton (τ), as well as three electrically neutral leptons, called neutrinos (ν_e, ν_μ, ν_τ). Of the quarks, there are up-type quarks, the up, charm, and top quark, carrying an electric charge of $+\frac{2}{3}e$, and down-type quarks, the down, strange, and bottom quark, carrying an electric charge of $-\frac{1}{3}e$.

The SM is based on the symmetry group $SU(3) \otimes SU(2) \otimes U(1)$. Interactions are described via the exchange of spin-1 gauge bosons. In case of the strong force, these are 8 massless gluons, which carry color charge and couple to it. The mediator of the electromagnetic interaction is the massless photon, coupling to the electric charge of particles. For the weak interaction the responsible mediator particles are the three massive bosons W^\pm and Z , which couple to the weak isospin.

An illustration of the complete SM particle content with its properties is shown in Figure 2.1. For each particle, a corresponding antiparticle exists with same mass and inversed quantum numbers. Throughout this thesis particles and antiparticles are treated the same way, and both are labeled with the name of the particle.

The strong interaction between color charged particles is described by the quantum field theory of quantum chromodynamics (QCD). The corresponding mediators of the non-abelian gauge group $SU(3)_C$ are the eight gluons, which carry each the color-charge C of an anticolor and a color, giving rise to the self-coupling of gluons. Due to the confinement of quarks [15], quark-antiquark pairs will be produced out of the vacuum if particles with color charge are being separated, since the potential energy density of the strong force includes constant terms, and the potential energy rises with increasing distance. This principle is responsible for the existence of only color-neutral bound states of two (mesons) or three (baryons) quarks, called hadrons.

Indications for hadrons made up of five quarks (pentaquarks) have also been found recently [16]. Based on the same principle, color charged particles are not observed as single particles. In the hadronization process, gluons and quarks lead to the generation of large aggregations of color charged particles while transversing the detector material. These clusters are called jets.

The electromagnetic and weak forces are unified in the electroweak theory [17–20], represented by the gauge group $SU(2)_L \otimes U(1)_Y$. The indices L and Y indicate the symmetry of the $U(1)_Y$ group corresponding to the weak hypercharge Y , and that the weak isospin T couples only to left-handed $SU(2)_L$ doublets of fermions, while the right-handed $SU(2)_L$ singlets carry no isospin. The three mediators of the $SU(2)_L$ group are the W^1, W^2 , and W^3 bosons, and the gauge boson of the $U(1)_Y$ group is the B^0 boson. These four bosons mix to the W^\pm and Z bosons and the photon γ :

$$\begin{pmatrix} \gamma \\ Z \end{pmatrix} = \begin{pmatrix} \cos(\theta_W) & \sin(\theta_W) \\ -\sin(\theta_W) & \cos(\theta_W) \end{pmatrix} \cdot \begin{pmatrix} B \\ W^3 \end{pmatrix}, \quad (2.2)$$

$$W^\pm = \frac{1}{\sqrt{2}} (W^1 \mp iW^2), \quad (2.3)$$

where $\theta_W \approx 0.231$ [14] is the weak-mixing angle, also referred to as Weinberg angle. The resulting weak interaction is parity violating [21, 22]. The W^\pm bosons only couple to left-handed fermions, while the neutral Z boson couples to both left-handed and right-handed particles, but with different strength.

In this theory, the gauge bosons are not allowed to have Dirac mass terms in the Lagrangian, because it would break local gauge symmetry. However, since the Z boson mass is measured to be 91.2 GeV [14], and the W boson mass to be 80.4 GeV [14], the Higgs mechanism is introduced [23–25]. In its simplest representation, it predicts a complex scalar Higgs doublet with a potential that is symmetric, but has a non zero vacuum expectation value. Therefore, the deviation from zero is responsible for the spontaneous symmetry breaking of the $SU(2)_L \otimes U(1)_Y$ gauge group. The Higgs field can be represented by the complex scalar $SU(2)_L$ doublet

$$\Phi = \begin{pmatrix} \Phi^+ \\ \Phi^0 \end{pmatrix} = \frac{1}{\sqrt{2}} \begin{pmatrix} \Phi_1 + i\Phi_2 \\ \Phi_3 + i\Phi_4 \end{pmatrix} \quad (2.4)$$

with the potential

$$V(\Phi) = \mu^2 \Phi^\dagger \Phi + \lambda (\Phi^\dagger \Phi)^2. \quad (2.5)$$

For $\mu^2 < 0$, it results in the non-zero vacuum expectation value of

$$v = \frac{|\mu|}{\sqrt{\lambda}}. \quad (2.6)$$

The field can be reformulated without loss of generality by expanding around the vacuum expectation value and transforming to unitary gauge as

$$\Phi = \frac{1}{\sqrt{2}} \begin{pmatrix} 0 \\ v + h \end{pmatrix}, \quad (2.7)$$

where h is a scalar field. Thereby, three of the four degrees of freedom of the field are consumed to give mass terms to the W and Z bosons. The remaining degree of freedom is the spin-0 Higgs boson. For consistency, leptons and quarks acquire also masses in the SM via Yukawa

interactions with the Higgs field. Such a neutral boson has been observed in proton-proton collisions at the LHC in 2012 [1, 2], and its mass has been determined to be 125.09 ± 0.24 GeV. Measurements regarding the Higgs boson are in good agreement with SM predictions [26], and recently also the couplings of Higgs bosons to the top quark [27], and decays of Higgs bosons to bottom quarks and tau leptons have been observed [28, 29], strengthening the presumption, that the found Higgs boson is the postulated SM Higgs boson.

Indications for physics beyond the standard model

Although the SM describes all phenomena observed at high energy particle colliders successfully, different observations and theoretical arguments indicate that there must exist physics beyond the standard model (BSM):

1. Precise measurements of the cosmic microwave background and theoretical interpretations suggest, that only 4.9% of the universe consists of ordinary matter, while the remainder is composed of dark energy and dark matter [30]. The existence of dark matter is also observed in gravitational lensing effects [31] and in the velocity of rotation curves of spiral galaxies [32]. Inside the SM, there exists no particle that could explain the total amount of dark matter in the universe.
2. It is assumed, that in the early age of the universe there was the same amount of matter and antimatter. But, today we observe the existence of much more matter than antimatter [33, 34]. In order to explain this discrepancy, different conditions, such as \mathcal{CP} -violation and baryon number violation, must be fulfilled [35]. However, in the SM there are no known sources of \mathcal{CP} -violation effects large enough to give rise to such big differences, while baryon number conservation is not violated at all.
3. In the SM, neutrinos are predicted to be massless particles. But, the observation of neutrino oscillations are only explicable if neutrinos are massive particles [14, 36].
4. The observation of a Higgs boson in 2012 on the one hand marks the great success of the SM, but on the other hand directly leads to an issue concerning the Higgs mass, which is known as the "Hierarchy Problem". The Higgs boson couples to all massive particles, with coupling strengths proportional to their masses. But unlike for all other particles, the correction to the Higgs boson mass is quadratically divergent at low energies, caused by virtual loop corrections. The cut-off scale for these corrections can be as large as the validity scale of the SM. Thus, the Higgs boson mass can be enlarged to the order of the Planck scale (10^{19} GeV). Since its mass was measured at the LHC to be approximately 125 GeV, and due to the large difference between the electroweak scale (10^2 GeV) and the Planck scale, these correction terms need to cancel extremely precisely over 32 orders of magnitude. This is considered "unnatural", leading to the expectation that new physics exists in the energy range between the electroweak and the Planck scale.
5. Driven by the electroweak unification, the unification of all forces except for gravity in a grand unified theory (GUT) is well motivated. While the couplings of the forces in the SM do not lead to a unification at very high energies [14], a possible extension of the SM with additional new particles could realize such a unification of the electroweak and strong interactions, see Figure 2.2.

2.3. Supersymmetry

Supersymmetry (SUSY) [37, 38] is one of the most popular BSM theories and was developed in the 1970s [39, 40]. It is well motivated with regard to the theory, because it is the only

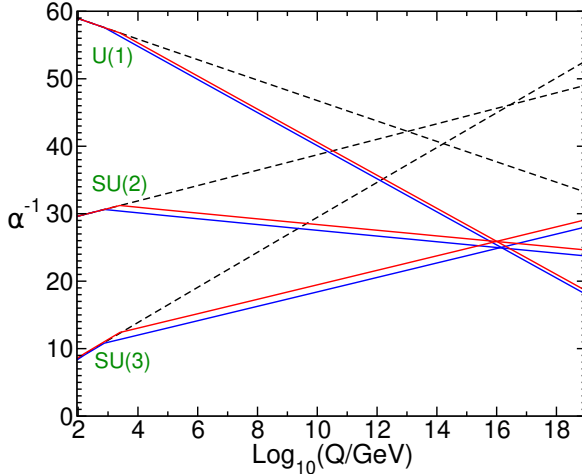


Figure 2.2.: Running couplings for all three fundamental forces in case of the SM (dashed lines) and the minimal supersymmetric standard model (solid lines) for two different sparticle mass scales (750 GeV and 2.5 TeV) [37].

possible extension of space time symmetry. Since then, many different SUSY models have been developed, all based on the same principle: SUSY connects fermions with bosons and the other way around by introducing supersymmetric partners for SM particles. These superpartners differ only in spin by $\pm 1/2$, and all other quantum numbers are equal. With the help of generators Q , bosonic and fermionic states can be transformed into each other:

$$Q | \text{fermion} \rangle = | \text{boson} \rangle, \quad Q | \text{boson} \rangle = | \text{fermion} \rangle. \quad (2.8)$$

Advantages of SUSY are, e.g., that multiple models directly provide candidates for dark matter particles, it realizes the unification of forces, and solves the Hierarchy Problem without fine tuning of physical parameters to match the observation.

The simplest model of SUSY regarding the extension of the particle content is the minimal supersymmetric standard model (MSSM), where only exactly one Q exists. Within the MSSM, for each left and right-handed fermion in the SM exactly one supersymmetric scalar bosons is introduced. To differentiate between SM and SUSY particles, the names of supersymmetric partners are those of the SM particles prepended with an "s-" in case of the fermions. Thus, the partners are called sfermions, and, e.g., the partner of the electron is the selectron. The names of superpartners of bosons are constructed by appending the SM name with an "-ino", making them bosinos, so the gluon's superpartner for example is called gluino. In general, superpartners are called sparticles, and are labeled the same as their SM counterparts, but with a tilde (e.g. $\mu \rightarrow \tilde{\mu}$). Also, the couplings between all sparticles are the same as of their SM partners.

To realize mass terms in the spontaneous symmetry breaking for all particles, including both up- and down-type fermions, the SM Higgs sector needs to be extended to two complex scalar doublets:

$$H_u = \begin{pmatrix} H_u^+ \\ H_u^0 \end{pmatrix}, \quad H_d = \begin{pmatrix} H_d^0 \\ H_d^- \end{pmatrix}. \quad (2.9)$$

The H_d gives masses to the down-type quarks and charged leptons, while the H_u is responsible for the masses of up-type quarks. Four higgsinos as superpartners are introduced in the MSSM accordingly. As a consequence, there are eight degrees of freedom in the Higgs sector instead of four, related to the two Doublets, and giving rise to an expanded Higgs sector consisting of five particles: the two neutral scalars h^0 and H^0 , the two charged scalars H^\pm , and the neutral pseudoscalar A^0 . The remaining three degrees of freedom give masses to the gauge bosons as in the SM. The observed Higgs boson at the LHC can be identified as one of the two neutral

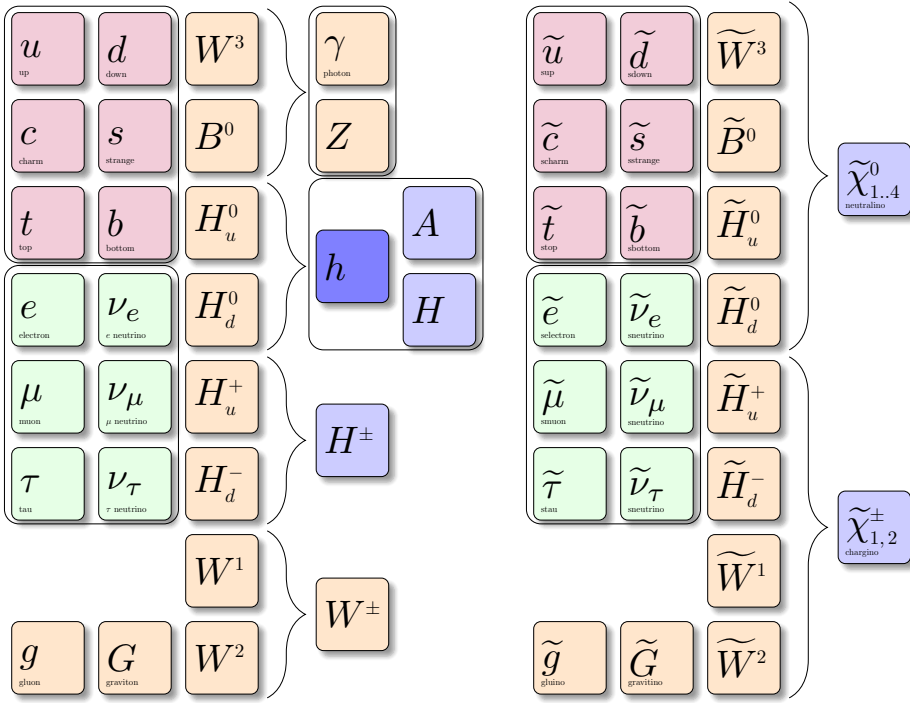


Figure 2.3.: The particle content of the MSSM extended with the graviton and gravitino.
Mixings to mass eigenstates are indicated with the brackets.

scalars, where the lightest boson, the h^0 , is chosen by convention.

The gauginos and higgsinos mix, similar to the mixing in the electroweak sector, to eight mass eigenstates, which are the four neutral neutralinos $\tilde{\chi}_1^0$, $\tilde{\chi}_2^0$, $\tilde{\chi}_3^0$, and $\tilde{\chi}_4^0$, and the four charged charginos $\tilde{\chi}_1^\pm$ and $\tilde{\chi}_2^\pm$.

The total particle content of the MSSM is shown in Figure 2.3. To include gravity, the SM is extended by the graviton G , and the SUSY sector is extended by its superpartner, the gravitino \tilde{G} .

In unbroken SUSY, the particles and their corresponding sparticles should have the same masses, and those SUSY particles should have been found easily in the past (considering, e.g., a selectron with a mass of 511 keV). Therefore, SUSY must be a broken symmetry. Many different theories have been developed over time to explain different breaking scenarios. Attractive approaches are models where gravity is responsible for the SUSY breaking [37], anomaly breaking scenarios [41], and in particular gauge-mediated supersymmetry breaking, which are discussed in the next section.

SUSY can provide Dark Matter candidates, if the lightest supersymmetric particle (LSP) is stable, electrically neutral, and colorless. R-parity

$$R = (-1)^{3B+L+S} \quad (2.10)$$

is therefore introduced as a new conserved quantum number, where S is the spin, B the Baryon number, and L the lepton number. The R-parity is -1 for sparticles, and $+1$ for particles, respectively.

It is not fundamentally necessary that the LSP is stable. In R-parity violating scenarios, decays of all SUSY particles into SM particles are allowed. Hence, the conservation of the Baryon number or the lepton number is violated. R-parity conserving scenarios however are motivated by many precision measurements, such as the lifetime measurement of protons [42]. In this

thesis, only R-parity conserving scenarios are considered. Therefore, SUSY particles can only be produced in pairs and the LSP needs to be stable.

2.3.1. General Gauge Mediation

The phenomenology of SUSY is very rich. While in many models gravity is responsible for SUSY breaking, a different approach, motivating this search, is general gauge mediation (GGM). It is based on the assumption of gauge mediated supersymmetry breaking (GMSB) [43], where an additional "hidden sector" is introduced that is responsible for the breaking. This sector is mainly decoupled, and the possible interactions between the visible and the hidden sector are only achieved by messenger fields mediated by gauge interactions. In the studied GMSB models, the LSP is the gravitino \tilde{G} . This particle is assumed to be very light ($\ll 1 \text{ GeV}$). Therefore, the next-to-lightest supersymmetric particle (NLSP), which basically can be any sparticle, decays promptly. Since the gravitino is stable because of R-parity conservation, electrically and color neutral, it will leave the detector undetected, causing an imbalance in the measured total transverse momentum in proton-proton collisions at the LHC.

In all models considered throughout this thesis, the NLSP is assumed to be the lightest neutralino ($\tilde{\chi}_1^0$). In general, the mixing of the NLSP can include bino, wino, and higgsino components, each enabling different decay channels.

2.3.2. Signal scenarios

The signal scenarios considered in this thesis are discussed in the following. In general, very different production channels for SUSY particles, such as electroweak and strong production, are possible. In case of the LHC proton-proton collisions, SUSY particles can be produced directly in the hard scattering processes of the partons, leading to cascade decays down to the decays of the NLSP to the gravitino and a SM boson. The branching fractions of the lightest neutralino to different SM bosons depends on its mixing

$$\tilde{\chi}_1^0 = \sum_{i=1}^N N_{1i} \tilde{\psi}_i^0, \quad (2.11)$$

where $\tilde{\psi}_i^0 = (\tilde{B}, \tilde{W}, \tilde{H}_d^0, \tilde{H}_u^0)$ [44]. The mass eigenvectors N_{1i} are defined by four parameters, namely the bino mass M_1 and the wino mass M_2 at the messenger scale, the supersymmetric Higgs mass term μ , and $\tan\beta$, the ratio of the up-type to down-type Higgs vacuum expectation values. In GGM, a neutralino NLSP has three possible decay branches, all involving the \tilde{G} [44]:

$$\Gamma(\tilde{\chi}_1^0 \rightarrow \tilde{G} + \gamma) = |N_{11}c_W + N_{12}s_W|^2 \mathcal{A} \quad (2.12)$$

$$\Gamma(\tilde{\chi}_1^0 \rightarrow \tilde{G} + Z) = \left(|N_{12}c_W - N_{11}s_W|^2 + \frac{1}{2}|N_{13}c_\beta - N_{14}s_\beta|^2 \right) \left(1 - \frac{m_Z^2}{m_{\tilde{\chi}_1^0}^2} \right)^4 \mathcal{A} \quad (2.13)$$

$$\Gamma(\tilde{\chi}_1^0 \rightarrow \tilde{G} + h) = \frac{1}{2}|N_{13}c_\beta + N_{14}s_\beta|^2 \left(1 - \frac{m_h^2}{m_{\tilde{\chi}_1^0}^2} \right)^4 \mathcal{A} \quad (2.14)$$

Here, c_W , s_W , c_β , and s_β are abbreviations for $\cos(\theta_W)$, $\sin(\theta_W)$, $\cos(\beta)$, and $\sin(\beta)$, respectively. The formulae hold in cases of on-shell Z and h production. \mathcal{A} is a parameter responsible for the NLSP lifetime [45, 46]:

$$\mathcal{A} = \frac{m_{\tilde{\chi}_1^0}^5}{16\pi F_0^2} \approx \left(\frac{m_{\tilde{\chi}_1^0}}{100 \text{ GeV}} \right)^5 \left(\frac{100 \text{ TeV}}{\sqrt{F_0}} \right)^4 \frac{1}{0.1 \text{ mm}}, \quad (2.15)$$

where F_0 is the scale of SUSY breaking, its range is given by $10 \text{ TeV} \lesssim \sqrt{F_0} \lesssim 10^6 \text{ TeV}$, and it is related to the gravitino mass via

$$m_{\tilde{G}} = \frac{F_0}{\sqrt{3} M_{Planck}}. \quad (2.16)$$

Branching fractions for pure bino- or wino-like NLSPs are shown in Figure 2.4. Since the final

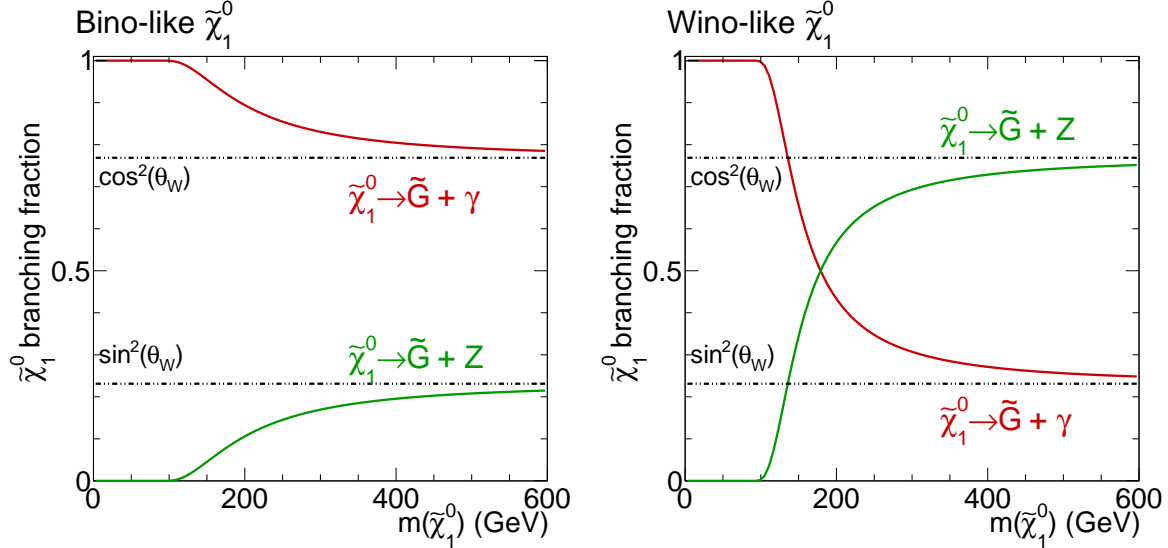


Figure 2.4.: Branching fractions for pure bino (left) and wino (right) NLSP scenarios with different parameters.

state investigated in this analysis consists of a Z boson and a photon, the search is sensitive in particular to bino- and wino-like NLSP scenarios.

One scenario used in the development of this search is a consistent GGM model, where the NLSP is the $\tilde{\chi}_1^0$, and it is assumed to be bino-like. The heavier neutralino $\tilde{\chi}_2^0$ and the lightest chargino $\tilde{\chi}_1^\pm$ are assumed to be wino-like. Therefore, the bino mass equals the mass of the lightest neutralino, while the $\tilde{\chi}_1^+$ and the $\tilde{\chi}_2^0$ are mass degenerate and their mass equals the wino mass. Higgsinos are decoupled, i.e., set to very high masses. Squarks and gluinos are also decoupled in this scenario, allowing only electroweak production modes. For the most dominant process a diagram is shown in Figure 2.5 right. The signal cross section depends only on the wino mass, since $\tilde{\chi}_2^0 \tilde{\chi}_1^\pm$ and $\tilde{\chi}_1^\mp \tilde{\chi}_1^\pm$ production are by far the most dominant production channels. Branching fractions of the gauginos are given by the gaugino masses and their gauge eigenstates, and behave as shown in Figure 2.4. The mass of the neutralinos and the lightest chargino directly influence the transverse momenta in the final state. As can be seen in Figure 2.5, larger mass differences between the NLSP mass and the wino mass will lead to higher momenta of the produced bosons in the cascades. The mass of the NLSP is directly responsible for the momenta of the SM bosons and the gravitino in the final state, and therefore the missing transverse momentum in an event.

A very different approach in regard to the interpretation in full theoretical models are simplified models (SMS)[47]. Here, only a limited particle content is assumed with simplified assumptions on the production and decay channels, providing a more model independent result by probing distinct final states. These results can be reinterpreted in various models [48]. In this thesis two simplified models are considered, one with electroweak gaugino production, and the other one with a strong gaugino production channel.

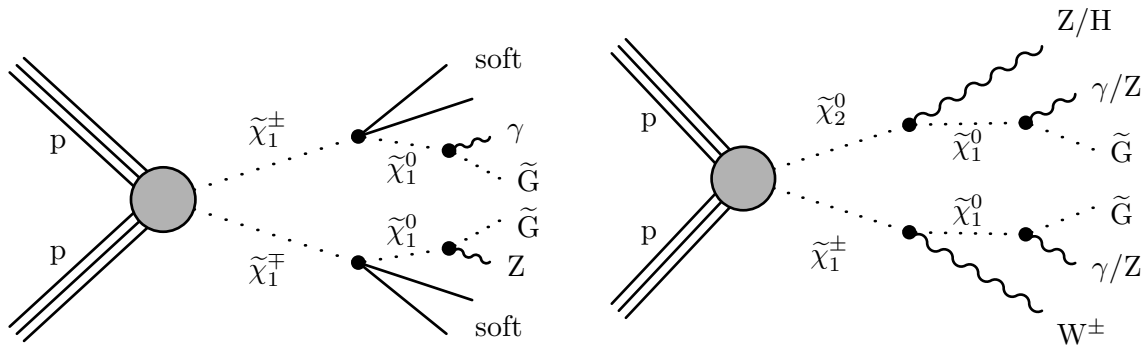


Figure 2.5.: Diagram of the TChizG scenario (left) with chargino pair production, where the charginos decay to neutralinos under soft emission of off-shell W bosons. Also, the chargino-neutralino production is possible. The most dominant production process with a wino-like $\tilde{\chi}_1^\pm$ and $\tilde{\chi}_2^0$ of the full GMSB model (right).

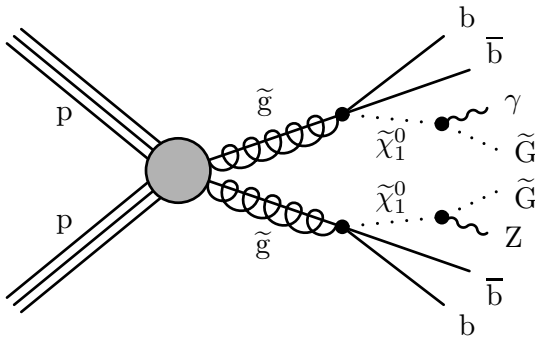
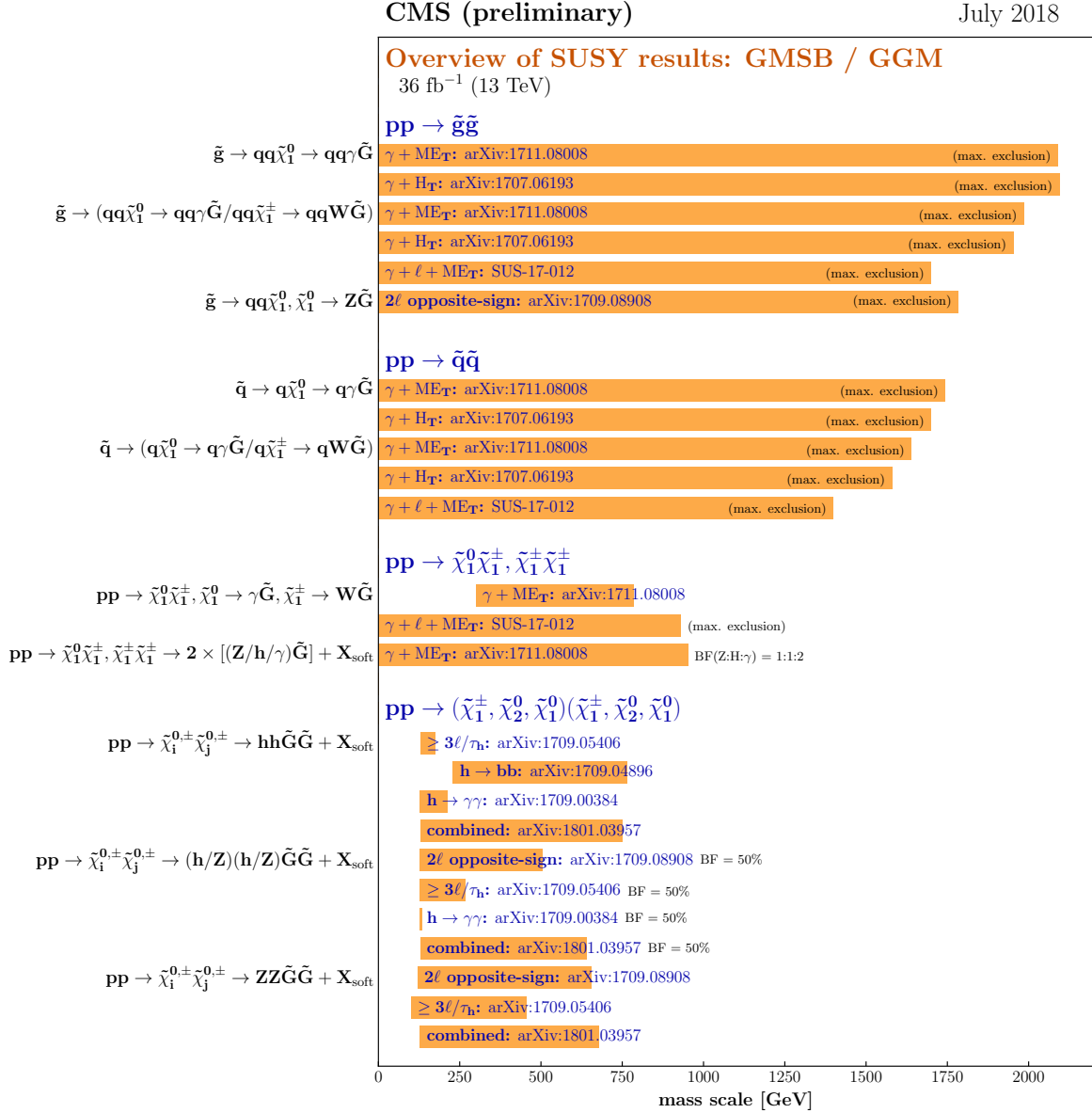


Figure 2.6.: The Feynman diagram for the T5bbbbZG scenario with pair production of gluinos in the hard process, decaying to neutralinos under the emission of b quarks.

The electroweak model is the TChizG SMS, in which only neutralino-chargino and chargino-chargino production is assumed. The lightest chargino and lightest neutralino are assumed to have nearly the same mass, leading to soft emissions of off-shell W bosons in the decays of the charginos to the NLSP. The branching fractions of the lightest neutralino to a gravitino and a photon or a Z boson are fixed to 50% each, i.e., $\mathcal{BR}(\tilde{\chi}_1^0 \rightarrow \gamma \tilde{G}) = \mathcal{BR}(\tilde{\chi}_1^0 \rightarrow Z \tilde{G}) = 0.5$. A diagram for the process can be found in Figure 2.5 left. Squarks and gluinos are decoupled. The strong model considered here is the T5bbbbZG SMS. A diagram is depicted in Figure 2.6. In this model, gluino pair production is assumed, leading to decays to the NLSP under the emission of bottom quark pairs. The branching fractions for the $\tilde{\chi}_1^0$ to photons and Z bosons are again set to 50% each.

2.3.3. Status of SUSY searches at the Large Hadron Collider

Searches for SUSY have been performed at the LEP experiment [49], the Tevatron collider [50], and using the LHC Run I data [51]. Although some promising excesses with respect to the SM expectation have been observed for example in the opposite-sign dilepton channel [52], no clear evidences for SUSY or other BSM theories have been confirmed. Currently SUSY is also constrained by precision measurements of the Higgs boson properties as mentioned above, and by measurements of rare decay processes, such as the $B_s^0 \rightarrow \mu^- \mu^+$ decay observed by the CMS and LHCb collaborations [53]. In the SM, this decay is helicity suppressed, whereas in the MSSM



Selection of observed limits at 95% C.L. (theory uncertainties are not included). Probe up to the quoted mass limit for light LSPs unless stated otherwise. The quantities ΔM and x represent the absolute mass difference between the primary sparticle and the LSP, and the difference between the intermediate sparticle and the LSP relative to ΔM , respectively, unless indicated otherwise.

Figure 2.7.: Mass exclusion limits for simplified models in the context of GMSB of the CMS collaboration [59].

or other extensions to the SM this decay may receive large enhancements.

Direct searches for SUSY in terms of SMS interpretations excluded gluino pair production up to gluino masses of around 2 TeV [54], squark pair production up to squark masses of roughly 1500 GeV, and sbottom (stop) masses of approximately 1500 GeV [55] (1200 GeV [56]), respectively. The production of electroweakinos (electroweak gauge bosinos) is excluded for chargino and neutralino masses up to around 1.1 TeV [57]. Regarding GMSB scenarios, the currently most stringent exclusion limits set by the CMS collaboration [58] are shown in Figure 2.7. The presented results are based on the proton-proton collision data recorded with the CMS detector in 2016, corresponding to an integrated luminosity of 36 fb⁻¹ with a center-of-mass energy of $\sqrt{s} = 13$ TeV. Searches similar to the one presented in this thesis exclude electroweakino production scenarios up to roughly 980 GeV, when final states tagged with a high-energy photon and large missing transverse momentum are analyzed [6]. Searches targeting the single lepton

plus photon final state [8] have set lower limits. Strong exclusions for gluino and squark pair production scenarios are set by searches targeting events with large hadronic activity and photons [5] and searches investigating events with photons together with high b-jet multiplicity [7] over the whole parameter space. They set limits up to approximately 2.2 TeV for gluino masses and 1.8 TeV for squark masses.

Despite the high exclusion limits set by CMS and ATLAS analyses [60–62] in comparable ways, large regions of phase space remain unexplored. But since there are many different SUSY models, and the phenomenology of SUSY is very rich, including scenarios with R-parity violation, compressed mass spectra, long-lived particles and displaced vertices, all described in different breaking scenarios, many studies and searches are yet to be performed. Nevertheless, although the sparticle masses are not predicted by theory, natural SUSY scenarios without great fine tuning should lead to sparticle masses in the order of $\mathcal{O}(\text{TeV})$, which are accessible at the LHC [63].

The experiment

Contents

3.1. The Large Hadron Collider	19
3.2. The Compact Muon Solenoid	21

In this chapter, the relevant experimental setup is discussed. Beginning with the description of the Large Hadron Collider (LHC), which accelerates the proton beams, thereafter the Compact Muon Solenoid (CMS) experiment and detector with all important subdetector components is explained.

3.1. The Large Hadron Collider

The Large Hadron Collider [64, 65], located at the European Organization of Nuclear Research (CERN) near Geneva in Switzerland, is the worlds largest and most powerful hadron collider. The design center-of-mass energy for proton-proton (pp) collisions is $\sqrt{s} = 14 \text{ TeV}$, while the LHC started operating in 2010 with a center-of-mass energy of 7 TeV . It was increased afterwards for the 2012 run period to 8 TeV . After the end of Run I and the first long shutdown, the LHC started operating again in 2015 with an increased center-of-mass energy of 13 TeV . This energy was maintained through the whole Run II for pp collisions until the end of 2018. In the near future, the LHC will be upgraded again in the long shutdown II, so that with the beginning of 2021 operations with the design energy of 14 TeV are planned. The LHC is also capable of accelerating lead ions and xenon ions with an energy of around 2.7 TeV per nucleon.

The LHC is a synchrotron collider built in a tunnel with a circumference of 27 km, which was already used for the Large Electron Positron collider (LEP) [66] in the past. The proton beams are accelerated using various pre-accelerators, such as the Booster, Proton Synchrotron (PS), and the Super Proton Synchrotron (SPS), accelerating protons to an energy of 450 GeV before entering the main storage ring. Four main experiments are located at the LHC, each built around one collision point. These are: ALICE (A Large Ion Collider Experiment) [67], ATLAS (A Toroidal LHC Apparatus) [68], CMS (Compact Muon Solenoid) [58], and LHCb (LHC Beauty) [69]. CMS and ATLAS are designed to be independent experiments by using different detector layouts, searching both for BSM physics, measuring precisely properties of the SM, and improve the knowledge of the Higgs sector. Besides those tasks, they also analyze ion collisions to gain a deeper understanding of the strong interaction. Initially ATLAS and CMS were mainly designed to find the SM Higgs boson.

The tasks of ALICE include studies of the quark-gluon-plasma, where the confinement is abrogated, leading to asymptotically free quarks and gluons.

LHCb investigates mainly mesons that include charm and bottom quarks, to perform precision

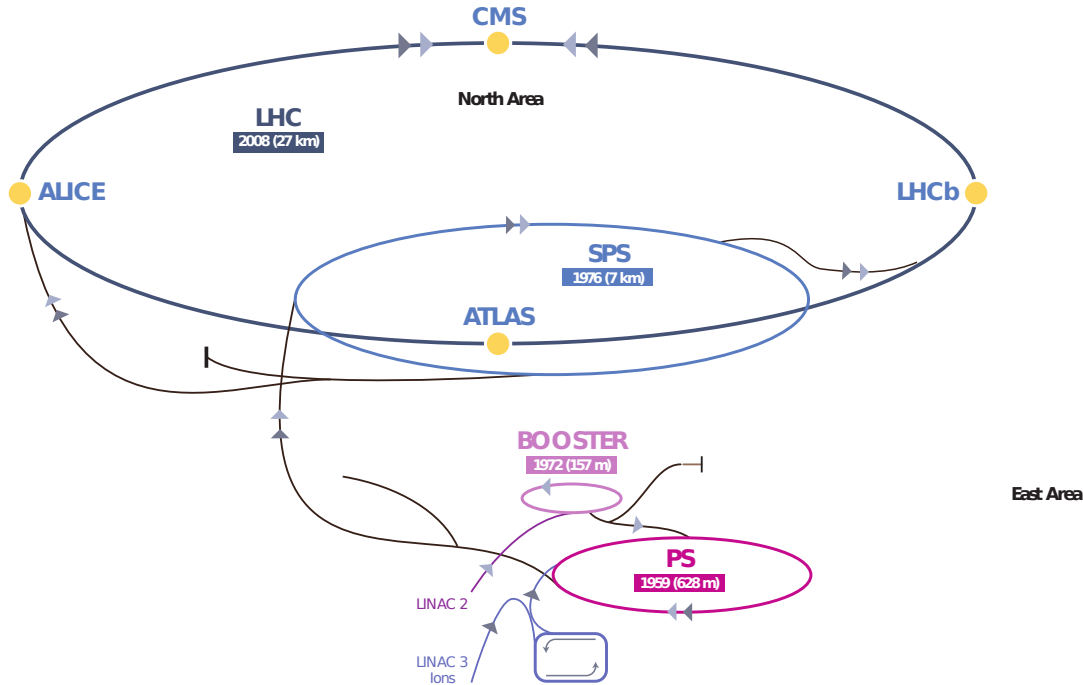


Figure 3.1.: A sketch of the total LHC accelerator complex [70] including the preaccelerators. The four main experiments are marked as yellow dots.

measurements of the SM and look for \mathcal{CP} -violation and hints for new physics. The asymmetric detector design of LHCb favors such studies, since the forward region with particles flying close to the beam axis, is enriched with such events. A schematic sketch of the LHC apparatus including the four big experiment locations at the interaction points and the preaccelerators is shown in Figure 3.1.

As the protons are accelerated to an energy of 450 GeV, they are injected in bunches of approximately $N_b = 1.1 \cdot 10^{11}$ particles into the two beam pipes counter rotating in bunch spacings of 25 ns. To achieve a center-of-mass energy of 13 TeV, each beam has to reach an energy of 6.5 TeV. Therefore, superconducting cavities operating at 400 MHz accelerate the protons, and dipole magnets force the beams on their orbital path. Higher order multipoles are needed to focus the beam and correct for different beam and magnetic effects. For instance, quadrupoles perform a geometrical, and sextupoles a momentum dependent orbital correction.

One important quantity to characterize a collider is the instantaneous luminosity L , because the rate of any scattering process is proportional to L . It can be defined as

$$L = \frac{N_b^2 n_b f_{rev}}{4\pi\sigma_x\sigma_y} F, \quad (3.1)$$

where N_b is the number of particles per bunch, n_b the number of bunches, f_{rev} the revolution frequency, σ_x and σ_y are the widths of Gaussian distributed beam profiles in x- and y-direction, and F is a geometrical factor accounting for the crossing angle of the beams [71]. The integrated Luminosity \mathcal{L}_{int} is connected to L via

$$\mathcal{L}_{int} = \int L dt. \quad (3.2)$$

The number of events N being produced for a given process with cross section σ is given by

$$N = \mathcal{L} \cdot \sigma. \quad (3.3)$$

In 2016, the LHC provided a total integrated luminosity of 40.8 fb^{-1} , while the CMS detector recorded 37.8 fb^{-1} , and 35.9 fb^{-1} were validated as good to be used for physics analysis [72].

3.2. The Compact Muon Solenoid

The data used in this thesis were recorded by the CMS detector [58, 73] in 2016. The CMS detector is a multi-purpose detector housing different subdetectors. From inside to outside, these are the tracker system including a pixel and the silicon strip detector, the electromagnetic calorimeter, the hadronic calorimeter, followed by the solenoid magnet and the muon system. A sketch of the CMS detector is shown in Figure 3.2. In the following, at first the used coordinate system to describe the detector is introduced, and afterwards each subdetector and the trigger system is briefly explained.

The coordinate system used to describe the detector has its origin located at the interaction point, and the z-axis points in the direction of the beam axis westwards toward the Jura mountains. The y-axis points upwards, while the x-axis points to the center of the LHC ring. To exploit the underlying symmetry of the detector, a transformation to an angular coordinate system is chosen. The azimuthal angle ϕ is measured in the x-y plane, where $\phi = 0$ equals the

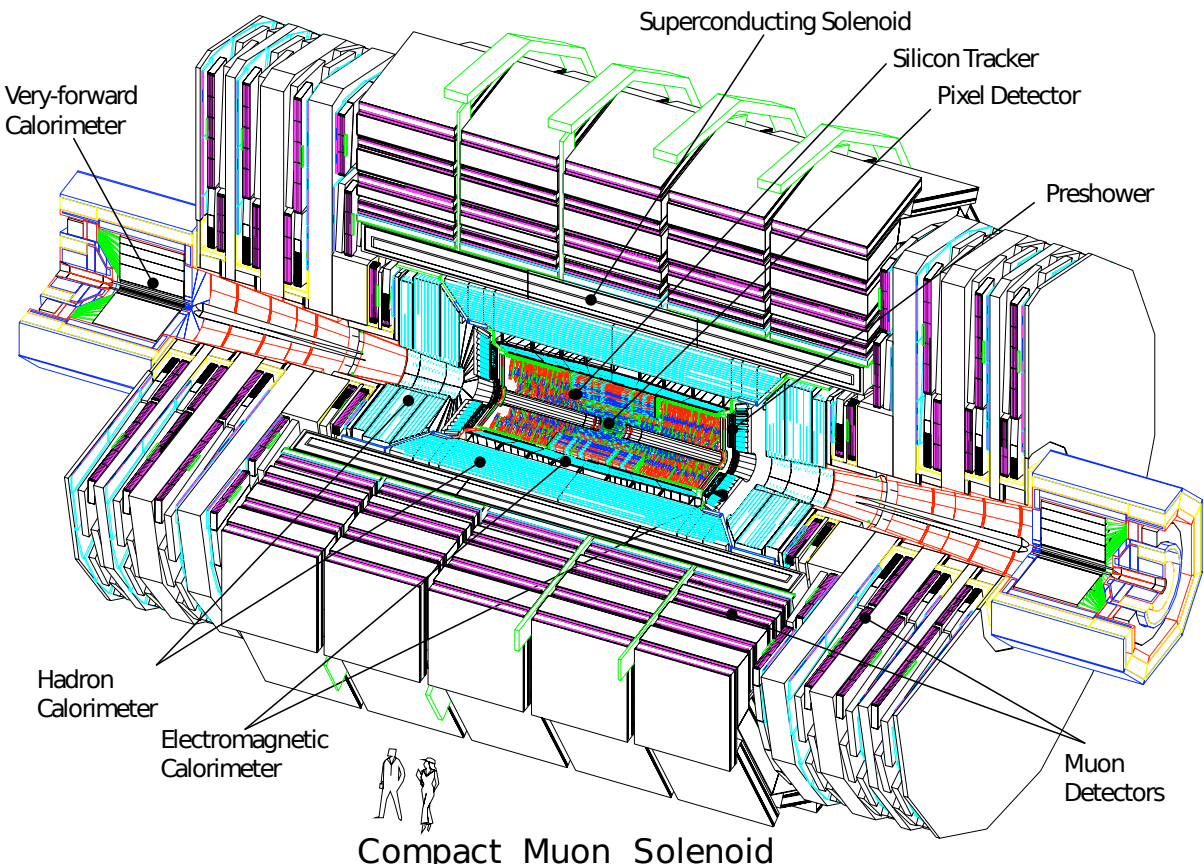


Figure 3.2.: A sketch of the CMS detector showing all subdetectors. [73]. The innermost part of the detector is the tracker system, composed of the pixel and silicon strip detectors. Outside the tracking system the electromagnetic and hadron calorimeters are placed within the solenoid magnet. The outermost part of the detector is the muon system.

direction of the x-axis, and ϕ ranges from $-\pi$ to π . The polar angle θ is measured from the positive z-axis, and the pseudorapidity η is introduced as

$$\eta = -\ln \left(\tan \left(\frac{\theta}{2} \right) \right). \quad (3.4)$$

The advantage in using η instead of θ is that differences in η are invariant under Lorentz-boosts along the beam axis, and in the limit of massless particles the pseudorapidity equals the rapidity. Another important quantity is the geometric distance between two objects in the detector

$$\Delta R = \sqrt{(\Delta\phi)^2 + (\Delta\eta)^2} \quad (3.5)$$

In proton proton collisions, the initial total momentum of the colliding partons is unknown, since they carry only a fraction of the proton energy. In contrast, the transverse momentum in the initial state is negligible, and therefore, the transverse momentum

$$p_T = |\vec{p}_T| = |\vec{p} \cdot \sin(\theta)| \quad (3.6)$$

is a widely used quantity.

Most of the subdetectors are divided into a low η part (barrel), and two high η parts (endcaps). Each of the subdetectors is designed to measure certain properties of different particle types, to ensure both a good particle distinction and identification, and precise measurements of energy, momenta, and trajectories.

3.2.1. The tracker system

The innermost part of the CMS detector is the inner tracker, which consists of two main components, a silicon pixel and a silicon strip detector¹. Both components enclose parts parallel to the beam pipe in the barrel, and parts orthogonal to the beam axis in the endcaps. They cover a length of 5.8 m and a diameter of 2.5 m. A sketch of the inner tracker with all subparts is shown in Figure 3.3. The tracker is designed to perform precise measurements of particle trajectories and an identification of primary and secondary vertices. Therefore, a high granularity and fast response is needed. The silicon pixel subcomponent is built of three barrel layers (the closest at a radial distance of 4.4 cm to the center of the beam pipe) and two endcap disks, covering a total area size of around 1 m². Each of the approximately 66 million silicon pixel cells has a size of $100 \times 150 \mu\text{m}^2$. This provides good granularity for all track directions.

The silicon strip detector consists of four strip layers in the inner (TIB), and six layers in the outer part (TOB). In the direction of the endcaps, it is built of three inner disk layers (TID), and nine layers in the outer part (TEC).

The inner tracker in total covers a range of $|\eta| < 2.5$ and the sensoring system has a surface area of around 200 m². The performance of the tracker yields a momentum resolution for muons with a transverse momentum of around 100 GeV of 1 – 3% in the pseudorapidity range of $|\eta| < 1.6$. At higher pseudorapidities and momenta the momentum resolution decreases.

3.2.2. The electromagnetic calorimeter

Built around the tracker, the second subdetector of CMS is the electromagnetic calorimeter (ECAL). Its main purpose is to measure the energy of electrons and photons, which produce similar electromagnetic showers in the calorimeter. Only with the combined measurements of the tracker, a differentiation between electrons and photons can be performed. The ECAL is

¹The silicon pixel detector was replaced at the end of the 2016 run. Since in this thesis only 2016 data is used, only the former detector is discussed.

made up homogeneously of lead-tungstate (PbWO_4) scintillator crystals and their light emission is proportional to the deposited energy of traversing particles in an electromagnetic shower. Emitted light in the visible spectrum is measured by photodiodes and phototriodes. The material of lead-tungstate was chosen due to its high density, short Molière radius of 2.2 cm characterizing the shower width, and short radiation length of 0.89 cm. Another big advantage of PbWO_4 is the short scintillation time. In a time window of 25 ns, most of the visible light (approximately 80%) is emitted, which agrees with the bunch spacing of 25 ns. The ECAL is divided into a barrel (EB: $|\eta| < 1.479$) and an endcap part (EE: $1.479 < |\eta| < 3.0$), as can be seen in Figure 3.4 left. The 61200 crystals mounted in the barrel have a length of 23 cm, corresponding to 25.8 radiation lengths, and a cross section of $22 \times 22 \text{ mm}^2$ matching the Molière radius of PbWO_4 . In each ECAL endcap, 3662 crystals are placed, having a larger cross section of $28.6 \times 28.6 \text{ mm}^2$ and a length of 22 cm. To prevent particle trajectories from aligning with the orientation of ECAL crystal borders, the crystals (in EB) are tilted in an angle of 3 degree with respect to their orientation toward the interaction point. In the EE, the tilting varies between 2 – 8 degree in dependence of η . So in total both a compact format and a high granularity is maintained.

The energy resolution of the ECAL is determined to be

$$\left(\frac{\sigma_E}{E}\right)^2 = \left(\frac{2.8\%}{\sqrt{E[\text{GeV}]}}\right)^2 + \left(\frac{12\%}{E[\text{GeV}]}\right)^2 + (0.3\%)^2, \quad (3.7)$$

where the first term covers stochastic effects due to the Poissonian distributed number of created scintillation photons and the second term combines noise effects both from the electronics and multiple collisions per bunch-crossing (pileup). The third term covers constant effects, such as intercalibration effects between the crystals and energy leakage. All values were obtained in test beam setups [75]. The energy resolution was designed to be optimal at energies of around 50 GeV to maximize the sensitivity for the Higgs boson discovery, where photons from the Higgs boson decay were expected.

An additional preshower detector is installed in front of the ECAL endcap, to identify photons coming from meson decays, such as the π^0 .

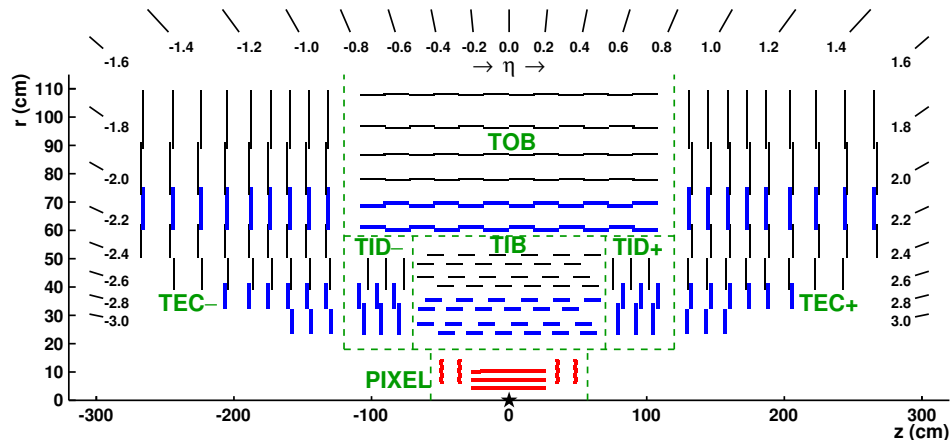


Figure 3.3.: A sketch of one quadrant of the CMS tracker [74]. It is composed of the inner pixel detector (red) and of the strip detector. The silicon strip detector is divided into the TIB, TOB, TID, and TEC.

3.2.3. The hadron calorimeter

The hadron calorimeter (HCAL), which is designed for the energy measurement of hadrons, consists also of a barrel (HB) and endcap parts (HE). It is placed between the ECAL at a radius of 1.77 m and the magnet coil at a radius of 2.95 m. An additional outer barrel part with lower granularity (HO) extends the HCAL outside of the solenoid magnet, making use of its stopping power, while the hadron forward (HF) is installed to cover high pseudorapidity ranges. The barrel part covers pseudorapidities in the range of $|\eta| < 1.4$, while the HCAL endcap together with the outer HCAL covers the range of $1.3 < |\eta| < 3$.

In contrast to the homogeneous ECAL, the HCAL barrel is a so-called sampling calorimeter, consisting of alternating layers of brass absorbers and plastic scintillator material. The front and backplates are made of steel. Hence, the brass plates stop incoming particles, and their energy deposition is measured in the form of hadronic showers creating scintillation light in the plastic layers, which is measured afterwards by hybrid photodiodes. The outer HCAL makes use of the same principle, but uses in addition the stopping power of the solenoid. The hadron forward, covering pseudorapidity ranges of $3 < |\eta| < 5.2$, needs to be more radiation hard in comparison to the rest of the HCAL, since the energy deposit in the forward region is much higher. It is therefore constructed as a Cherenkov detector made of quartz fibres. A total sketch of the HCAL can be seen in Figure 3.4 right.

3.2.4. The solenoid magnet

To measure the momentum of charged particles properly, it is crucial to have bent trajectories. The resolution of momentum measurements at very high energies is directly proportional to the particle momenta and inverse proportional to the magnetic field strength. Thus, for a precise measurement of the curvature of the trajectory, a strong magnetic field is needed. In case of the CMS detector, this is provided by a superconducting NbTi magnet, cooled to 4.8 K, inducing a magnetic field of 3.8 T inside the solenoid. Outside in the muon chambers, that are discussed in the next section, the magnetic field is weaker (approximately 2 T). By choosing a solenoid with a length of 12.5 m and a diameter of 6.3 m, the solenoid defines the CMS detector design, especially with regard to the limited space for the tracking system, the ECAL, and the HCAL.

3.2.5. The muon system

The outermost part of the CMS detector is the muon system. Because all other charged particles beside muons should be stopped in the inner layers, muons are the only particles entering

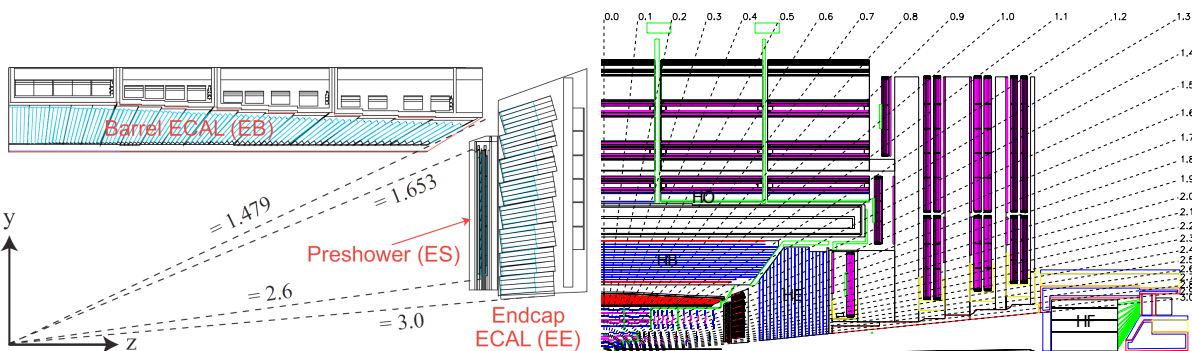


Figure 3.4.: A sketch of one quadrant of the CMS detector for the ECAL (left) [76], and the whole detector (right) [58]. The subparts of the HCAL, the HE HB HO, and HF are indicated separately.

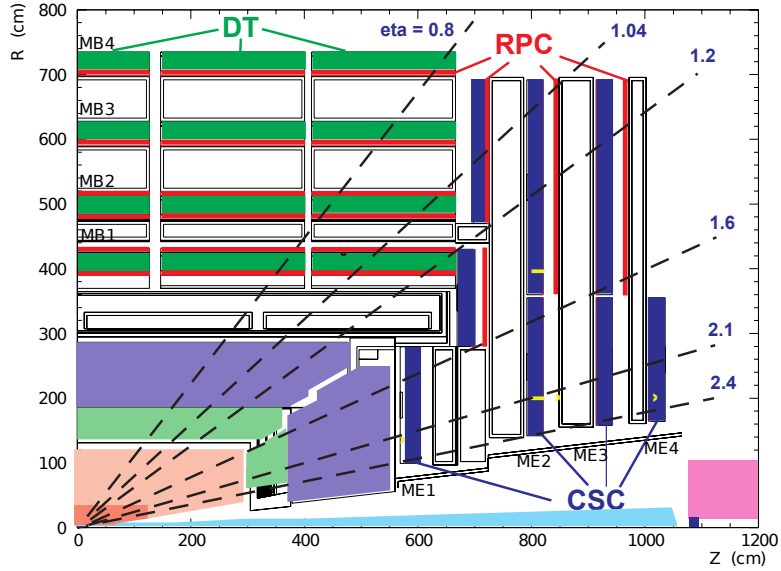


Figure 3.5.: A sketch of one quadrant of the CMS detector with the main detector components [73], especially the different muon detectors, is shown.

the muon system and leaving a signature there. Three different types of detectors are used to measure and identify muons. The barrel part ($|\eta| < 1.2$) is covered by four stations of drift tubes (DT). Cathode strip chambers (CSC) are covering the endcap at pseudorapidities in the range $0.9 < |\eta| < 2.4$, because in this region a higher muon rate is expected, and CSCs in contrast to DTs have a faster response time and are more radiation hard. The muon momentum resolution, dependent on the η region, varies between 10% in the barrel region to around 20% in the endcap region for muons reconstructed standalone by the muon system with a transverse momentum above 15 GeV. In a combined reconstruction using also the tracker information, the resolution is of the order of 1 – 6% for muons with momenta lower than 100 GeV and about 10% for TeV muons [77]. Again, the energy resolution was designed to be at its maximum at around 50 GeV, where muons from the diboson Z decays of the Higgs boson were expected. Additional detector components, namely six layers of resistive plate chambers (RPC), are installed in the pseudorapidity range of $|\eta| < 1.8$. Because they show both good time resolution and fast response time, they are mainly used for triggering purposes. The structure of the muon system can be seen in Figure 3.5.

3.2.6. The trigger system

As bunch crossings take place every 25 ns, and therefore at a rate of 40 MHz, it is not achievable to read out and store all events. To keep only physically interesting events and reduce the rate of events to be saved, a trigger system consisting of two stages is implemented [78]. It is composed of the hardware based level 1 (L1) triggers, and the software based high level triggers (HLT). Since the L1 trigger system needs to deliver decisions in a very short time window, it uses only information provided by the calorimeters and the muon chambers. Usually first requirements on the event, such as a minimal deposited transverse energy, and the presence of first estimates for electron and muon candidates, are imposed. The L1 trigger reduces the event rate to a rate of approximately 100 kHz.

More complex decisions are made by the HLT trigger system. It has full access to the complete readout of all subdetectors, and therefore performs selections close to the offline analysis. It reduces the event rate to $\mathcal{O}(1 \text{ kHz})$ [79].

Using the decisions of the HLT, events are categorized into different subsets, based on event kinematics and the trigger objects, called primary data sets (PD).

Simulation, data processing, and event reconstruction

Contents

4.1.	Data sets	28
4.2.	Monte-Carlo simulation	28
4.3.	Event reconstruction and particle identification	30
4.4.	Definition of observables	35
4.5.	Lepton pair selection	36
4.6.	Triggers and trigger efficiency measurement	37

The data sets, based on the proton-proton collisions recorded with the CMS detector, are among others centrally provided in the MINIAOD format [80] by the CMS collaboration. This format contains only parts of the original event and detector information relevant for most of the physics analyses. SM and signal simulations are also centrally provided in the MINIAOD format with extended generator information, called MINIAODSIM.

All measured data and simulation data sets are further processed with the help of the CMS software framework (CMSSW¹) [81], the CMS Remote Analysis Builder (CRAB3) [82], and the resources of the Worldwide LHC Computing Grid [83], to obtain files of significantly reduced size. The reduced information is stored in the ROOT [84] file format, and can be used by analysts with self-developed software.

In this chapter, at first the used data samples are introduced. Thereafter, an overview of simulation is given, while the simulated samples used in this analysis are reviewed. After that, the event reconstruction performed on all data sets is explained. A more detailed view is given on the reconstruction and identification of physics objects. In the end, the trigger efficiency measurement of the used triggers is discussed.

Protons are objects composed of many different quarks and gluons. The probability to find a distinct parton of a proton with a specific momentum in a deep inelastic scattering is given by parton distribution functions (PDFs)[85], that need to be extracted from data, since the parton content of the proton is not predicted by QCD. An interaction between two partons of the colliding protons is described in the hard interaction. Due to the structure of protons, many different lower energy particles can be produced in interactions between additional partons (multi-parton-interactions). These remnants of the scattering process, together with reconstructed remnants of the protons, are denoted as the underlying event. More important for proton-proton colliders at such high luminosities is pileup, which denotes interactions between additional protons in the same bunch crossing as the hard interaction.

¹Version 8.0.26

4.1. Data sets

This analysis uses different data sets based on the pp collisions of the LHC with a center-of-mass energy of 13 TeV recorded with the CMS detector in 2016, corresponding to an integrated luminosity of 35.9 fb^{-1} . Each primary data set is a composition of events recorded with similar HLT trigger paths. The `DoubleMuon` and `DoubleEG` PDs are used in the central part of the analysis for the signal selection, since they contain events with at least two muons or electromagnetic objects (electron or photon), respectively. `MET` and `HT` PDs are used for trigger efficiency measurements, and the `MuonEG` PD is used for the background prediction. For a list of all used triggers see Section 4.6.

The different PDs are separated into several single samples for different run eras throughout 2016. The paths of the used samples, available via the CMS data set bookkeeping service (DBS) [86], are listed in Table A.1 in the additional material.

4.2. Monte-Carlo simulation

The simulation process for SM background and SUSY signal samples can be divided into three major steps, which are very similar for both cases. At first, for a specific process events are simulated with an event generator. The event generators used for the generation of the samples considered in this analysis are `MADGRAPH 5` in leading order (LO) configuration [87–89], `MADGRAPH5_aMC@NLO` in next-to-leading order (NLO) configuration [87, 90], `PYTHIA 8` [91], or `POWHEG` [92, 93]. Matrix elements for the contributing diagrams are computed, and taking PDFs into account, cross sections are calculated. The simulation can be performed with much higher statistics than data in order to minimize the statistical uncertainty of the simulation.

Depending on the choice of the chosen generator, a separate generator for the simulation of hadronic showers must be used. This is done with `PYTHIA 8`. So that partons generated in matrix element calculations corresponding to the hard interaction, and partons generated with `PYTHIA` in the showering for, e.g., initial state radiation (ISR) are not double counted, a matching with the MLM [88] (LO) or FXFX [90] (NLO) matching schemes is performed. The hadronization of the partons (quarks and gluons) is also simulated with `PYTHIA`, based on the confinement of color charged particles. This, together with the underlying event and pileup, is all incorporated in the CUETP8M1 generator tune [94]. It is based on 7 TeV pp CMS and proton-antiproton CDF measurements. The PDFs used for the generation of the MC samples are provided by the NNPDF 3.0 sets [95].

The big next step, which is the most time and resource consuming part, is the simulation of the detector response. A full model of the CMS detector was constructed with the `GEANT4` [96] package. In the `GEANT4` package, material and particle properties, detector effects, and decay structures are considered in the simulation process, leading to a high accuracy. Since this procedure is very time consuming, a different method is chosen for signal processes. For the generation of signal samples, where theoretical uncertainties dominate and events for many different signal points for each model need to be generated, the CMS `FASTSIM` package is used [97]. It is based on a simplified geometry and parametrizations, yielding approximately a reduction in computing time of the factor 100. Comparing both methods [98], an agreement within around 10% for all distributions, such as the momenta of particles or jet multiplicity, is observed.

All simulated processes used in this analysis are listed in Table 4.1 together with their corresponding cross sections. The DBS paths are given in the appendix in Table B.1.

The Drell-Yan (DY) Z/γ^* process, as well as $Z\gamma$, $W\gamma$, $WW\gamma$, and $WZ\gamma$ production are generated with `MADGRAPH5_aMC@NLO` with NLO accuracy. Top pair production in association with a photon ($t\bar{t}\gamma$) and the production of a W boson in association with jets are also simulated using the `MADGRAPH5_aMC@NLO` generator with NLO accuracy. Top pair production with leptonic decays ($t\bar{t} \rightarrow 2\ell 2\nu 2b$), diboson production of WZ , ZZ , WW , and all single top production processes are generated using `POWHEG`. Diboson WW and $W\gamma$ production, $W + jets$ production, triboson $WW\gamma$ and $WZ\gamma$ production, and all single top production channels are grouped together and denoted as "other" in the following. Cross sections calculated with NLO and next-to-next-to-leading order (NNLO) accuracy [99–107] are used for the normalization of the samples.

The generator used for the signal simulation production is `MADGRAPH5_aMC@NLO` at LO accuracy for the simplified models, and `PYTHIA 8` for the full GGM model. The corresponding DBS paths are also listed in the appendix in Table B.2. The cross sections used in the signal normalization are calculated at NLO accuracy for the full GGM scenario, and at NLO plus next-to-leading logarithmic (NLL) accuracy for the two simplified models [108–116]. For the electroweak SMS, the applied cross sections are calculated for the $\tilde{\chi}_1^\pm \tilde{\chi}_1^0$ and $\tilde{\chi}_1^\pm \tilde{\chi}_1^\mp$ production channels with squarks and gluinos decoupled, and the sum of both is used. In the cross section calculations of gluino pair production for the other SMS, squark decoupling is assumed. The applied cross sections for the GMSB model are different from the ones used for the electroweak SMS, since the GMSB scenario represents a full theoretical model taking several processes into account.

For the GMSB model, signal points are generated with wino masses ($m(\widetilde{W})$) ranging from 215 GeV to 1015 GeV, and bino ($m(\widetilde{B})$) masses ranging from 205 GeV to $m(\widetilde{W}) - 10$ GeV in intervals of 25 GeV. In case of the TChiZG SMS, points are generated with NLSP masses in the range of 300 – 1300 GeV in steps of 25 GeV. The grid of points generated for the T5bbbbZG strong production SMS includes gluino masses ($m(\widetilde{g})$) in the range of 800 GeV to 2500 GeV, while the NLSP mass range is scanned from 10 GeV to $m(\text{NLSP}) = m(\widetilde{g}) - 10$ GeV in non equidistant steps.

As mentioned above, the number of generated events N_{Gen} is very high. Thus, with the measured integrated luminosity \mathcal{L} and a given cross section σ , a global event weight of

$$w = \frac{\mathcal{L} \cdot \sigma}{N_{Gen}} \quad (4.1)$$

is used to rescale the simulation to the physical expectation.

Additional event weights are applied on the simulation to account for differences in the pileup distribution between data and simulation. To improve on the `MADGRAPH` modeling of the multiplicity of additional jets arising from ISR, SUSY SMS events are reweighted as a function of the ISR jet-multiplicity or the transverse momentum of the ISR system, to improve the agreement with observations in data. The latter is based on studies of the transverse momentum of Z boson events. [117]. The differences to unity for the reweighting factors are considered as systematic uncertainties. The `POWHEG` $t\bar{t}$ simulation is also reweighted as a function of the transverse momentum of the top system, based on studies in top pair production cross section measurements [118–121] to improve the agreement of the transverse momenta of the top quarks with data.

Overlap removal

Different physical processes described in higher orders lead to a redundant modeling of distinct diagrams in the matrix element calculation. For each of these processes distinct simulated samples are available, and multiple ones are used in order to achieve a precise modeling of

Table 4.1.: All SM simulated samples used in the analysis with their cross sections. For their corresponding accuracy refer to the text. Additional k-factors to obtain NNLO cross sections for the ZZ samples are applied per event in dependence of the p_T of the diboson system. All samples are of the MINIAODSIM format.

process	σ [pb]	process	σ [pb]
t̄t		diboson	
$t\bar{t} \rightarrow \ell^+\nu b + \ell^-\bar{\nu} \bar{b}$	87.3	$Z\gamma \rightarrow 2\ell\gamma$ ($p_T^\gamma < 130$ GeV)	124.9
t̄tγ		$Z\gamma \rightarrow 2\ell\gamma$ ($p_T^\gamma > 130$ GeV)	0.149
$t\bar{t}\gamma \rightarrow 2\ell 2\nu 2b\gamma$	1.68	WZ	4.91
$t\bar{t}\gamma \rightarrow 4q 2b\gamma$	3.48	$ZZ \rightarrow 2\ell 2\nu$	$0.564 \cdot k(p_T^{ZZ})$
$t\bar{t}\gamma \rightarrow \ell\nu 2b 2q\gamma$	2.51	$WW \rightarrow 2\ell 2\nu$	12.2
DrellYan		$Wg \rightarrow \ell\nu\gamma$	489
$Z/\gamma^* \rightarrow 2\ell$	5765	W jets	
single top		$W + jets$	61527
$W^+ \rightarrow t\bar{b}$	3.36	triboson	
$q\bar{b} \rightarrow q'\bar{t}$	81.0	$WW\gamma$	0.215
$qb \rightarrow q't$	136.0	$WZ\gamma$	0.041
$\bar{b} \rightarrow W^+\bar{t}$	11.7		
$b \rightarrow W^-t$	11.7		

the phase space region of interest with low statistical uncertainties. Since these samples are produced for a distinct process only, e.g., $t\bar{t}$ pair production, NLO contributions in this case overlap with the standalone $t\bar{t}\gamma$ samples, because photon radiation in the initial state on the one hand is an NLO contribution for $t\bar{t}$ production, and on the other hand LO $t\bar{t}\gamma$ production. The same holds for the Drell-Yan Z/γ^* process and the NLO $Z\gamma$ diboson production. To avoid double counting of events, these overlaps need to be removed.

Events being consistent with the generated events of the standalone photon production sample are removed from the inclusive samples to achieve a common higher order description of the selected phase space. Since different generators are used to simulate the different processes, different strategies to remove the overlaps are used, to ensure that double counting of diagram contributions is rejected.

4.3. Event reconstruction and particle identification

To maintain both a precise and robust particle reconstruction, particle reconstruction and identification is divided in two major parts. This is needed, since different types of analyses, such as searches or SM precision measurements have different priorities for the requirements of their selected particles in terms of efficiency, misidentification rate, and resolution.

In the global event reconstruction, at first, particles and their properties, such as momentum, energy, and trajectory, are reconstructed with the Particle flow (PF) algorithm [122] by combining information from all CMS subdetectors. After that, identification criteria determined by specialized CMS physics objects groups are applied, dependent on the choice of the analyst regarding the demands mentioned above.

In the following section, the PF algorithm is briefly introduced by explaining its main features, whereafter more detailed definitions of the physical objects are given.

4.3.1. Particle flow

The excellent performance of the CMS tracking system, the high granularity of the ECAL, and the highly efficient muon tracking system is exploited by combining the information of all sub-detectors in a global identification of physical objects in the PF event reconstruction.

The PF reconstruction and identification procedure is divided in multiple subtasks. At first, tracks and clusters are reconstructed separately. Afterwards, they are combined by a linking algorithm. Eventually, so-called PF blocks are formed out of the links, and final decisions are made on the type of the particle.

A combinatorial track finding algorithm based on Kalman Filtering [123] is used to reconstruct tracks in three stages. Firstly, seeds are generated that are compatible with tracker hits and therefore with a trajectory of a charged particle. Secondly, trajectories are built by using all tracker layers. Finally, the particle properties, such as momentum and direction, are determined in a fit. The tracking procedure is optimized to maintain a high efficiency by keeping a low misidentification rate. A tracking efficiency of 99% for muons with a momentum larger than 1 GeV is achieved, compared to 70 – 80% for charged pions. To further increase the efficiency while retaining the misidentification rate as low as possible, an iterative tracking procedure is realized, where each step has a lower efficiency compared to the approach discussed before, but quality criteria requirements ensure a low misidentification rate.

For electrons another separate track reconstruction is realized. In contrast to the tracker based approach described above, an approach based on reconstructed ECAL clusters is used in addition. Thereby, extrapolations back to the inner tracker are realized based on the cluster energy and position.

The muon tracking is also different, since here in addition the muon system can be used to gain further information and increase the efficiency and lower the misidentification rate. Three types of muon tracks are reconstructed. The first are standalone muon tracks, where only information from the muon system, in particular seeds built of hits in the DTs and CSCs, is used to reconstruct a muon trajectory through all muon system subcomponents. Global muon tracks are standalone muon tracks, that can be matched to hits in the inner tracker. Tracker muon tracks are obtained by extrapolating inner tracker tracks to the muon system, and are only considered if at least one muon segment hit matches the extrapolation.

The clustering algorithm is performed in each subcalorimeter separately using also the information of the tracker. It is used to measure the energy and direction of neutral particles such as photons and neutral hadrons, and distinguish them from charged hadrons and photons originating from electron bremsstrahlung. Thereafter, seeds are identified as cells where the energy deposit is larger compared to the neighboring cells. Out of the seeds, topological clusters are built by combining cells that show energy deposits larger as the noise level and being in contact with at least one corner to the already aggregated cells. Within each topological cluster, a fit is performed to obtain the total energy and position of each cluster under the assumption of a Gaussian-mixture model. This model characterizes the energy deposit in each cell of the topological cluster as the combination of several Gaussian distributed energy deposits of each seed. In the ECAL, superclusters are formed for electromagnetic objects, where nearby clusters in a narrow η -window and wider ϕ -window are combined in order to collect the total energy coming from bremsstrahlung and photon conversion. The window size in η and ϕ differs to account for the azimuthal bending of the charged particles in the magnetic field.

The last important part of the PF based reconstruction is the linking procedure, where all information is combined, based on the nature of each particle. Multiple links are then summed

up to a particle flow block, in which separately the final decisions are made consecutively. After each particle identification step, the used subdetector information, such as tracks and clusters, is removed from the PF block and not considered for further identification steps.

Muons are identified first, driven by the high reconstruction efficiency and low misidentification rate using the muon system. Except for jet remnants reaching the muon system, called punch-throughs, muons are the only particles leaving a signature in the muon system.

Electrons and prompt photons are identified next, since they produce very similar signatures in the ECAL.

Finally, neutral and charged hadrons, and non prompt photons, e.g., originating from meson decays, are identified.

Based on the PF reconstruction, an analysis-specific physical object selection can be performed on top of the PF objects, which is discussed in the following.

4.3.2. Primary vertex and quality requirements

The primary vertex of an event is defined by the vertex with the largest sum of associated transverse momenta squared determined by vertex reconstruction algorithms [124], and needs to be reconstructed within a distance of 24 cm in z direction, and 2 cm in the x-y plane.

Also, several event quality filters developed by CMS [125] are applied to the event selection in order to reject contaminated events. The rejected events consist mainly of events with faulty detector signals caused by noise or anomalies, spurious energy deposits in ECAL endcap crystals, cosmic muons, muons being misidentified as charged hadrons, or muons produced in scattering processes with the beam halo.

4.3.3. Muons

Muons are required to have a transverse momentum larger than 15 GeV. Because the muon chambers extend only to a pseudorapidity range of $|\eta| < 2.4$, muons need to be reconstructed within this region. In addition, muons have to pass quality requirements suggested by the CMS collaboration [126].

A muon candidate needs to be reconstructed as a PF muon, and either as a global muon or a tracker muon. If it is reconstructed as a global and a as tracker muon, the segment compatibility, which is a measure for the comparability between the tracker tracks and an extrapolation to the muon system, has to be larger than 0.303. In addition, more than 80% of the inner track layers need to be used in the track fit, the normalized goodness of fit needs to be less than 3, the match between the standalone muon position and the tracker muon must have $\chi^2 < 12$, and the maximum χ^2 found by a kink finding algorithm, which tries to separate the track into two independent tracks, needs to be smaller than 20. If the muon is reconstructed exclusively as a tracker muon, only the segment compatibility needs to be greater than 0.451, and the other requirements on the track quality are removed.

Besides the identification requirements, conditions on the position of the track relative to the reconstructed primary vertex are imposed. In the transverse direction (d_{xy}), muon tracks need to be closer than 0.05 cm to the vertex, and in the longitudinal direction (d_z), the distance needs to be smaller than 0.1 cm.

To quantify the dominance of an object with respect to its surrounding particles in its vicinity described by a cone, the concept of isolation is introduced. A isolation definition is used, called mini isolation, where the cone size in the $\phi - \eta$ plane is calculated relative to the transverse momentum of the particle as follows:

$$R = \max \left(0.05, \min \left(0.2, \frac{10 \text{ GeV}}{p_T} \right) \right). \quad (4.2)$$

Pileup corrections are also taken into account in the mini isolation calculation. The determined energy deposited in the cone around the muon must not exceed 20% of the transverse momentum of the particle.

All identification criteria can be found in Table 4.2.

Table 4.2.: Identification criteria for muons, spread for muons being reconstructed as solely tracker and as tracker and global muons.

Variable	Value	
	tracker and global muon	tracker muon
segment compatibility	> 0.303	> 0.451
fraction of valid inner tracker hits	> 0.8	-
normalized χ^2 of global track fit	< 3	-
track standalone position match (χ^2)	< 12	-
kink finder (χ^2)	< 20	-
p_T	> 15 GeV	
$ \eta $	< 2.4	
mini isolation	< 0.2	
d_{xy}	< 0.05 cm	
d_z	< 0.1 cm	

4.3.4. Electrons

The requirements imposed on the electron selection is driven by a symmetric approach between the two lepton selections. The same conditions on the distance to the primary vertex, ($d_{xy} < 0.05$ cm, $d_z < 0.1$ cm), pseudorapidity ($|\eta| < 2.4$), and transverse momentum ($p_T > 15$ GeV) need to be fulfilled. The mini isolation criterion is tightened to 10%, since the probability to misidentify a jet as an electron is higher than for muons.

The identification requirements determined by the CMS Collaboration [127] separately for electrons reconstructed in the ECAL barrel (EB: $|\eta_{Supercluster}| < 1.479$) and endcap (EE: $|\eta_{Supercluster}| > 1.479$) region are listed in Table 4.3. Here, $\sigma_{in\eta}$ is a quantity characterizing the width of the electromagnetic shower shape in the ECAL in η -direction. It is calculated as the weighted variance of energy deposits in a 5x5 ECAL pixel array around the seed of the supercluster. Since jets emerging from hadrons have a wider shower in the ECAL than electrons, a differentiation can be achieved. Consistency between the information of the reconstructed track at the vertex and the supercluster is required, by setting conditions on $\Delta\eta$ and $\Delta\phi$ between both reconstructed positions, and additional consistency requirements on the supercluster energy E and track momentum p . To further separate electrons from hadrons, more energy should be deposited in the ECAL rather than in the HCAL (H/E). An isolation requirement based on the PF determined isolation assures that prompt electrons are separated from electrons coming from, e.g., jets. Photons misidentified as electrons are suppressed by imposing a requirement on the number of missing inner hits in the pixel, and an additional veto for photon conversions to electron-positron pairs determined in an χ^2 fit.

4.3.5. Photons

Photons are required to have a transverse momentum larger than 20 GeV. Because in the considered SUSY signal scenarios the sparticles typically have high masses, central collisions are needed to produce these in the pp interactions. Therefore, the sparticles decay mainly in rest, and the

photons originating from the decays are produced more centrally in comparison to SM processes. Hence, only photons reconstructed in the ECAL barrel are considered ($|\eta| < 1.4442$). Additional identification criteria determined by the CMS Collaboration [128] are listed in Table 4.4. Similarly to the requirements on $\sigma_{i\eta i\eta}$ and H/E for the electron selection, these conditions in the photon identification ensure the suppression of selecting hadrons faking the photon signature. Additional different isolation criteria lower the amount of selected photons originating from neutral and charged hadrons, and photons created from meson decays.

Requirements on the minimum distance in the $\eta - \phi$ plane between the photon and selected lepton candidates ($\Delta R(\gamma, \ell) > 0.3$) significantly reduce contributions from final state radiation (FSR) photons. By requiring that no pixel seed can be assigned to a trajectory between the ECAL supercluster and the interaction point, a clear differentiation between electrons and photons is achieved.

4.3.6. Jets

Jets are complicated objects due to the complexity of the hadronization and fragmentation processes. Therefore, a sophisticated clustering algorithm is needed to identify them and measure their energy properly. Jets are clustered with the anti- k_T algorithm [129] included in the FASTJET package [130, 131] with a distance parameter of $R = 0.4$. In the clustering procedure, each PF object is considered a pseudojet, and these pseudojets are summed up iteratively until a certain breaking condition is fulfilled. The final jet momentum is defined as the sum of the momenta of the constituents of the jet. Charged hadrons not emerging from the primary vertex are not considered in the clustering. The jet energy is corrected for effects originating from pileup and the detector response, tuned with the help of different data control selections and simulation [132]. Reconstructed jets are required to pass loose identification criteria proposed by the CMS Collaboration [133], to have a transverse momentum larger than 30 GeV, and their pseudorapidity must not exceed $|\eta| = 3$. In addition, jets overlapping with photon or lepton candidates in a cone with radius $R = 0.4$, are removed from the selection to avoid double counting of objects.

Table 4.3.: Identification criteria for electrons given separately for reconstructed electrons in the barrel and endcap.

Variable	Value	
	EB	EE
$\sigma_{i\eta i\eta}$	< 0.00988	< 0.0298
$\Delta\eta_{Seed, Track}$	< 0.00311	< 0.00609
$\Delta\phi_{Seed, Track}$	< 0.00311	< 0.00609
H/E	< 0.253	0.0878
relative combined PF isolation	< 0.0695	< 0.0821
$ \frac{1}{E} - \frac{1}{p} $	< 0.134	< 0.13
number of missing inner hits	≤ 1	≤ 1
photon conversion veto	true	true
p_T	> 15 GeV	
$ \eta $	< 2.4	
mini isolation	< 0.1	
d_{xy}	< 0.05 cm	
d_z	< 0.1 cm	

4.4. Definition of observables

Throughout this thesis, different observables are used to define different phase space regions, in particular the signal region and control and validation regions important for the background prediction. All these high-level variables are defined based on low-level quantities such as the p_T of different objects.

Missing transverse momentum

Before a collision the transverse momentum of the colliding protons is nearly negligible. Therefore, the missing transverse momentum quantifies the imbalance of all reconstructed particle flow objects ($N_{PFObj.}$) in an event projected to the transverse plane and is defined as

$$p_T^{\text{miss}} = |\vec{p}_T^{\text{miss}}| = \left| - \sum_i \vec{p}_{T,i} \right|. \quad (4.3)$$

Jet energy corrections are propagated to the missing transverse momentum vector to avoid a bias in events with large hadronic activity.

Missing transverse momentum p_T^{miss} is one of the most important observables in searches for BSM physics. In typical SUSY models, see Section 2.3, significant p_T^{miss} is expected in the events due to the LSP leaving the detector undetected. In SM processes only neutrinos and mismeasurements of, e.g., the jet energies lead to missing transverse momentum. In such SUSY events, the LSP gains a lot of energy through the decays of sparticles with higher masses. Hence, much more p_T^{miss} is expected to be produced in SUSY events as in SM processes, also due to the production of two LSPs in the final state because of R-parity conservation.

Total hadronic activity H_T

The hadronic activity H_T is defined as the scalar sum of the transverse momenta of all jets, that are clustered with the procedure above, and fulfill $|\eta| < 3$ and $p_T > 30 \text{ GeV}$:

$$H_T = \sum_{\text{jets}} |p_{T,i}|. \quad (4.4)$$

Invariant dilepton mass $m_{\ell\ell}$

The invariant dilepton mass $m_{\ell\ell}$ is defined as the absolute value of the sum of both lepton four momenta:

$$m_{\ell\ell} = |\mathbf{p}_{\ell_1} + \mathbf{p}_{\ell_2}|. \quad (4.5)$$

Table 4.4.: Identification criteria for photons reconstructed in the ECAL barrel.

Variable	Value
$\sigma_{inj\eta}$	< 0.01031
H/E	< 0.0597
PF charged hadron isolation	< 1.295
PF neutral hadron isolation	$< 10.910 + 0.0148 \cdot p_T + 0.000017 \cdot (p_T)^2$
PF photon isolation	$< 3.630 + 0.0047 \cdot p_T$
$ \eta $	< 1.4442
p_T	> 20 GeV
number of pixel seeds	0
$\Delta R(\gamma, \ell)$	> 0.3

The transverse mass m_T

If particles decay to invisible and visible objects, the invariant mass of the mother particle cannot be fully reconstructed. In contrast to the calculation of the invariant dilepton mass introduced above, invisible decay products are not measured in the detector. Only p_T^{miss} can be measured. In such cases, the transverse mass m_T of the mother particle can be reconstructed by using only transverse components of all involved four-momenta.

The transverse mass of two objects with transverse momenta \vec{p}_T^A and \vec{p}_T^B yields the transverse mass of the mother particle if both particle emerge from the same decay. It is defined as

$$m_T(\vec{p}_T^A, \vec{p}_T^B) = \sqrt{2|\vec{p}_T^A||\vec{p}_T^B|(1 - \cos(\Delta\phi))}, \quad (4.6)$$

where $\Delta\phi$ is the angle between \vec{p}_T^A and \vec{p}_T^B in the transverse plane.

In cases where one decay product is invisible and leaves the detector undetected, m_T is calculated under the assumption that the p_T of the invisible particle is described by p_T^{miss} . By definition, it has an upper limit at the actual mass of the mother particle, and yields therefore a good estimate for the mother particle mass.

The stransverse mass M_{T2}

In case of two identical particles, each decaying to one invisible and one visible particle, the stransverse mass M_{T2} [134, 135] is a useful generalization of m_T . In this analysis, it is calculated to estimate the mass of the NLSP, which decays to an invisible object, the gravitino, and one visible particle, a Z boson or a photon. It is defined as

$$M_{T2} = \min_{\vec{p}_T(\tilde{G}_1) + \vec{p}_T(\tilde{G}_2) = \vec{p}_T^{\text{miss}}} \left(\max \left[m_T(\vec{p}_T(Z), \vec{p}_T(\tilde{G}_1)), m_T(\vec{p}_T(\gamma), \vec{p}_T(\tilde{G}_2)) \right] \right), \quad (4.7)$$

where the final value is determined via minimization as indicated by "min" in the equation. Descriptively, the algorithm tries to estimate the transverse masses of the mother particles under the assumption that p_T^{miss} is composed of exactly one massless particle from each decay branch. For all signal models, the M_{T2} distribution has an upper limit at the mass of the lightest neutralino, while for all SM backgrounds M_{T2} yields much lower values in comparison to the high SUSY masses. See Figure 4.1 for a visualization of the described decay structure and an M_{T2} distribution.

The calculation of M_{T2} based on the reconstructed Z boson candidate, the photon, and p_T^{miss} performs better for the simplified models, since in these scenarios the bosons are always produced in the final NLSP decays. In the GMSB model on the other hand, both bosons can also be produced in the decays of different particles, such as the second lightest neutralino, depending on the wino and bino masses.

4.5. Lepton pair selection

In the analysis, different data sets selected with different dilepton triggers are combined, see Section 4.1. Therefore, it is possible that an event is contained in more than one data set. With the following procedure it is assured that no event is double counted. At first, all leptons per event are sorted by their transverse momenta. The leading and subleading² leptons are identified. Their flavor combination then determines the classification of the event as "dielectron" (ee), "dimuon" ($\mu\mu$), or "electron-muon" (e μ). For instance, a dielectron event is classified as such, if the event originates from the DoubleEG sample, both the leading and the trailing lepton are

²Called trailing from now on.

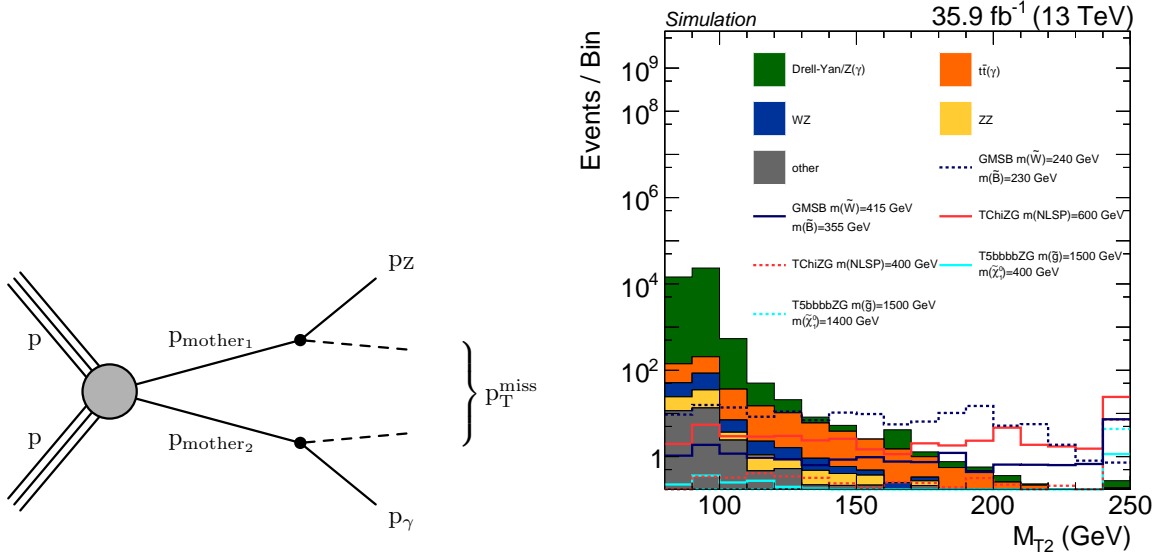


Figure 4.1.: Sketch of decays of pair produced particles to p_T^{miss} and a Z boson or a photon, respectively (left). Stacked background events and events for different signal points against the stransverse mass M_{T2} (right). Both are obtained from simulation. For each signal model, two different signal points are shown. For their masses refer to the legend in the plot.

electrons, and it is selected by at least one of the dielectron triggers. This set of conditions ensures the exclusivity of the three selections.

The trailing and leading lepton need to be separated at least by a distance of $\Delta R = 0.1$ in the transverse plane, and the invariant dilepton mass $m_{\ell\ell}$ should be larger than 50 GeV. The first requirement ensures, that no lepton candidate is counted twice, while the latter threshold is introduced, because the simulation of the Drell-Yan simulation does not include events with lower dilepton masses. The selection of targeted SUSY events is not harmed with this requirement, since the Z bosons are mainly produced on-shell in the NLSP decays. Events with lower invariant dilepton masses are not of interest for this analysis, since in the following only leptons originating from a Z boson decay are selected, resulting in an invariant dilepton mass around the Z boson mass of around 91 GeV.

Hereafter, the dielectron and dimuon selections are combined to a dilepton selection to increase the statistics in the validation, and especially in the signal region.

Additional leptons need to pass the same selection as the trailing lepton.

4.6. Triggers and trigger efficiency measurement

As pointed out in Section 4.1, the events are recorded with various dilepton triggers. For each dilepton combination (ee , $\mu\mu$, $e\mu$) multiple triggers are used because of the changing instantaneous luminosity over the 2016 run period, and different triggers were active at different times. The main trigger paths are isolated dilepton triggers, while non-isolated trigger paths are added to increase the efficiency for boosted topologies of the dilepton system. A list of all used HLT trigger paths is given in the appendix in Tables D.1 and D.2. While the same-flavor dilepton triggers (ee , $\mu\mu$) are used as signal triggers, the different-flavor triggers ($e\mu$) are used to select events needed for the background prediction of the top pair production ($t\bar{t}(\gamma)$) background. This is explained in more detail in Section 5.2.1. The various dilepton triggers altogether have transverse momentum thresholds for both leptons of around 17 – 33 GeV for the leading

lepton, and $8 - 33\text{ GeV}$ for the trailing lepton. Additional triggers with H_T or p_T^{miss} thresholds are relevant for the trigger efficiency measurement, which is presented in the following.

Trigger efficiency measurement

Measuring the trigger efficiency is essential to obtain appropriate transverse momentum requirements for the dilepton system. In the signal simulation using the FASTSIM package no trigger simulation is performed, while it is done for the SM background samples. Therefore, the efficiency needs to be measured also on simulation, such that the signal simulation can be scaled accordingly. In addition, the SM simulation samples are weighted with a factor, correcting for differences in the efficiency between data and simulation.

A logical OR combination of all dilepton triggers with the same-flavor requirements is used. Thus, for an event only one of the used triggers has to be fired to be selected for the key analysis. The combined trigger efficiency ε is measured using a baseline trigger. The baseline trigger needs to be uncorrelated to the signal trigger which efficiency is being measured. In addition, the baseline trigger needs to provide a sufficient number of events to ensure a sample of events large enough to reduce the statistical uncertainty of the measurement. The signal trigger efficiency is defined as the number of events passing baseline and signal trigger, divided by the number of events passing only the baseline trigger:

$$\varepsilon = \frac{\text{baseline} \wedge \text{signal}}{\text{baseline}}. \quad (4.8)$$

As a consequence, the efficiency of the baseline trigger cancels, and the pure signal trigger efficiency is maintained. As baseline triggers, a combination of various triggers with H_T thresholds is used. These thresholds range from $200 - 800\text{ GeV}$ and all H_T baseline triggers except for the triggers with thresholds of $H_T > 200\text{ GeV}$ and $H_T > 800\text{ GeV}$ are prescaled over the 2016 run period, meaning that only every x -th event is recorded if x is the prescale factor.

The measurement is not performed on the dilepton data streams, but on the H_T data sets. The event selection consists of the lepton pair selection introduced in Section 4.5 with an additional $H_T > 200\text{ GeV}$ requirement to ensure that the baseline triggers are efficient. An additional matching between the selected leptons and the trigger objects responsible for the firing of the triggers is performed.

The so-called efficiency turn-on characterizes the slope around the trigger threshold due to differences in the online and offline reconstruction of the transverse momenta. Since dilepton triggers are used, the triggers consists of two triggering parts for each lepton, called trigger legs. Therefore, the efficiency turn-ons need to be determined for each lepton trigger leg separately. Resulting efficiency curves for all three dilepton combinations measured both on data and simulation are shown in Figure 4.2 against the p_T of the trailing lepton. The efficiency curves for the leading lepton legs are shown in Figure D.1 in the additional material. Statistical uncertainties of the individual bins are calculated using 68% confidence level (CL) Clopper-Pearson intervals [136].

The measurements suffer mainly from the available sample size in the H_T triggered data set, while the available number of simulated events is very high. The electron-muon channel is affected the most by this effect. However, the efficiency curves show the structure of multiple efficiency turn-ons, as it is expected from a combination of triggers with very different ranges of thresholds. As indicated by the dotted lines in the plots, the lepton p_T cut was determined to be 20 GeV for the trailing lepton, and 25 GeV for the leading one. Although the dielectron and electron-muon triggers are not yet fully efficient at this threshold, as it is the case for the dimuon

trigger, this requirement is imposed also on the other two selections in order to obtain a symmetric lepton selection, since both lepton channels are combined for the analysis, see Section 4.5. The mean plateau efficiencies are shown as gray bands with their statistical uncertainties in the plots. The mean efficiency is also measured on simulation, and all efficiency values are given in Table 4.5. These are obtained by requiring both leptons to pass the 25 GeV and 20 GeV threshold, respectively. As can be seen, these values do not differ very much from the values quoted in the plots, where no lepton p_T requirement in the selection is imposed. Thus, the leading lepton leg is nearly fully efficient, when the trailing lepton has a p_T larger than 20 GeV. Additional efficiency values for the same triggers obtained with a p_T^{miss} baseline selection, that are discussed in the following, are given, too. The efficiency curves after applying the p_T cuts, are also studied in various other distributions, e.g., H_T and p_T^{miss} , to assure the stability of the used triggers. These can be found in Section D.

Table 4.5.: Trigger efficiencies determined both on data and simulation for both baseline trigger configurations for the ee, e μ , and $\mu\mu$ channels.

baseline trigger	Data		Simulation	
	H_T	p_T^{miss}	H_T	p_T^{miss}
ee	$96.1^{+0.2\%}_{-0.2\%}$	$93.8^{+0.3\%}_{-0.3\%}$	$96.62^{+0.01\%}_{-0.01\%}$	$96.79^{+0.02\%}_{-0.02\%}$
e μ	$86.9^{+0.5\%}_{-0.5\%}$	$86.8^{+0.3\%}_{-0.3\%}$	$91.92^{+0.01\%}_{-0.01\%}$	$91.46^{+0.05\%}_{-0.05\%}$
$\mu\mu$	$92.6^{+0.3\%}_{-0.3\%}$	$93.9^{+0.3\%}_{-0.3\%}$	$97.71^{+0.01\%}_{-0.01\%}$	$97.63^{+0.02\%}_{-0.02\%}$

In addition, the agreement between rescaled simulation by the factor $\varepsilon' = \varepsilon_{\text{Data}} / \varepsilon_{\text{MC}}$ and data is shown in the ratio plots beneath the efficiency curves. It can be concluded, that the efficiencies agree within the systematic uncertainty, which is set to cover differences between data and simulation. It is determined to be 3%, and is indicated with the red uncertainty band in the plots.

As an additional independent check, the whole trigger efficiency measurement was performed also on p_T^{miss} data sets with p_T^{miss} baseline triggers, that have thresholds of around 110 – 600 GeV. This selected phase space region is more or less orthogonal the H_T selection. It is also closer to the phase space of the final signal region, since the signal region selection contains a p_T^{miss} threshold, see Section 5.1.2. Because the efficiency in the low H_T region cannot be studied with the H_T baseline selection due to the inherent inefficiency of these triggers, with the p_T^{miss} baseline selection this region can be covered. As can be read from Table 4.5, the values obtained from this method are also in agreement with the efficiencies measured using the H_T selection.

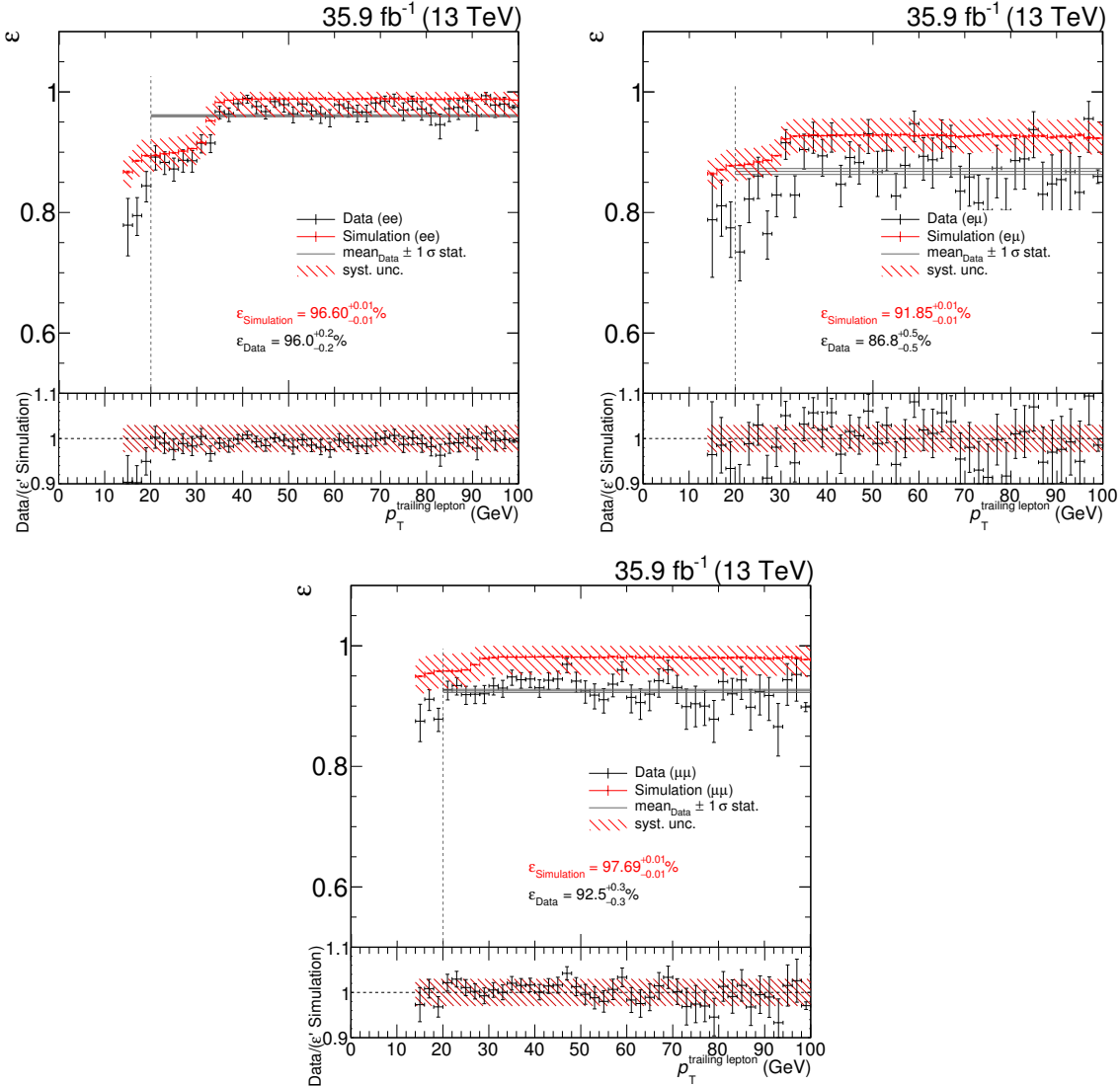


Figure 4.2.: Measurement of the combined efficiency for all dilepton trigger combinations on data (black) and simulation (red) for the ee (top left), eμ (top right), and μμ (bottom) channels. The measurement is performed using various H_T baseline triggers, while the selection consists of the lepton pair preselection, and a $H_T > 200 \text{ GeV}$ requirement. The mean of the data efficiency with its statistical uncertainty (gray band), and the 3% systematic uncertainty on the measurement (red band) are also shown. In the bottom panel of each plot, the ratio between the efficiency measured on data and the simulation scaled with the reweighting factor ϵ' is depicted.

Analysis strategy and background estimation

Contents

5.1. Event selection	41
5.2. Background estimation	45
5.3. Study of systematic uncertainties	58

Processes producing SUSY particles have significantly smaller cross sections than most SM processes. Therefore, a sophisticated understanding of the relevant production and decay scenarios is needed in order to separate the potential interesting events from the huge amount of SM background. Since this search is targeting SUSY scenarios with bino- and wino-like NLSPs, final states with photons and Z bosons are expected. Choosing the dileptonic decay of the Z boson, there are not many SM background processes leading to the investigated final state. Especially the additional requirement of a photon and p_T^{miss} in the events reduces most of the background, such that, e.g., the QCD background becomes negligible. Left over are processes producing two same-flavor opposite-charge (SFOC) leptons, one photon and missing transverse momentum. The most important ones are $t\bar{t}(\gamma)$ production, the combination of Drell-Yan Z/γ^* and $Z\gamma$ production, called Drell-Yan/ $Z(\gamma)$ from now on, ZZ, and WZ diboson production. This is discussed in more detail in Section 5.2.

The key strategy of this analysis is to obtain a event selection, so that many GMSB model scenarios can be investigated. Hence, only the existence of all expected final state particles is required, where the Z boson is reconstructed from the two selected leptons. Therefore, loose requirements on the lepton and photon energies can be imposed. Not many additional requirements are needed in the following to obtain a sensitive signal region selection.

5.1. Event selection

In this section, the event selection is discussed, including region definitions important for the background prediction, which is based on simulation. In those control regions, each enriched with a specific type of background events and suppressed signal contribution, the simulation is tuned to match the measured data. In an additional validation region, the background prediction is examined, and finally a two bin counting experiment is performed in the signal region.

5.1.1. Preselection

The preselection acts as a first rough definition of the phase space that is of interest, and rejects inefficient parts of the used triggers. The preselection imposed on the dilepton triggered events is defined as follows:

- exactly one SFOC lepton pair (ee or $\mu\mu$) as defined in Section 4.3,

- $p_T > 25 \text{ GeV}$ for the leading lepton,
- $p_T > 20 \text{ GeV}$ for the trailing lepton,
- at least one photon,
- $\Delta R(\ell_1, \gamma) > 0.3$ and $\Delta R(\ell_2, \gamma) > 0.3$,
- $81 \text{ GeV} < m_{\ell\ell} < 101 \text{ GeV}$.

The first four conditions imply the existence of the final state particles, including the definition of the physics objects and lepton pair selection explained above, and the p_T requirements determined in the trigger efficiency measurement. The fifth requirement reduces contributions of FSR photons. The invariant dilepton mass requirement ensures that only lepton pairs are selected, that originate from an on-shell Z boson decay, and reduces different contributions of SM backgrounds.

5.1.2. Signal region

The signal region (SR) selection is optimized to maintain high sensitivity for various SUSY scenarios both with electroweak and strong production. It is defined by the following criteria:

- $p_T^{\text{miss}} > 150 \text{ GeV}$,
- $M_{T2} > 100 \text{ GeV}$.

In the considered models, see Section 2.3.2, the NLSP can decay to a Z boson or a photon in combination with gravitinos \tilde{G} , which are undetectable and create missing transverse momentum in the event. Therefore, requiring p_T^{miss} to be larger in the selected events than in most of the SM background processes enables a good separation between SM background and SUSY signal. The p_T^{miss} threshold is not supposed to be too high, in order to maintain sensitivity to low neutralino masses as well. Additional high separation power is given by the stransverse mass M_{T2} , because it yields a good estimate of the NLSP mass, which is larger than the mass of SM particles. Also, there is no known SM particle which can decay into photons or a Z boson accompanied with neutrinos creating an momentum imbalance in the detector. Therefore, M_{T2} on average is much larger for SUSY processes than for SM processes. Both the M_{T2} and p_T^{miss} distributions of events fulfilling the preselection are shown in Figure 5.1 for the total background and signal points of each model. The final SR is divided in two search bins in the p_T^{miss} distribution, one ranging from 150 to 200 GeV, and the second one ranging from 200 GeV to infinity, see Section 6.1.

5.1.3. Control regions

Different control regions (CRs) are defined for the four main background processes, in order to develop a background prediction for each important background process. These CRs are built such that they are fully orthogonal to the signal region and among each other and include a large amount of events for precise studies and high purity. The main groups of backgrounds are $t\bar{t}(\gamma)$, DY/Z(γ), WZ, and ZZ production.

$t\bar{t}(\gamma)$ - control region

To obtain a CR for the $t\bar{t}(\gamma)$ background, the flavor symmetry of the process is exploited. The two W bosons of the top quark decays can decay independently with the same probability to an electron or a muon, resulting in a similar number of same-flavor and different-flavor final state events. The different-flavor triggers are needed to guarantee a basis data set containing a sufficient number of events. In addition, the background can be studied in the same high p_T^{miss} and M_{T2} regions as the SR. The preselection criteria need to be adjusted accordingly, resulting in a CR definition of

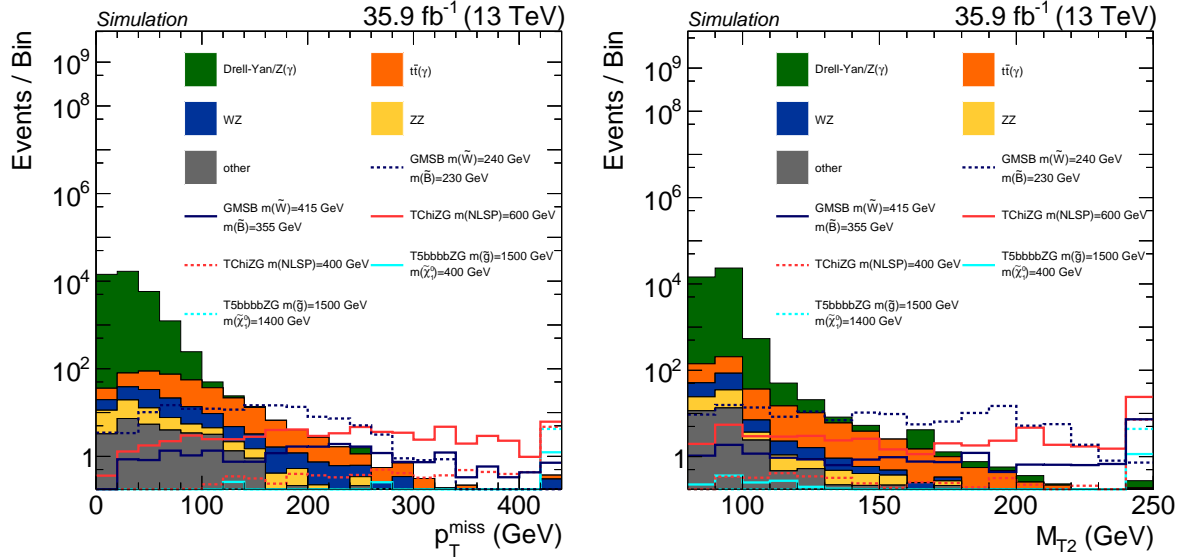


Figure 5.1.: Stacked background events and events for different signal points against p_T^{miss} (left) and M_{T2} (right). Both are obtained from simulation. For each signal model two different signal points are shown. For their mass parameters refer to the legend in the plots.

- exactly one different-flavor opposite-charge (DFOC) lepton pair ($e\mu$),
- at least one photon,
- $\Delta R(\ell_1, \gamma) > 0.3$ and $\Delta R(\ell_2, \gamma) > 0.3$.

The invariant dilepton mass window requirement is removed from the preselection, since the reconstructed dilepton mass is not necessarily in coincidence with the Z boson mass. In contrast, it shows a broad distribution because the leptons are not originating from the same mother particle. The requirement being responsible for the orthogonality to the SR is the different dilepton flavor requirement.

Drell-Yan/Z(γ) - control region

The Drell-Yan/Z(γ) background has nearly the same phenomenological topology as the SUSY signal, except for lower missing transverse momentum on average, since it mainly originates from mismeasurements of jets. The final control region definition additionally to the preselection is

- $p_T^{\text{miss}} < 100$ GeV.

This region is orthogonal to the SR due to the inverted p_T^{miss} requirement.

WZ - control region

In order to obtain a high purity WZ control region, the selection criteria are adjusted such that the fully leptonic decay of the diboson system is studied. As in the preselection, a SFOC lepton pair is required, but the additional lepton veto is inverted. Hence, the existence of a third lepton is required. Since the leptonic W boson decays are selected, with the help of additional p_T^{miss} and m_T requirements the purity of the selection of WZ diboson production events is enhanced. The transverse mass m_T is calculated using the third lepton and the missing transverse momentum, and is therefore an estimate for the W boson mass. In the identification of the lepton pair belonging to the Z boson, all combinations fulfilling flavor and charge requirements are tested. In case of multiple valid combinations, the combination with the invariant dilepton mass closest

to the Z boson mass is chosen. To ensure a selection with a suitable amount of data, since the cross section for diboson production is rather low, the requirement of the existence of at least one photon from the preselection is removed. The final region selection is

- exactly one SFOC lepton pair (ee or $\mu\mu$),
- exactly one additional third lepton (e or μ),
- $\Delta R(\ell_1, \gamma) > 0.3$ and $\Delta R(\ell_2, \gamma) > 0.3$,
- $81 \text{ GeV} < m_{\ell\ell} < 101 \text{ GeV}$ (for the SFOC lepton pair),
- $p_T^{\text{miss}} > 70 \text{ GeV}$,
- $m_T(\vec{p}_T^{\text{miss}}, \vec{p}_T(\ell_3)) > 50 \text{ GeV}$.

ZZ - control region

The strategy to achieve a pure ZZ diboson selection that does not overlap with the SR selection is very similar to the WZ CR selection described above. By selecting events, where both Z bosons decay leptonically to charged leptons (ee or $\mu\mu$), per definition an exclusive control region is obtained. As in the WZ CR selection, flavor and charge requirements are considered to construct Z boson candidates from the four selected leptons. In cases, where multiple valid solutions for the reconstruction of two Z bosons exist, the possibility with the first Z boson candidate mass closest to the nominal Z boson mass is chosen. The second Z boson candidate has to fulfill a looser mass agreement compared to the first one. Also, the existence of a photon in the event is not required. In total, the selection criteria are

- exactly two SFOC lepton pairs (ee or $\mu\mu$),
- $\Delta R(\ell_1, \gamma) > 0.3$ and $\Delta R(\ell_2, \gamma) > 0.3$ for the first pair,
- $76 \text{ GeV} < m_{\ell\ell} < 106 \text{ GeV}$ for the mass of the first Z boson candidate,
- $50 \text{ GeV} < m_{\ell\ell} < 130 \text{ GeV}$ for the mass of the second Z boson candidate.

5.1.4. Validation region

An additional validation region (VR) is constructed, where the developed background predictions are verified by performing data-to-background prediction comparisons. Therefore, it is convenient to choose a VR close in phase space to the SR. This is achieved by applying the same selection requirements as for the SR, but demanding either the p_T^{miss} or the M_{T2} requirement to be inverted. The VR must also not overlap with the DY/Z(γ) CR, thus a minimal p_T^{miss} requirement needs to be imposed. The selection requirements for the VR in addition to the preselection are the following:

- $p_T^{\text{miss}} > 100 \text{ GeV}$,
- either $p_T^{\text{miss}} < 150 \text{ GeV}$ or $M_{T2} > 100 \text{ GeV}$.

A visualization of the signal, validation, and DY/Z(γ) control region definitions in the M_{T2} - p_T^{miss} plane can be found in Figure 5.2. Two dimensional histograms for the number of expected events motivating the region definitions are shown in Figure 5.3 for all background processes, together with distributions of different benchmark signal points for all three considered signal models. These distributions show also specific features of the considered signal models regarding important kinematic observables. Because the TChiZG model is a one parameter scan, and the only free parameter is the NLSP mass, together with the momentum of the NLSP it directly determines the maximum amount of transverse momentum for the decay products and thus directly the Z boson p_T and the p_T^{miss} originating from the gravitinos. Also, the endpoint of the

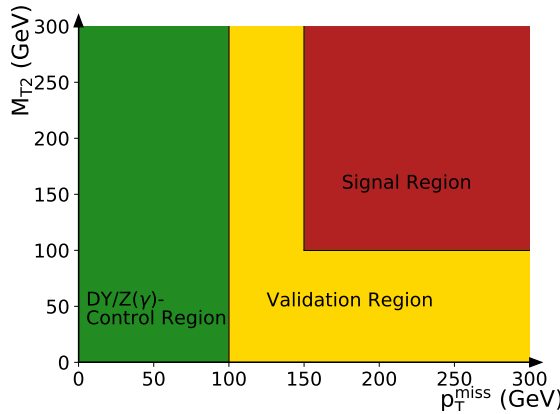


Figure 5.2.: Visualization of the definition of the signal, validation, and DY/Z(γ) control region in the M_{T2} - p_T^{miss} plane.

M_{T2} distribution is of the same order and coincides with the NLSP mass. Hence, p_T^{miss} and M_{T2} calculated from the bosons and p_T^{miss} are strongly correlated for this specific model.

For the strong SMS this is not directly the case. Since this SMS is a two dimensional parameter scan, the event kinematics also depend on the mass difference of the gluino and the NLSP mass, as discussed in Section 2.3.2. In cases where the mass difference is small, the kinematics evolve similar as for the EWK SMS, while for larger mass differences, as shown in Figure 5.3, the correlation between M_{T2} and p_T^{miss} is much weaker and the distributions are much broader.

The distributions of the GMSB model behave similar to the electroweak SMS, depending on the wino and bino masses.

The signal events mainly populate the SR for all models, with small contributions in the CRs and the VR, while the majority of the background events contribute to the DY/Z(γ) CR and a minor part to the VR. Only a minority of the background events are expected in the SR. Hence, in total a good separation between background and signal is achieved.

5.2. Background estimation

In this section, the used background estimation methods are discussed, including the study of systematic effects. The total background is composed of $t\bar{t}(\gamma)$ production, Drell-Yan and $Z(\gamma)$ events, WZ and ZZ diboson production, and a remaining group of backgrounds ("other"), composed of, e.g., single top and triboson production (See Section 4.2 and Section 5.1.3). The relative contributions for all background processes in the two SR bins are depicted in Figure 5.4. The most dominant background is $t\bar{t}(\gamma)$, followed by WZ, ZZ, and Drell-Yan/ $Z(\gamma)$.

The leptonic decays of the top pairs generated in association with a photon significantly contribute to the SR, because the final state signatures appear very similar to those of the SUSY models and the production cross section is very high. If both W bosons decay leptonically, a SFOC lepton pair in connection with neutrinos can be produced, creating a large amount of p_T^{miss} in the detector. Prompt photons can be produced in the hard interaction, or can be radiated off in the initial or the final state by participating charged particles. Since the two selected leptons of the $t\bar{t}$ system decay originate from different mother particles, the reconstructed invariant mass distribution is broad and shows no resonance. Due to the high cross section of $t\bar{t}(\gamma)$ production, see Table 4.1, there is a sufficient probability to measure an invariant dilepton mass close to the Z boson mass although the two leptons do not emerge from it.

In the Drell-Yan process and in $Z\gamma$ production, an on-shell Z boson is produced, thus the $m_{\ell\ell}$ requirement for the dileptons in the SR is fulfilled. Although a photon can be produced addi-

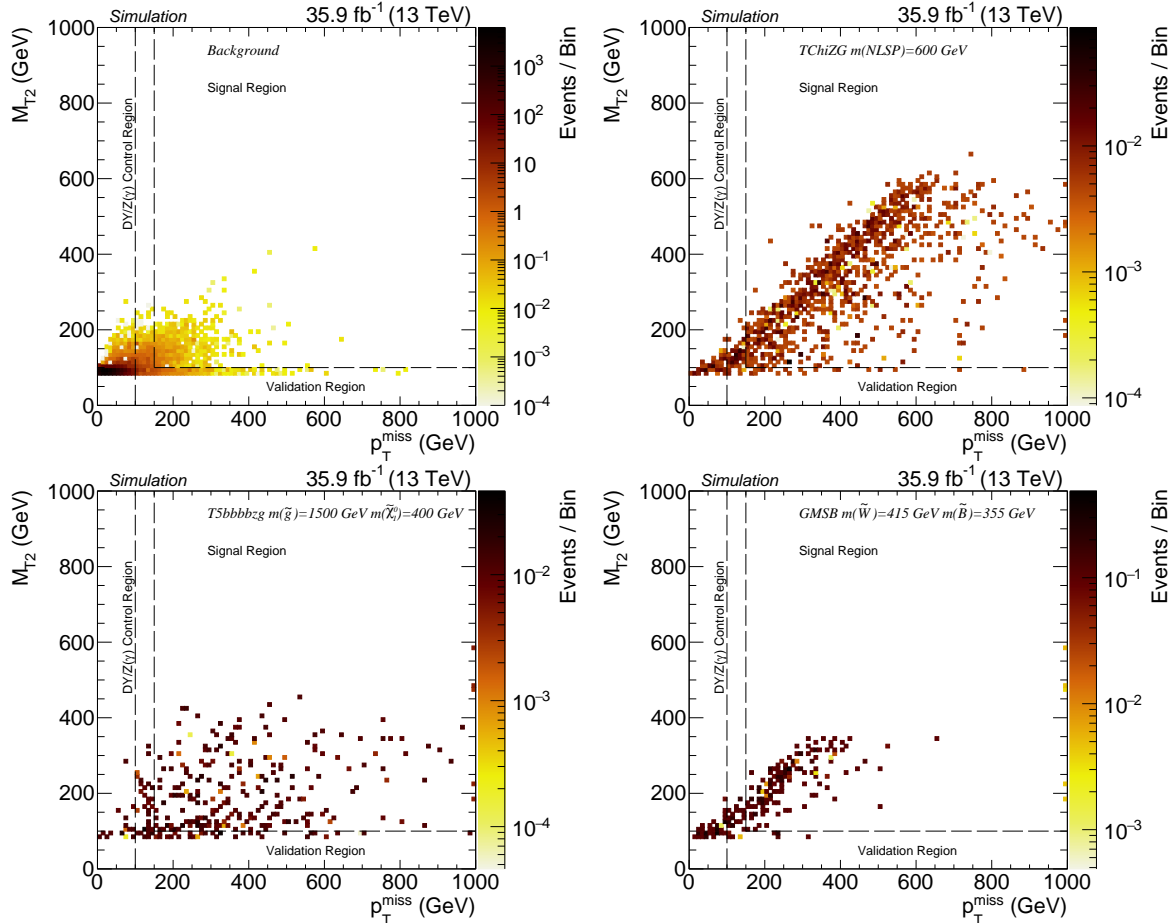


Figure 5.3.: Distribution of the total number of expected background events in the M_{T2} - p_T^{miss} plane (upper left). Distributions for the number of expected signal events for the TChiZG SMS with an NLSP mass of 600 GeV (upper right), the T5bbbbZG SMS with a gluino mass of 1.5 TeV and a neutralino mass of 400 GeV (bottom left), and the GMSB model with $m(\tilde{W}) = 455 \text{ GeV}$ and $m(\tilde{B}) = 355 \text{ GeV}$ (bottom right).

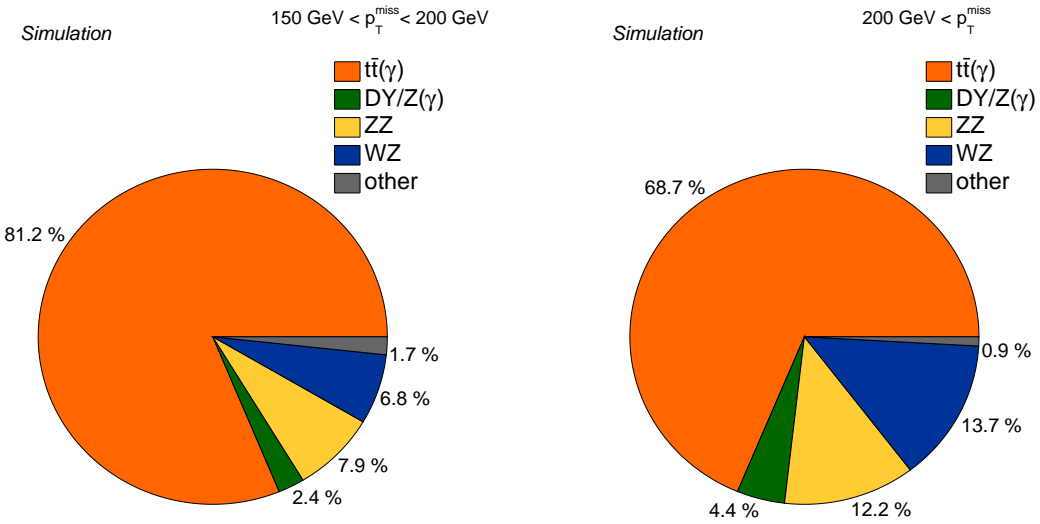


Figure 5.4.: Relative amounts for all groups of considered backgrounds for the two search bins in the SR.

tionally, this background does not contribute significantly to the SR, because only nongenuine p_T^{miss} is generated in the process due to mismeasurements and therefore the p_T^{miss} distribution is steeply falling.

WZ production is also an important background for this search, since the W boson can decay leptonically and therefore creates a sufficient amount of genuine p_T^{miss} to pass the SR requirements, but is also suppressed by the M_{T2} requirement. While a photon can be generated in all possible radiation processes, an additional electron or jet originating from the W boson can fake a photon signature in the detector. In cases of appearance of photons, events can contribute, where the additional lepton does not pass the acceptance, reconstruction, and identification criteria.

Lastly, the ZZ event signature can be very similar to the one expected from the considered SUSY signals. One boson can decay to a pair of charged leptons, while the other decays to neutrinos, leading to a large amount of p_T^{miss} in the event. Together with FSR or ISR of a photon, ZZ background events show a signature very similar to the signal topology.

If the different background processes are compared, the diboson processes have more similar event kinematics than the $t\bar{t}(\gamma)$ process compared to the signal processes, but due to the lower diboson production cross sections the $t\bar{t}(\gamma)$ background dominates the other contributions.

The background prediction is based on simulation for all backgrounds. As mentioned in Section 5.1.3, different CRs are developed, that are enriched with corresponding background events. In those CRs, scale factors (SF) α_i are calculated by scaling the simulation to the measured data yield. Contributions of other backgrounds in the CR are considered in the calculation by fixing their contribution. The SFs are calculated via the following formula:

$$1 = \frac{D}{F + \alpha_i \cdot B} \quad (5.1)$$

$$\Rightarrow \alpha_i = \frac{D - F}{B}, \quad (5.2)$$

where B is the number of background events that are to be scaled, F the number of fixed background events, and D the number of measured data events. Due to the used method, which is performed similarly in each CR, possible uncertainties on the normalization of the predicted

distributions cancel, and only uncertainties in the shape need to be considered, see Section 5.3. The uncertainty arising from the SF calculation is purely of statistical origin, and is calculated via error propagation

$$\sigma_{\alpha_i}^2 = \sigma_D^2 \cdot \left(\frac{D}{B}\right)^2 + \sigma_F^2 \cdot \left(\frac{F}{B}\right)^2 + \sigma_B^2 \cdot \left(\frac{D - F}{B^2}\right)^2, \quad (5.3)$$

where σ_i are the corresponding statistical uncertainties to D , F , and B . These are assumed to be uncorrelated Poissonian uncertainties, and can be calculated via $\sigma_i = \sqrt{N_i}$, where N is the associated integral of events in the selection. In case of the simulation, for the calculation of the SF the normalized event yield is used, whereas in the error calculation the pure MC event count is considered to reflect the underlying statistical precision of the simulation. This method is referred to as the "integral method" in the following.

In each CR, all other background contributions have an influence, since their contributions are not negligible. Therefore, the order of SF determination can introduce a bias. To minimize this effect, the SFs are calculated in descending order of the purity of the background sample. At first, the ZZ SF is determined, followed by DY/Z(γ), $t\bar{t}(\gamma)$, and WZ. However, the background estimations are discussed in a different order, starting with the most important background, $t\bar{t}(\gamma)$. The systematic uncertainty arising from the choice of order is discussed in Section 5.3. To strengthen the confidence in the outcome, Kolmogorov-Smirnov (KS) [137] tests are performed to study the agreement of measured and predicted shape, which are based on the largest deviation between the two compared distributions. Resulting KS-values from the tests results are quoted on the corresponding plots for each individual distribution in the related sections. KS-values $\ll 1$ indicate disagreement between the input distributions, otherwise the distributions are considered to match.

In order to study a possible bias of observables not well modeled within the simulation, additional cross checks are performed. Similar to the SF calculation in the integral method, SFs are determined via χ^2 -minimization in the same CRs. Albeit this method is somewhat correlated to the method explained above, it enables the possibility to study influences of different distributions in different binnings. Therefore, for the final SF determination the integral method is preferred over the χ^2 -method, since it is independent of the choice of any observable or binning, and the resulting values for α_i agree between both methods. Thus, the χ^2 -fits serve only as additional cross-checks. In order to obtain the SF via χ^2 -minimization, α_i is varied in a range in small steps for each binning and distribution, and for every iteration the simulation is scaled and the χ^2 is calculated, which is defined as:

$$\chi^2 = \sum_i^{N_{bins}} \frac{\left(N_i^{obs} - N_i^{pred}\right)^2}{N_i^{pred}}. \quad (5.4)$$

The best fit value is determined to be at the minimum of the χ^2 -distribution, which is obtained by fitting a polynomial of fourth grade to the χ^2 -distribution. Ideally the measured χ^2 -distribution would be described by a parabola, but in order to account for asymmetries in the determined distribution, a higher order polynomial is chosen as the fit function. In addition, the fits do not have a statistical influence, but are only needed to extract the best fit value and its uncertainty, which is also of statistical origin. It is calculated by taking the difference between the best fit value and the values, corresponding to $\chi^2 = \chi_{BestFit}^2 + 1$. An example fit in the p_T^{miss} distribution is shown in Section 5.2.1 in the discussion of the $t\bar{t}(\gamma)$ background estimation. The number of degrees of freedom (ndf) is given by the number of bins used to obtain the χ^2 -distribution reduced by the number of parameters that are being optimized. The only free parameter is α_i , so ndf equals the number of bins subtracted by unity.

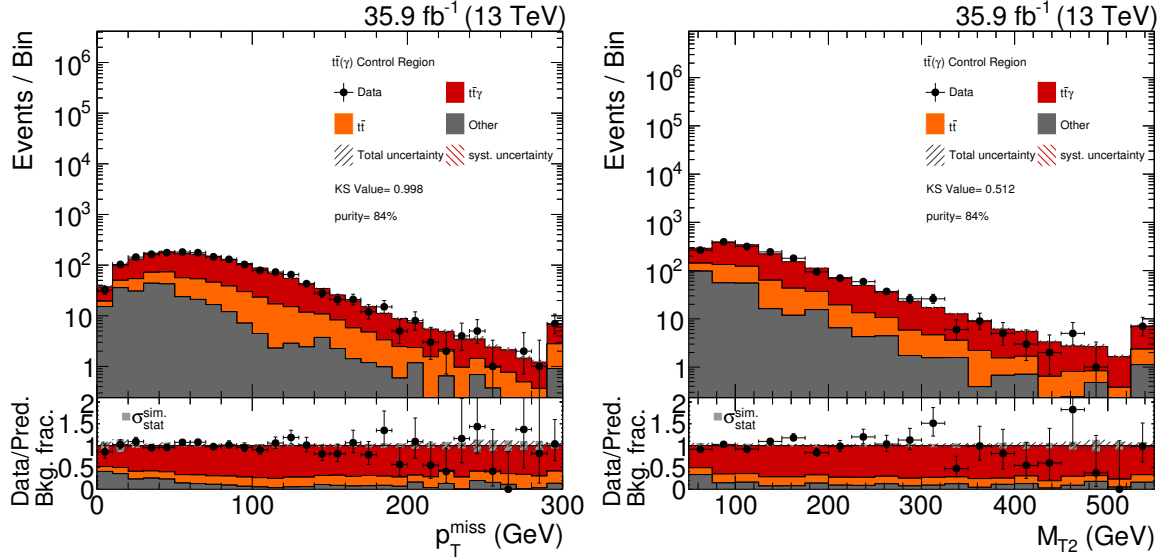


Figure 5.5.: Comparisons between data and rescaled simulation in the $t\bar{t}(\gamma)$ CR in the p_T^{miss} and M_{T2} distribution. Below each plot, a ratio between data and prediction is shown. The uncertainty bands correspond to the systematic (red) and total uncertainty (gray). In addition, in the ratio plot the relative composition of the backgrounds is visualized. KS-values for the performed Kolmogorov-Smirnov test and the selection purity are also quoted.

After determining all SFs, the background prediction is tested in the VR. Therefore, the simulated backgrounds in the VR are scaled accordingly, and the result is investigated, see Section 5.2.6.

5.2.1. Top pair production

As shown in Figure 5.4, the main background contribution is $t\bar{t}(\gamma)$, which is composed of top pair production ($t\bar{t}$) with and without photon radiation, and top-pair production in association with a photon ($t\bar{t}\gamma$), while the latter dominates. Both compositions are determined together by rescaling the simulation, such that the integral of events of the simulation in the CR matches the integral of events in data as explained in Section 5.2. The overall purity of the selection is of the order of 84%. With the integral method applied, the SF is obtained and given by

$$\alpha_{t\bar{t}(\gamma)} = 0.80 \pm 0.03(\text{stat.}) [\hat{=} 4.0\%]. \quad (5.5)$$

After application of $\alpha_{t\bar{t}(\gamma)}$, the numbers of events in data and simulation match per definition. Since the analyzed final state in this CR is very sensitive to higher order effects such as jet and photon radiation, and complex matrix elements are needed to describe the hard interaction, a SF differing from unity meets the expectation. NNLO electroweak effects can cause negative corrections for example due to destructive terms in higher order corrections. The uncertainty of the order of 4% indicates, that a sufficient number of events is present in the corresponding CR. The resulting prediction shows a good agreement with data, as can be seen from the p_T^{miss} and M_{T2} distributions in the CR after rescaling in Figure 5.5. The uncertainty of the fit method is of statistical origin, and is treated as a systematic uncertainty in the following. The agreement of additional important observables, such as the transverse momentum of the photon and both leptons, is also investigated, and no systematic deviation was found. Additional statistical checks, such as Kolmogorov-Smirnov tests and χ^2 -fits, as explained above are also performed. The resulting KS-values of the Kolmogorov-Smirnov tests quoted in each plot indicate a good

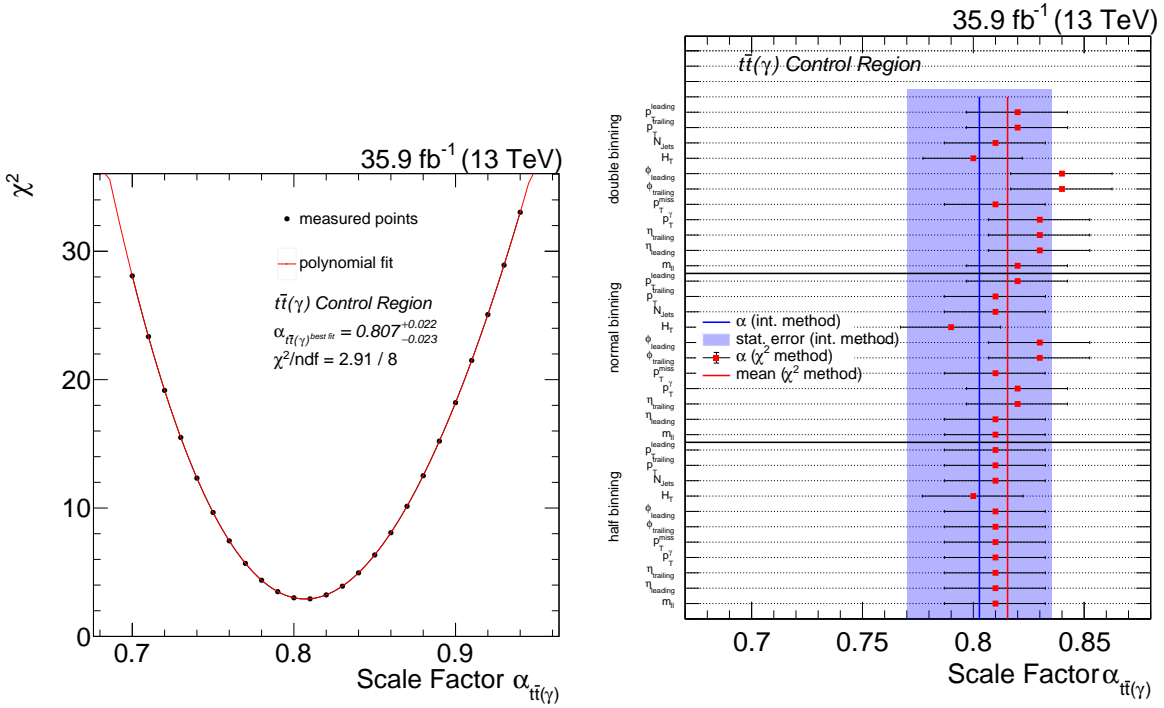


Figure 5.6.: Example χ^2 -fit in the $t\bar{t}(\gamma)$ CR in the p_T^{miss} distribution (left) with the polynomial fit. All fit results compared with the SF obtained from the integral method in different binnings and variables (right).

shape agreement.

The resulting curves of the χ^2 -fit distributions, see Figure 5.6 left for an example fit in the p_T^{miss} distribution, are smooth, indicating a proper performance of the fit. A comparison of all obtained SFs for the different setups and the SF obtained by the integral method is shown in Figure 5.6 right. No significant deviation is observed, and all SFs are in agreement with each other. Hence, the scaling of the $t\bar{t}(\gamma)$ background seems stable and well described in the CR.

Further studies

Since the $t\bar{t}(\gamma)$ background is the most dominating one, further studies are performed in which the underlying MC simulation samples and their combination are examined. Different overlap removal procedures, see Section 4.2, and different available cross sections are used, while the fit procedure itself is varied. In addition, available corrections to improve the modeling of jet radiation in the initial state, and corrections to enhance the description of the top quark p_T distribution, that are used both to correct the LO samples and the samples that are generated with POWHEG (see Section 4.2), are applied in different combinations. The used fit methods include a χ^2 -template fit, where the ratio between the fractions of the $t\bar{t}$ and $t\bar{t}\gamma$ simulation is left free as an additional parameter, and a fit where only the $t\bar{t}\gamma$ simulation is made use of. The additional corrections to improve the modeling of the top quark p_T distribution and the initial state jet radiation are observed to be unnecessary, because the modeling of the related distributions, i.e. the jet multiplicity and the lepton p_T distributions, is already in agreement with data in the standalone simulation. Using only the $t\bar{t}\gamma$ simulation yields the best agreement between simulated and observed shape, but is unphysical due to the missing $t\bar{t}$ process. For this reason, also the template fit method gives rise to similar results, since in the fit the $t\bar{t}\gamma$ sample has the highest impact due to the good shape agreement. Therefore, this approach is discarded,

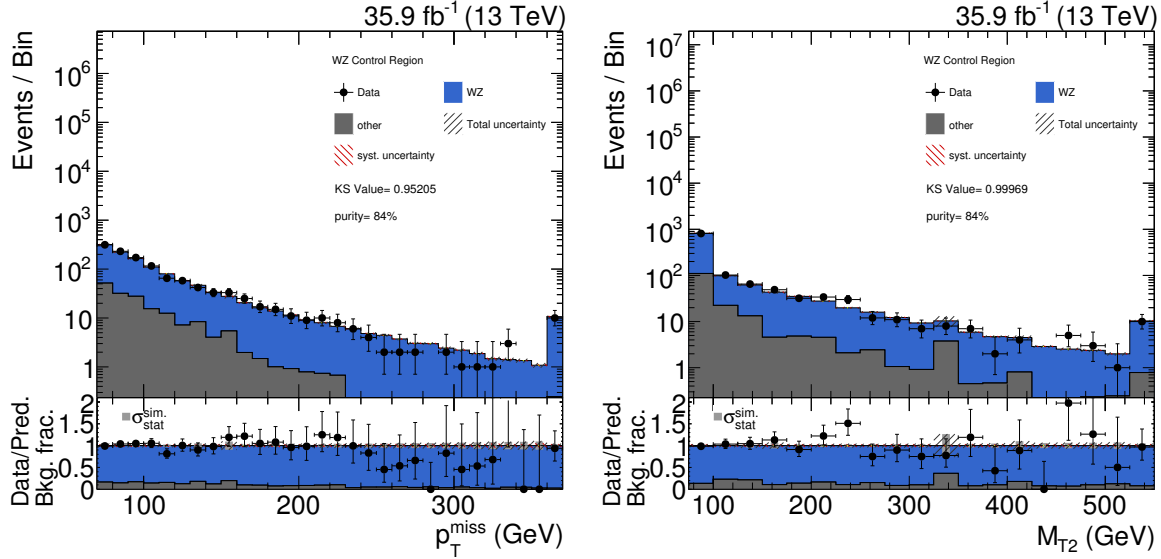


Figure 5.7.: Comparisons between data and rescaled simulation in the WZ CR in the p_T^{miss} and M_{T2} distribution. Below each plot, a ratio between data and prediction is shown. The uncertainty bands correspond to the systematic (rand) and total uncertainty (gray). In addition, in the ratio plot the relative composition of the backgrounds is visualized. KS-values for the performed Kolmogorov-Smirnov test and the selection purity are also quoted.

too. Eventually, no substantial variations regarding the background prediction are observed, and the best performance and stability is provided by the approach explained above.

5.2.2. WZ diboson production

The diboson production of WZ pairs is the second important background contribution for this analysis. It is also tuned to agree with the measurement in the WZ CR, while the SF α_{WZ} is calculated with the integral method. The expected purity of selected WZ events in this CR is about 84%. The SF α_{WZ} is determined to be

$$\alpha_{\text{WZ}} = 1.14 \pm 0.04(\text{stat.}) [\hat{=} 3.2\%]. \quad (5.6)$$

Higher order effects can lead to larger cross sections as calculated within the NLO simulation, thus it is not unexpected to obtain a SF varying from unity. Resulting distributions of the description of the p_T^{miss} and M_{T2} variables are shown in Figure 5.7. As can be seen, the predicted shape is in consistency over the whole range with the observed data, also in the high p_T^{miss} and M_{T2} regime. This is further confirmed by the additional cross checks, that are also realized in the $t\bar{t}(\gamma)$ CR described above. The KS-values close to one strengthen the trust in the background estimation method. The χ^2 -fit studies lead to the same outcome as can be seen in Figure 5.8.

5.2.3. ZZ diboson production

The third biggest background contribution is ZZ diboson production, where both Z bosons decay leptonically, one to charged leptons such as electrons or muons, and the other one to neutrinos. To simplify the construction of a dedicated CR, as explained in Section 5.1.3, the simulation procedure is exploited. Since the simulation of the events is the same for both charged leptons and neutrinos, that being produced in the Z boson decays, due to the identical generator, only the detector response differs. Therefore, the ZZ background can be well estimated in a four lepton CR. A pure selection of ZZ events can be established, although the statistics in data is

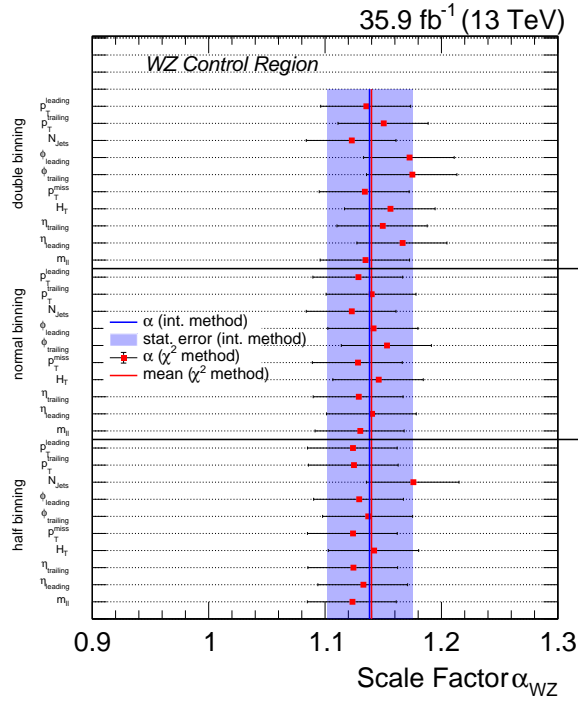


Figure 5.8.: All χ^2 -fit results compared with the SF obtained from the integral method in different binnings and variables.

quite low due to small cross section and the low branching fraction for the $Z \rightarrow \ell\ell$ decay. The selection purity is nearly 100%. With the integral method applied, the SF α_{ZZ} is given by

$$\alpha_{ZZ} = 1.11 \pm 0.06(\text{stat.}) [\hat{\pm} 5.7\%]. \quad (5.7)$$

Post-fit distributions in the p_T^{miss} distribution and invariant dilepton mass distribution of the second Z boson can be found in Figure 5.9. As mentioned, the precision is limited by the low statistics of the selected sample, but nevertheless is sufficient enough to establish a stable background prediction. The shapes agree well, as it is additionally indicated by the KS-values printed on the plots. The properties of the $ZZ \rightarrow 4\ell$ process does not allow to study the prediction in the high p_T^{miss} regime, since only nongenuine p_T^{miss} is produced. However, based on the agreement of distributions of the third and fourth leptons, such as $m_{\ell_3\ell_4}$, and the agreement of the description of nongenuine p_T^{miss} , the agreement of p_T^{miss} in the $ZZ \rightarrow 2\ell 2\nu$ background can be assumed. The χ^2 -fit studies, see Figure 5.10, are performed as for the other three background estimations discussed above, and yield the same conclusion, although some fluctuations in the choice of the variable or binning are present due to the lower total event count in the observed data. All in all also this background estimation method is stable.

5.2.4. Drell-Yan and $Z\gamma$ production

Although the contribution from the Drell-Yan and $Z\gamma$ backgrounds is small in the two SR bins, its contribution is the fourth largest. As in the case of the $t\bar{t}(\gamma)$ background, it is composed of two major parts, the Drell-Yan process, where quarks annihilate to off-shell photons or Z bosons and generate leptons in their decays, and the diboson production of $Z\gamma$. The integral method as explained above is used to determine the SF $\alpha_{DY/Z(\gamma)}$ in the dedicated CR defined in Section 5.1.3. The resulting SF is determined to be

$$\alpha_{DY/Z(\gamma)} = 1.066 \pm 0.001(\text{stat.}) [\hat{\pm} 0.87\%]. \quad (5.8)$$

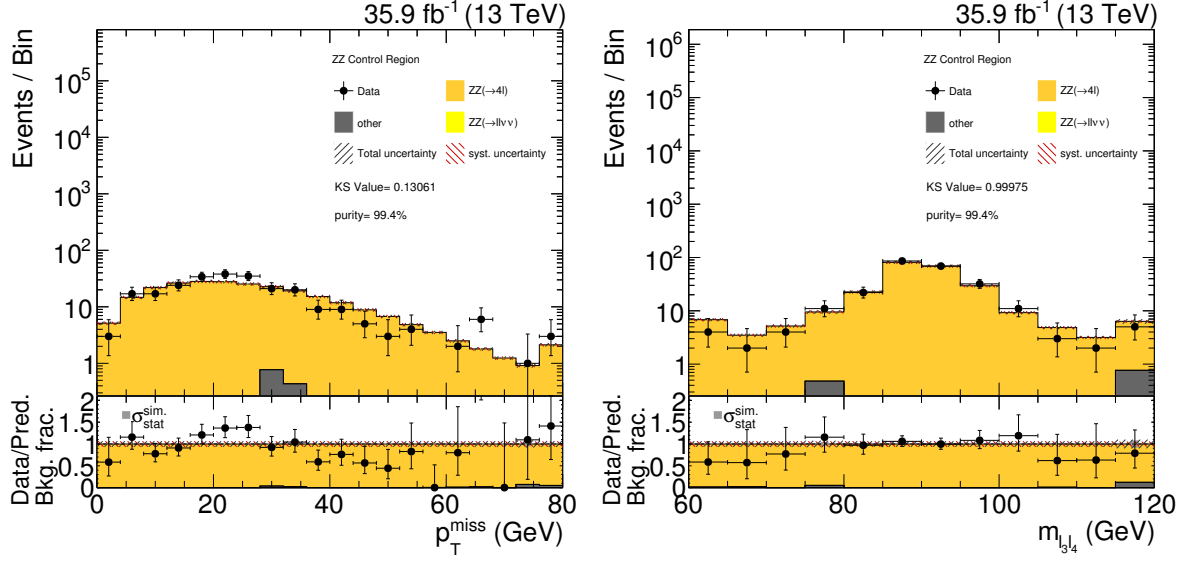


Figure 5.9.: Comparisons between data and rescaled simulation in the ZZ CR in the p_T^{miss} and $m_{\ell_3 \ell_4}$ distribution. Below each plot, a ratio between data and prediction is shown. The uncertainty bands correspond to the systematic (red) and total uncertainty (gray). In addition, in the ratio plot the relative composition of the backgrounds is visualized. KS-values for the performed Kolmogorov-Smirnov test and the selection purity are also quoted.

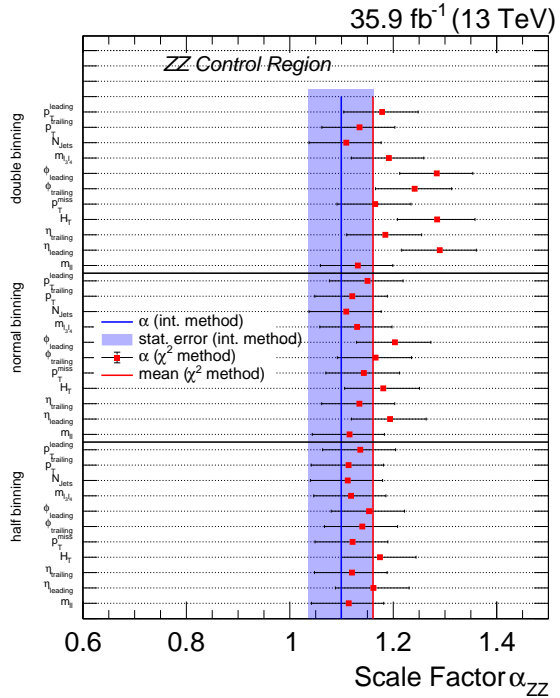


Figure 5.10.: All χ^2 -fit results compared with the SF obtained from the integral method in different binnings and variables.

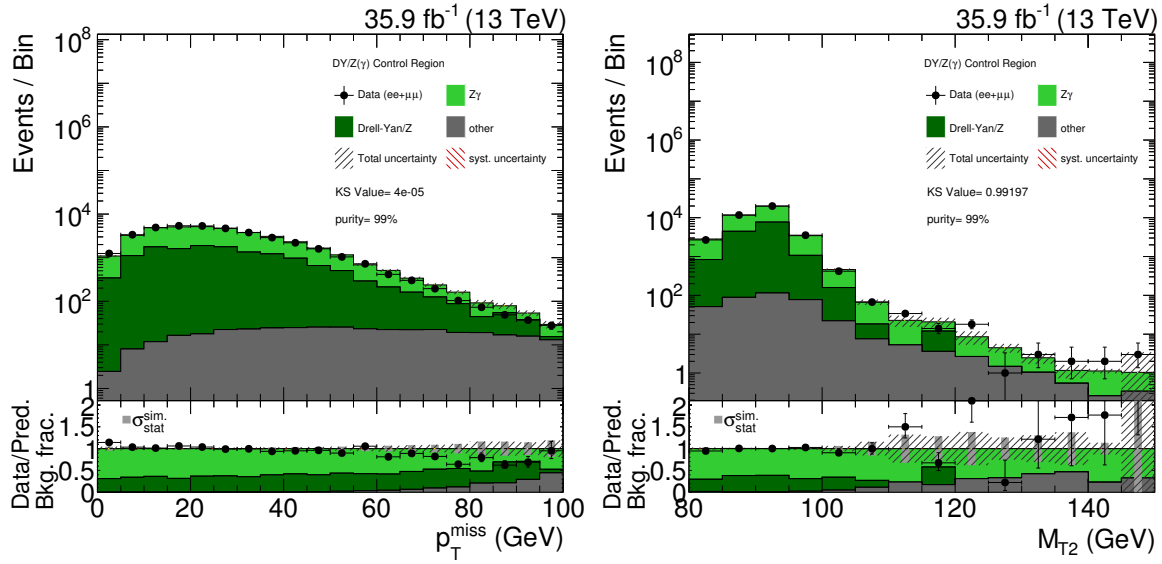


Figure 5.11.: Comparisons between data and rescaled simulation in the $DY/Z(\gamma)$ CR in the p_T^{miss} and M_{T2} distribution. Below each plot, a ratio between data and prediction is shown. The uncertainty bands correspond to the systematic (red) and total uncertainty (gray). In addition, in the ratio plot the relative composition of the backgrounds is visualized. KS-values for the performed Kolmogorov-Smirnov test and the selection purity are also quoted.

With a purity of about 99%, and a large total event count, a precise SF determination is feasible, as can be concluded also from the small statistical uncertainty of around 1%. The agreement between simulation and data is very good even before application of $\alpha_{DY/Z(\gamma)}$, since the SF equals nearly unity. The post-scaling distributions of p_T^{miss} and M_{T2} are shown in Figure 5.11. They show overall a good agreement, only in the high M_{T2} region there are some fluctuations due to the limited statistics being present both in data and simulation. Most of the KS-values indicate a very good matching between predicted and observed shape, albeit the Kolmogorov-Smirnov test provides a very small KS value for the consistency between the p_T^{miss} distributions. This is mainly due to the high statistics in data and therefore a higher absolute discrepancy, in contradiction to the lower statistics in simulation, leading to larger fluctuations. These discrepancy is also visible in the ratio in the bottom panel of the plot, but is consistent with the shown total uncertainty.

The χ^2 -fit studies shown in Figure 5.12 show good agreement over all variations.

5.2.5. Other standard model backgrounds

Additional minor backgrounds, such as $WZ\gamma$, $WW\gamma$, WW , and $W\gamma$ production, the production of W bosons in association with jets, and single top processes as listed in Table 4.1, are taken from plain simulation after reweighting them as described in Section 4.2 to the measured luminosity and NLO and NNLO cross sections.

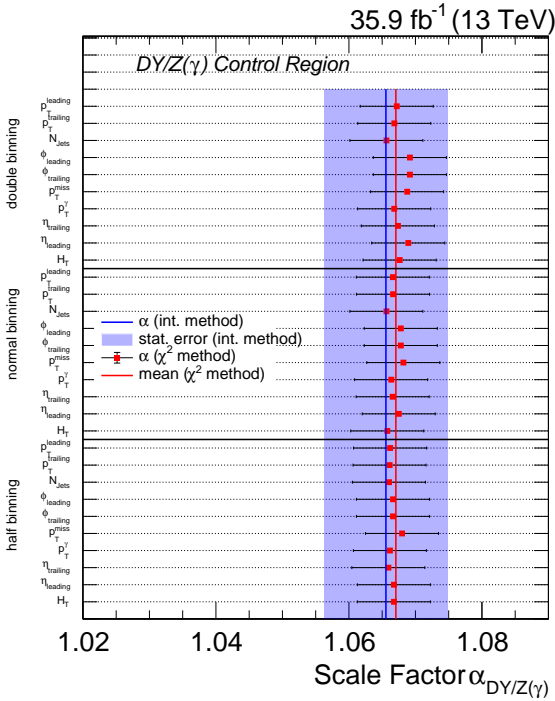


Figure 5.12.: All χ^2 -fit results compared with the SF obtained from the integral method in different binnings and variables.

5.2.6. Validation of the background estimation

After all main backgrounds are estimated using the corresponding CRs where the SFs are determined, the background prediction is validated in the VR defined in Section 5.1.3. The VR is orthogonal to the SR while being not signal sensitive and kinematically similar to the SR. Therefore, the VR is ideal to study the obtained background prediction.

Resulting comparisons between prediction and observed data in different distributions are shown in Figure 5.13 for the most important variables, such as p_T^{miss} and M_{T2} , together with p_T distributions of the leading and trailing lepton. Comparisons for the photon p_T and the invariant dilepton mass $m_{\ell\ell}$ distributions are shown in Figure 5.14.

Overall, the agreement is good in all distributions, although being limited by the low statistics in some kinematic regions. The largest deviation is observable in the p_T^{miss} distribution, but is consistent with the measured data within the statistical uncertainty in all bins. Statistical fluctuations of the DY/Z(γ) background are present, leading to such discrepancies. Although this background has an influence in the VR, its contribution in the SR is very small. Hence, the background prediction in the SR is not affected. In addition, Kolmogorov-Smirnov tests are performed to gain more trust in the background prediction. As can be read from the resulting KS-values, each quoted on the corresponding plot, the predicted and observed shapes agree well considering statistical uncertainties and systematic uncertainties, also in the p_T^{miss} distribution. Here, the shown systematic uncertainty originates merely from the statistical ones from the integral method. With 97 data events measured and 93.9 predicted, also the total number of events match between prediction and data.

Therefore, the background is assumed to be stable in the SR due to the similar kinematics in the VR based on the design as a kinematic sideband in p_T^{miss} and M_{T2} .

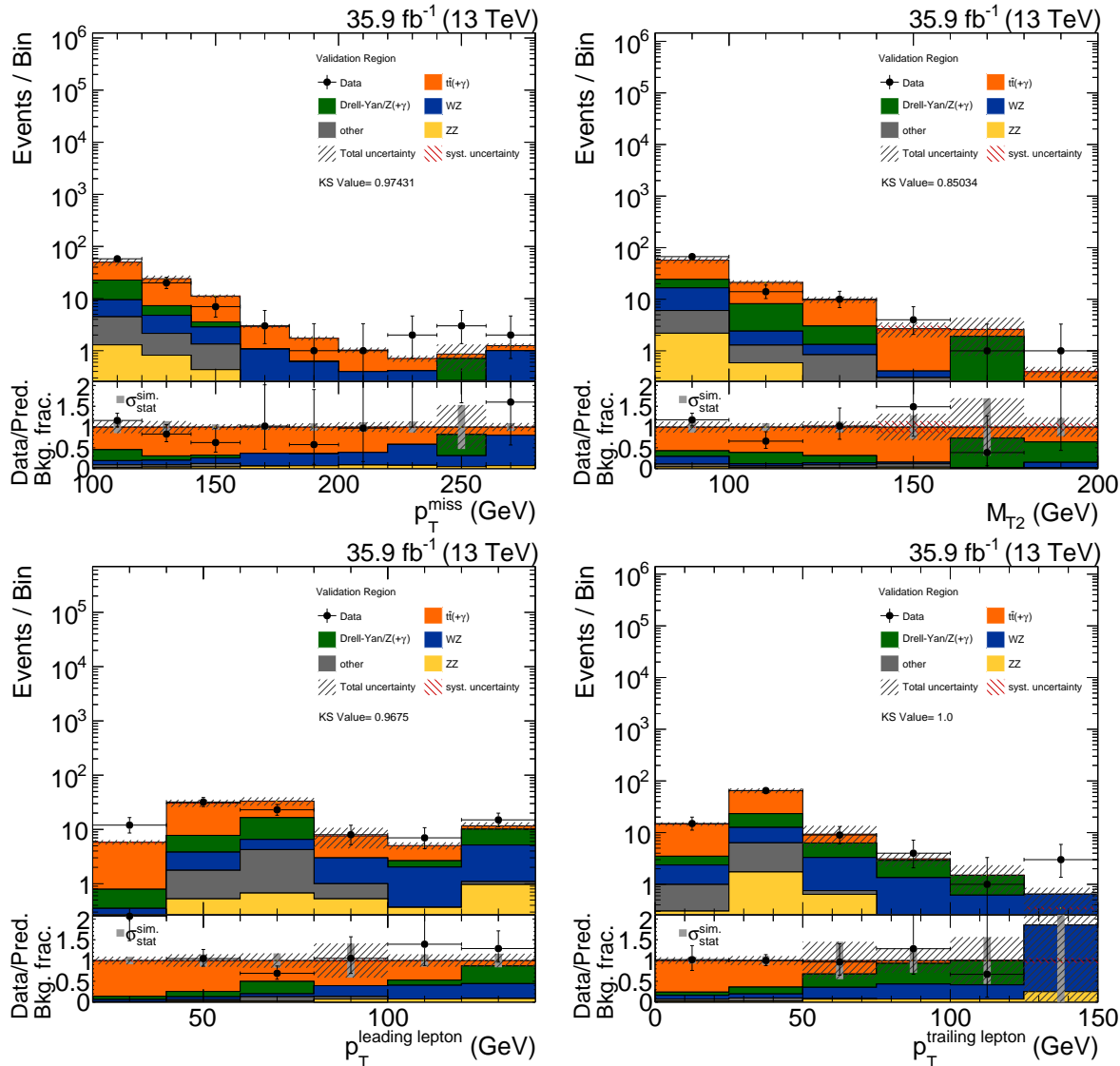


Figure 5.13.: Comparisons between data and rescaled simulation in the VR in the p_T^{miss} , M_{T2} , and lepton p_T distributions. Below each distribution, a ratio between data and prediction is shown. The uncertainty bands correspond to the systematic (red) and total uncertainty (gray). In addition, in the ratio plot the relative composition of the backgrounds is visualized. KS-values for the performed Kolmogorov-Smirnov test and the selection purity are also quoted.

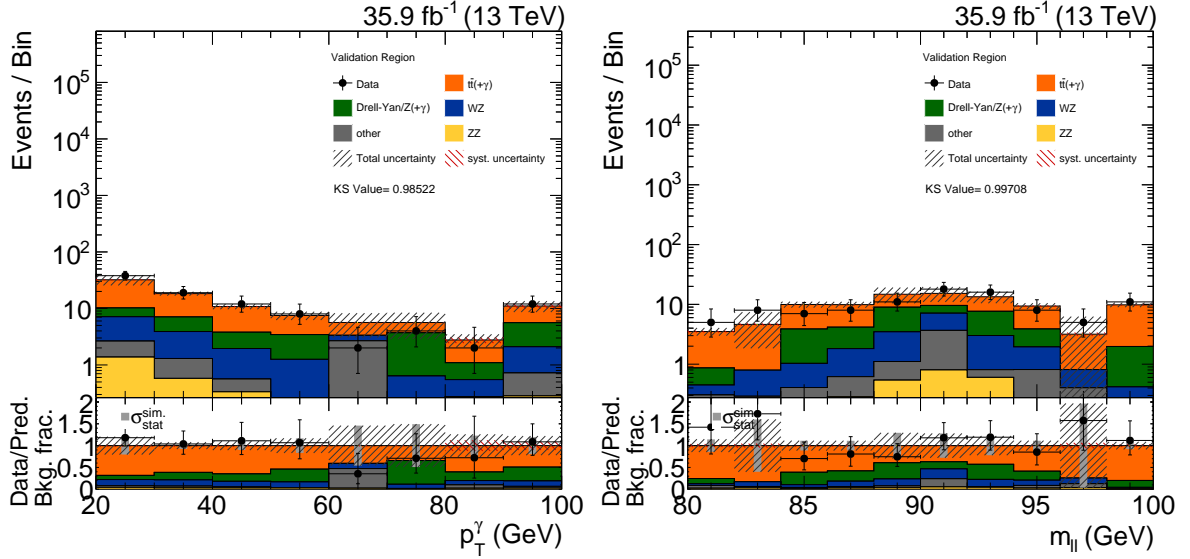


Figure 5.14.: Comparisons between data and rescaled simulation in the VR in the photon p_T and invariant dilepton mass distribution. Below each distribution, a ratio between data and prediction is shown. The uncertainty bands correspond to the systematic (red) and total uncertainty (gray). In addition, in the ratio plot the relative composition of the backgrounds is visualized. KS-values for the performed Kolmogorov-Smirnov test are also quoted.

5.2.7. Signal contamination

If SUSY was realized in nature, it would not only produce events in the SR, but also some events may appear in the CRs that are used to determine a proper background prediction. To account for this effect, the so-called signal contamination of the background CRs is not considered in the background estimation itself, but is translated into a reduction of the predicted signal yield in the SR. Hence, the signal contamination needs to be measured for each signal point of all samples individually in all CRs.

Therefore, the fraction of expected signal events relative to the total number of background events in each CR is measured. Exemplary, the signal contamination for the GMSB model in the DY/Z(γ) CR and WZ CR are shown in Figure 5.15, because they are the largest ones observed. This is due to the variety of decay topologies in this model. As can be seen, the contributions of signal events are mainly negligible, although the signal contamination reaches around 3% for very low bino and wino masses.

To account for those effects, these relative fractions are used to lower the signal expectation in each SR bin individually. If ρ is the fraction of signal events in the CR, in each SR bin the absolute signal event yield is reduced with the following formula

$$\#signal_{after} = \#signal_{before} - \rho \cdot \#background, \quad (5.9)$$

where $\#signal_{before}$ and $\#signal_{after}$ are the total number of signal events per bin before and after the correction, and $\#background$ is the number of predicted background events in this bin.

In total, the influence of signal contamination to the final result is rather negligible, because for most of the signal points the contributions to all CRs are very low. In cases where they exceed the level of a few percent, their influence will not matter in the final interpretation, since for those low SUSY mass signal points, the expectation for the signal yield in the SR is sufficiently high.

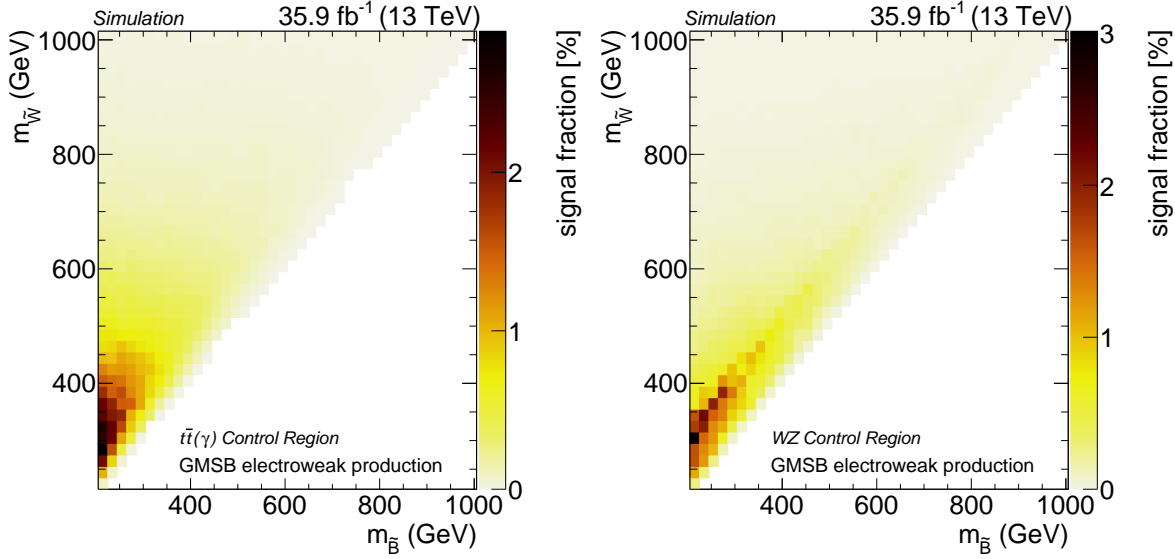


Figure 5.15.: Signal fraction compared to the total background event yield for different signal points of the TChiZG in the DY/Z(γ) CR (left) and the GMSB model in the WZ CR (right).

5.3. Study of systematic uncertainties

In addition to the statistical uncertainties arising from the background prediction method itself, various systematic effects and their impact on the final prediction need to be evaluated.

5.3.1. Background uncertainties

Systematic uncertainties arise from the data pileup distribution, which is used to rescale the simulated samples as explained in Section 4.2, the cross sections used to rescale the simulation, the measurement of the total integrated luminosity, the measurement of the jet energy scale (JES) and the jet energy resolution (JER), the measured trigger efficiencies as discussed in Section 4.6, corrections for a different photon and lepton reconstruction efficiency in simulation and data, the PDF sets used in the simulation process, and choice of the factorization scale and renormalization scale.

These measurements and underlying effects all contribute systematic uncertainties on the final background prediction yield. Cross section, trigger, and luminosity uncertainties are uncertainties in the normalization and cancel for the four main background contributions due to the integral method, but are relevant for the other minor contributions. For these a cross section uncertainty of 50% is assigned to the final yield to account for differences between cross section measurement and theoretical prediction, and to consider the circumstance, that only a special phase space region is investigated in the analysis.

The uncertainty on the luminosity measurement with 2.5% [138] and the uncertainty on the trigger efficiency, that is estimated to be 3% (see Section 4.6), propagate also directly to the final prediction for the other background contributions.

All other uncertainties are uncertainties in the shapes of the predicted spectra, and need to be determined in another way for all backgrounds. In order to estimate the impact of the JES and JER, the pileup reweighting, and the lepton and photon identification and reconstruction corrections, the background prediction is performed again with the underlying quantities shifted one standard deviation up and down. Hence, two additional predictions for each SR bin are obtained, and half of the difference between those, relative to the nominal prediction, is taken as the corresponding systematic uncertainty.

Table 5.1.: Systematic uncertainty ranges for all background predictions in the signal region.

	$t\bar{t}(\gamma)$	DY/Z(γ)	WZ	ZZ	Other
PDF	0.8 – 1.5%	2.6 – 3.3%	0.5 – 0.7%	2.2 – 2.4%	1.1 – 1.2%
Renorm. and fact. scale	3.3 – 7.1%	18.2 – 22.5%	4 – 6%	3.7 – 4.1%	2.1 – 9.3%
Jet energy scale	4.6 – 6.5%	4.4 – 5%	2.8 – 4.8%	1 – 1.9%	0 – 50.7%
Jet energy resolution	1.6 – 3.1%	0.7 – 16.1%	1 – 1.8%	0.2 – 1.4%	0 – 50.7%
Lepton ID and reco.	2.8 – 2.9%	2.2 – 3.4%	3.3%	1.8%	4.2%
Photon ID and reco.	0.7 – 0.8%	1.4 – 1.5%	1 – 1.1%	0.9%	0.7 – 1.9%
Luminosity	-	-	-	-	2.5%
Pileup	1.2 – 2%	1 – 5%	0.2 – 2.5%	1.5 – 1.7%	0.1 – 10%
Trigger efficiency	-	-	-	-	3%
Scale factor α_i	4.1%	0.9%	3.9%	5.7%	-
Cross section	-	-	-	-	50%

The uncertainty arising from the JES (JER) is observed to be around 1 – 6.5% (0.2 – 16.1%) for the four main backgrounds, while the uncertainty arising from the lepton (photon) identification and reconstruction ranges between 1.8 – 3.2 (0.7 – 1.5%). The uncertainty due to pileup reweighting varies between 0.2% and 5% for these four backgrounds. For the other backgrounds the uncertainties are higher, but the absolute effect is negligible compared to the other background contributions due to the low predicted event yields.

To estimate the effect on the choice of the renormalization scale μ_R and factorization scale μ_F , these two are varied in combinations of the factors 0.5, 1, and 2, and eight new background predictions are obtained. The half of the difference between the two outliers, relative to the nominal prediction, is chosen as the systematic uncertainty. It varies between 2.1 – 22.5% for all backgrounds over all bins.

To determine the systematic uncertainty arising from the used PDF sets, one hundred different PDF variations are studied, and for each the background prediction method is performed again, thus one hundred different predictions for the SR are obtained. From this distribution of predicted yields, the standard deviation and the mean can be calculated. The standard deviation with respect to the mean is considered as the systematic uncertainty, and varies between 0.5% and 3.3% for all backgrounds and bins.

The uncertainty arising from the choice of order regarding the four SFs determined in the CRs, is estimated by testing all $4! = 24$ possibilities, and calculating the largest deviation from the nominal SFs. This envelope is considered as a systematic uncertainty on the SFs on top of the statistical uncertainty. Both uncertainties are added quadratically, such that one final uncertainty for each SF is obtained.

Table 5.1 lists ranges for all final systematic uncertainties for all backgrounds individually. Besides uncertainties for some backgrounds, such as DY/Z(γ) and the other composed backgrounds, exceed the level of 10%, where statistical fluctuations based on changes of different quantities play an important role, all other systematic uncertainties are of the order of a few percent. This reflects the stability and robustness, that was observed in the scale factor determination itself.

5.3.2. Signal uncertainties

Signal uncertainties need to be studied in order to interpret the results statistically in each SUSY model. Most of the signal uncertainty determination methods behave the same as for the backgrounds, but some additional effects need to be considered. Some calculations change, since the detector response in the signal MC simulation was performed using the FASTSIM package. For the determination of the pileup uncertainty, a different method is applied. The pileup distribution is split into a low PU ($N_{vertices} < 20$) and a high PU ($N_{vertices} > 20$) region, and the

Table 5.2.: Ranges for all the systematic uncertainties for all signal models.

Uncertainty	Range [%]	
	Electroweak production	Strong production
Statistical	3.9 – 71	2.5 – 100
Luminosity	2.6	2.6
Pileup	< 0.1 – 93	< 0.1 – 193
Jet energy scale	< 0.1 – 32	< 0.1 – 62
Jet energy resolution	< 0.1 – 26	< 0.1 – 64
Trigger Efficiency	3	3
Lepton ID and reconstruction	< 1 – 5.6	0.8 – 2.1
Photon ID and reconstruction	1.4 – 1.5	1.4 – 1.5
FASTSIM uncert. in p_T^{miss}	< 0.1 – 97	< 0.1 – 294
ISR reweighting	2.6 – 3.9	5.9 – 11
Renorm. and fact. scale	< 0.1 – 1.6	< 0.1 – 11

difference in the total signal acceptance is determined. Half of this difference is treated as the systematic uncertainty.

Because the modeling of the p_T^{miss} distribution is very complicated, and in the FASTSIM package only a simplified detector response is parameterized, the difference between generated p_T^{miss} and reconstructed p_T^{miss} is investigated. Thus, the whole analysis is reperformed for the signal, where the reconstructed p_T^{miss} is replaced with the generated p_T^{miss} for each event, and the difference in the acceptance is examined. Half of the deviation is taken as the systematic uncertainty.

For the signal simulation, no PDF uncertainties are available. The initial state radiation dependent reweightings mentioned in Section 4.2 introduce systematic effects on the signal yield expectation. Therefore, the same method as mentioned above for the identification and reconstruction uncertainties on the background prediction is performed.

Ranges for all signal uncertainties, including the statistical one, are given in Table 5.2 altogether for all signal models considered in the analysis and are given separately for electroweak and strong production scenarios.

All other systematic effects, except for the luminosity uncertainty and the uncertainty arising from the trigger efficiency measurement are correlated with the statistical uncertainty. Hence, large ranges are observable due to the limited statistics that is available for each signal point. This is due to time and resource saving reasons, since a large number of different signal points is being generated. In addition, the low available number of signal events becomes much lower, as only leptonic decay branches of the Z boson are considered and its branching fraction ($\mathcal{BR}(Z \rightarrow \ell^+ \ell^-) \approx 3.36\%$ [14]) is very low. Nevertheless, in most of the relevant signal points the uncertainties do not exceed the level of a few percent.

Results and interpretation

Contents

6.1. Results	61
6.2. Statistical interpretation	63

Now that all backgrounds are well estimated, the background prediction is reliable in the validation region, and all uncertainties are determined, the background prediction methods can be applied to the SR, $p_T^{\text{miss}} > 150 \text{ GeV}$ and $M_{\text{T}2} > 100 \text{ GeV}$, and predicted and observed event counts can be compared. An excess of events or other significant deviations from the prediction could be indicators for BSM physics.

6.1. Results

Signal region binning

In order to perform the counting experiment, a distinct binning in one or multiple variables needs to be applied to the SR. This binning can be optimized considering different criteria, e.g., observation and exclusion power. Since the most sensitive variables are p_T^{miss} and $M_{\text{T}2}$, different one dimensional and two dimensional binnings are possible. Because the total predicted event count in the SR is approximately 13 events, special care has to be taken regarding this low data yield. Albeit many sensitive bins with lower SM prediction and high signal expectation would push expected exclusion limits, this would make reinterpretations and observations difficult due to the high statistical uncertainties of the measured data. Considering that the p_T^{miss} and $M_{\text{T}2}$ distributions are exponentially decreasing for the predicted backgrounds, the maximum number of bins is limited. Therefore, a binning consisting of two bins is chosen. It consists of two bins in the p_T^{miss} distribution, as already introduced in Section 5.1.2. The first bin starts at 150 GeV and ends at 200 GeV, while the second one gathers all events with $p_T^{\text{miss}} > 200 \text{ GeV}$ in the SR. This choice yields good exclusion power while containing a sufficient number of events in each bin, so that the reinterpretation is not restricted by statistical uncertainties. For the same reasons, higher dimensional binnings are discarded, too. The p_T^{miss} distribution is preferred over the $M_{\text{T}2}$ distribution, because it is more model independent given the many decay possibilities in full theoretical models. In the calculation of $M_{\text{T}2}$, both bosons are assumed to be generated in an NLSP decay together with a gravitino, but the relevant final state particles (Z and γ) can be produced in several decay branches of different particles considering consistent models. In contrast, p_T^{miss} is a general measure of the energy carried by the gravitinos, thus being more independent and universal.

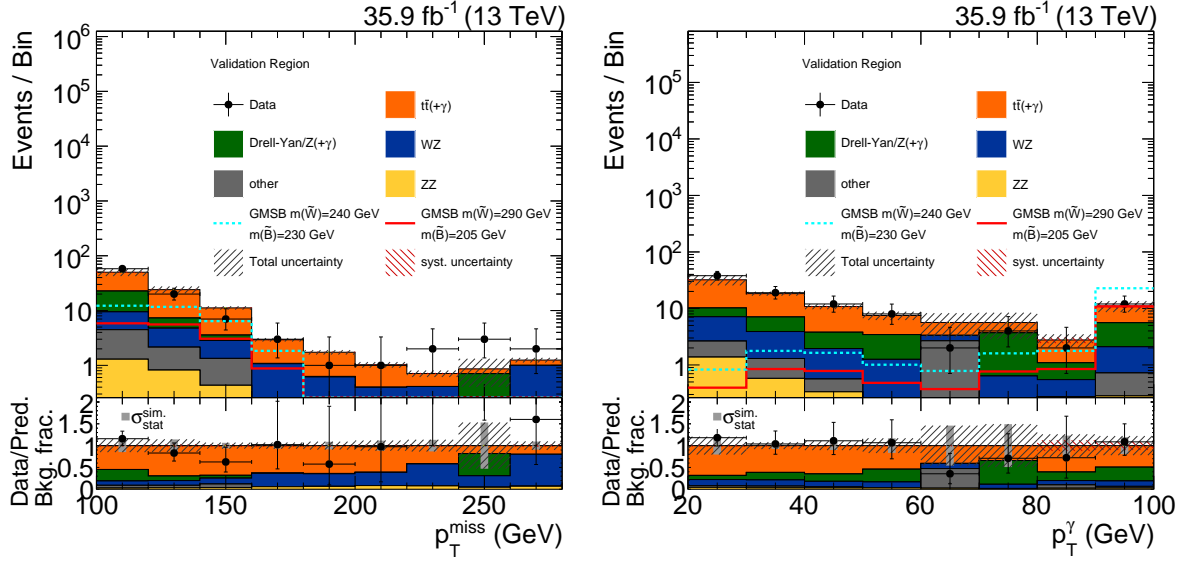


Figure 6.1.: The p_T^{miss} (left) and transverse momentum distribution of the photon in the VR (right). Signal benchmark points are also added to show the possible sensitivity in the high p_T^γ regime.

Possible influence of signal to the validation region

The SR and the VR are very close to each other in phase space due to the chosen sideband structure of the VR. Thus, some signal events, especially for low SUSY masses, are expected to populate also the VR. The distribution most sensitive to this effect is the p_T^γ distribution of the selected photon, as shown in Figure 6.1, where the p_T^γ and p_T^{miss} distributions are compared. For $p_T^\gamma > 80 \text{ GeV}$, a considerable amount of signal events is measurable in the VR, because in the considered SUSY processes the photons produced in the NLSP decay gain high momenta due to the high NLSP masses. Since the predicted background and observed data are already compared in the VR, and no background prediction is performed here, there is no need to account for this effect like in the other CR in terms of signal contamination.

Hence, the subtraction of this region from the VR, and the addition to the SR as a third search bin would increase the total sensitivity. The number of expected signal events in the two SR bins is already high enough for the relevant signal points to be excluded with a high significance. Thus, this strategy does not show any improvement in the overall sensitivity, that is large enough to justify the deterioration in the simplicity of the analysis.

Signal acceptances

The acceptance of the event selection is defined as the fraction of events being selected in the SR to all events in a distinct SUSY signal scenario being produced before passing the reconstruction, identification, and selection. Because several effects are considered in the definition, such as detector acceptance and trigger efficiencies, it is often referred to as acceptance times efficiency. In Table 6.1, exemplary the events yields for three different signal points after several analysis steps are given. In addition, the relevance of each SR bin with regard to the final sensitivity is indicated by comparing the expected number of signal events in each bin.

For all three considered signal scenarios, the acceptance after the preselection is already of the order of $\mathcal{O}(1\%)$. Due to the low branching fraction of the Z boson decaying to either an electron or a muon pair (each approximately 3.36%), low acceptances are expected considering the inefficiencies of the reconstruction, the trigger, and the particle identification. In addition, the probability for the NLSP to decay to a Z boson is only 50% in the SMS, and even lower for

the GMSB model, see Section 2.3.2. Therefore, the total acceptance is further decreased. The SR selection requirements, namely the p_T^{miss} and M_{T2} requirements, reduce the signal yield only insignificantly while decreasing the background contributions. Signal acceptances for all signal points are given in Section C in the appendix. Comparing the acceptances for all points, they are all of the same order, slightly depending on the sparticle masses.

Table 6.1.: Number of events for three signal points after several selection steps. The signal points correspond to the TChizG model with $m(\text{NLSP}) = 600 \text{ GeV}$, the GMSB model with $m(\widetilde{W}) = 415 \text{ GeV}$ $m(\widetilde{B}) = 355 \text{ GeV}$, and the T5bbbbZG model with $m(\tilde{g}) = 1500 \text{ GeV}$ $m(\text{NLSP}) = 1400 \text{ GeV}$.

Selection	Number of Events (Rel. fraction)					
	TChizG		GMSB		T5bbbbZG	
Before Selection	1063	(100%)	5285	(100%)	509	(100%)
Preselection	11.3	(1.06%)	21.5	(0.40%)	5.1	(1.00%)
$M_{\text{T2}} > 100 \text{ GeV}$	10.8	(1.02%)	18.5	(0.35%)	5.0	(0.99%)
$p_T^{\text{miss}} > 150 \text{ GeV}$	9.8	(0.92%)	14.2	(0.27%)	4.9	(0.96%)
$150 \text{ GeV} < p_T^{\text{miss}} < 200 \text{ GeV}$	0.7	(0.06%)	3.2	(0.06%)	0.1	(0.02%)
$p_T^{\text{miss}} > 200 \text{ GeV}$	9.1	(0.86%)	11.0	(0.21%)	4.8	(0.94%)

Event yields

The final background prediction together with the observed event yield is shown in Figure 6.2. The total background uncertainties are obtained by adding the individual uncertainties quadratically. The statistical uncertainties in the measurement are calculated using 68% confidence intervals of the Poisson distribution with the mean set to the observed yield. To show the effect of a possible signal in the counting experiment, contributions of two example signal points are drawn for comparison.

The number of background and observed events together with their total uncertainties are given also in Table 6.2. The measured data yields are in good agreement with the predicted background events, thus no evidence for BSM physics is found. The measured excess corresponds to a significance of 1.3 standard deviations calculated with the discovery significance based on a profile-likelihood ratio test and Asimov approximation [139]

$$Z_A = \left[2 \left(n \ln \left[\frac{n(b + \sigma_b^2)}{b^2 + n\sigma_b^2} \right] - \frac{b^2}{\sigma_b^2} \ln \left[1 + \frac{\sigma_b^2(n - b)}{b(b + \sigma_b^2)} \right] \right) \right]^{1/2}, \quad (6.1)$$

where n is the observed yield, b the predicted background, and σ_b the total uncertainty on the prediction, combining the statistical and systematic uncertainty on the background prediction. Albeit other approaches to calculate the observed significance, like $\frac{n-b}{\sqrt{b}}$ and $\frac{n-b}{\sqrt{b+\sigma_b^2}}$, overestimate the significance for small b , the Asimov significance yields a more confident estimate of the true significance of the observation [140].

6.2. Statistical interpretation

No evidence for BSM physics is found, but the results can be interpreted in various SUSY models in terms of the exclusion of model parameter space.

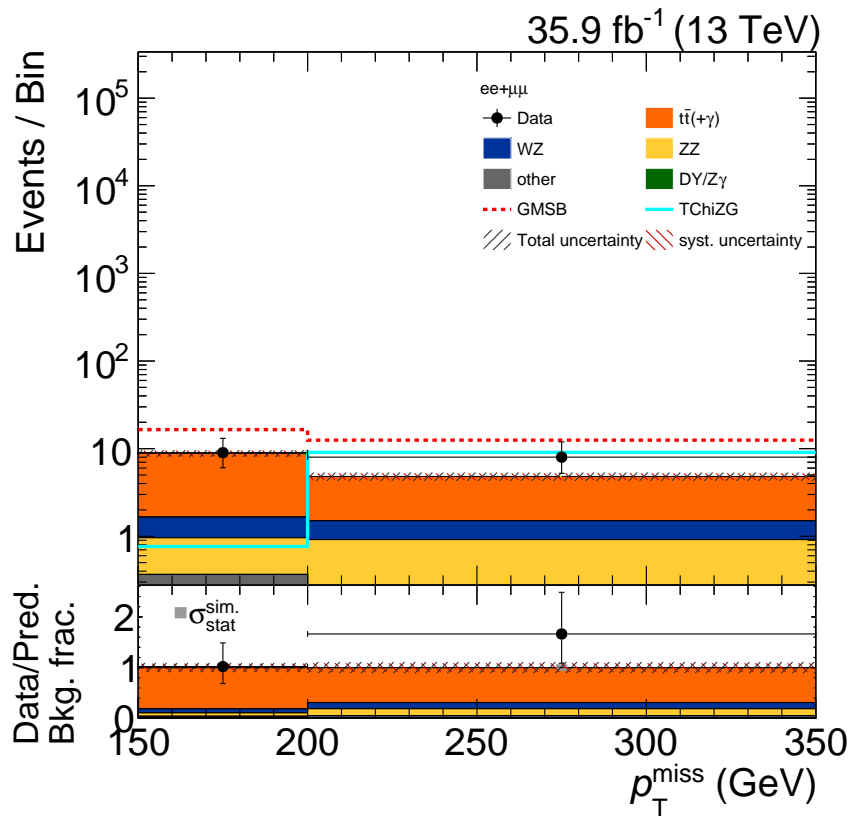


Figure 6.2.: Comparison between final prediction and observation with statistical and systematic uncertainties in the signal region. Two signal expectations for the TChiZG model with $m(\text{NLSP}) = 600 \text{ GeV}$ and the GMSB model with $m(\tilde{W}) = 290 \text{ GeV}$ and $m(\tilde{B}) = 205 \text{ GeV}$ are also shown.

Table 6.2.: Observed yields and final predicted background yields with the statistical and systematic uncertainties for each bin and background.

p_T^{miss}	150 – 200 GeV			200 GeV – ∞		
	yield	σ_{stat}	σ_{syst}	yield	σ_{stat}	σ_{syst}
$t\bar{t}(\gamma)$	7.16	0.32	0.60	3.31	0.23	0.37
DY/Z(γ)	0.15	0.06	0.04	0.04	0.02	0.01
WZ	0.69	0.08	0.06	0.59	0.08	0.05
ZZ	0.60	0.02	0.05	0.67	0.02	0.06
Other	0.22	0.22	0.19	0.21	0.21	0.11
Total	8.82	0.40	0.63	4.82	0.32	0.40
Data	9			8		

6.2.1. Limit calculation

Upper cross section limits are calculated for signal points in the parameter space of simplified models with both electroweak and strong production, and for a consistent GMSB model, as introduced in Section 2.3.2. All limits are calculated using the modified frequentist CL_s approach [141–143] with likelihood test statistics and asymptotic formulae [144, 145] at a confidence level (CL) of 95%. The compatibility of the background only (b) and signal plus background ($s + b$) hypotheses with the results is tested. Therefore, the signal strength modifier μ is introduced, in order to express both hypotheses in a uniform way $\mu s + b$, where $\mu = 0$ yields the background only hypotheses, and $\mu > 0$ corresponds to a $s + b$ hypothesis.

To account for systematic uncertainties, for each signal or background uncertainty a nuisance parameter θ is introduced, and signal and background yields are rewritten as functions of θ : $s(\theta)$ and $b(\theta)$. Different probability density functions (pdf) $p(\tilde{\theta}|\theta)$ are also implemented in the likelihood, to reflect the degree of belief in the true value of the nuisance parameter θ , where $\tilde{\theta}$ is the default value of the nuisance parameter. Different pdfs are used to describe the uncertainties, such as the log-normal or log-uniform distributions. The total likelihood function $\mathcal{L}(data|\mu, \theta)$ reads

$$\mathcal{L}(data|\mu, \theta) = Poisson(data|\mu \cdot (\theta + b(\theta)) \cdot p(\tilde{\theta}|\theta)). \quad (6.2)$$

Here, $data$ represents the actual experimental observation, and $Poisson(data|\mu \cdot (\theta + b(\theta)))$ stands for the probability to observe n_i events in bin i :

$$Poisson(data|\mu s + b) = \prod_i \frac{(\mu s_i + b_i)^{n_i}}{n_i!} e^{-\mu s_i - b_i}. \quad (6.3)$$

A test statistic \tilde{q}_μ is introduced as a likelihood ratio, because according to the Neyman-Pearson Lemma [146], this is the discriminator suited best for the testing of two alternative statistical hypotheses while minimizing the rate of wrongly rejected true hypotheses and accepted false hypotheses:

$$\tilde{q}_\mu = -2 \ln \frac{\mathcal{L}(data|\mu, \hat{\theta}_\mu)}{\mathcal{L}(data|\hat{\mu}, \hat{\theta})}, \text{ with } 0 \leq \hat{\mu} \leq \mu. \quad (6.4)$$

Here, $\hat{\theta}_\mu$ refers to the conditional maximum likelihood estimators of θ , given the signal strength μ and the data observation. The parameters $\hat{\theta}$ and $\hat{\mu}$ correspond to the global maximum of the likelihood. The constraints on $\hat{\mu}$ ensure, that only positive signal rates are considered, and a one sided confidence interval is guaranteed.

The probability to obtain values of $\hat{\theta}_\mu$ larger than observed in data ($\hat{\theta}_\mu^{obs}$) is given by CL_b for the background only hypothesis and CL_{s+b} for the signal plus background hypothesis. Now, the ratio CL_s can be calculated by

$$CL_s = \frac{CL_{s+b}}{CL_b}. \quad (6.5)$$

The $(1 - \alpha) = 95\%$ CL upper limit is found by varying μ until $CL_s = \alpha = 0.05$ is reached.

The limits on μ can be translated into signal cross section upper limits by multiplying it with the cross section that was used to determine the expected signal yield.

The calculation is performed using the Higgs Combine tool [143], while all systematic uncertainties are treated as fully correlated over all bins and background, except for the statistical uncertainties. Additional expected upper limits are calculated using pseudo-data, that are useful to show the expected sensitivity of the analysis, since statistical fluctuations are not considered.

6.2.2. Exclusion limits

Three different SUSY models are used to interpret the results of the counting experiment discussed above individually for each masspoint. If the given theoretical cross section exceeds the calculated limit, the points are considered as excluded. In cases of two dimensional parameter scans, exclusion contours can be determined.

Limits on electroweak production of charginos and neutralinos

Two different models are used to interpret the results for EWK SUSY production. For the TChiZG SMS, expected (dashed line) and observed (solid line) upper limits are shown in Figure 6.3 (top) as a function of the NLSP mass parameter. The theoretical cross section together with the uncertainty band is plotted as the blue curve. The error band of the expected limit reflects all uncertainties of the analysis.

This analysis is capable of excluding NLSP masses below 600 GeV in this scenario. Due to the excess of data in the second SR bin, which is the most sensitive one for all signal points of this parameter scan, the observed limit is approximately one standard deviation weaker than the expected limit of 675 GeV.

Upper cross section limits for the two dimensional GMSB model are shown in Figure 6.3 (bottom) together with the expected limit contour (red) and the observed limit contour (black). The uncertainty band of the expected limit represents all analysis specific uncertainties, while the uncertainty band of the observed limit reflects theoretical cross section uncertainties. The limits are shown in the wino-bino mass plane, where the wino mass corresponds to the $\tilde{\chi}_1^\pm$ and $\tilde{\chi}_2^0$ mass, and the bino mass corresponds to the NLSP $\tilde{\chi}_1^0$ mass, as discussed in Section 2.3.2. The analysis has the highest sensitivity in cases where the bino and wino mass differ by around 90 GeV, so that Z boson production in the decays of the wino is enhanced, as can be seen by the off-diagonal structure in the cross section limit plane. The sensitivity weakens for lower and higher wino masses, since the available energy is split between all decay products. For degenerate bino and wino masses, the sensitivity increases again, because nearly all energy is transferred into the final decay products, the gravitinos and the selected bosons. Due to the cross section decrease for larger wino masses, the sensitivity loses there. In total, the analysis excludes bino and wino masses in a range up to 400 – 560 GeV depending on the wino and bino mass.

The exclusion contours show the same behavior as for the one-dimensional exclusion discussed above due to the overfluctuation in data in the second SR bin. Therefore, the observed limit is weaker than the expected limit.

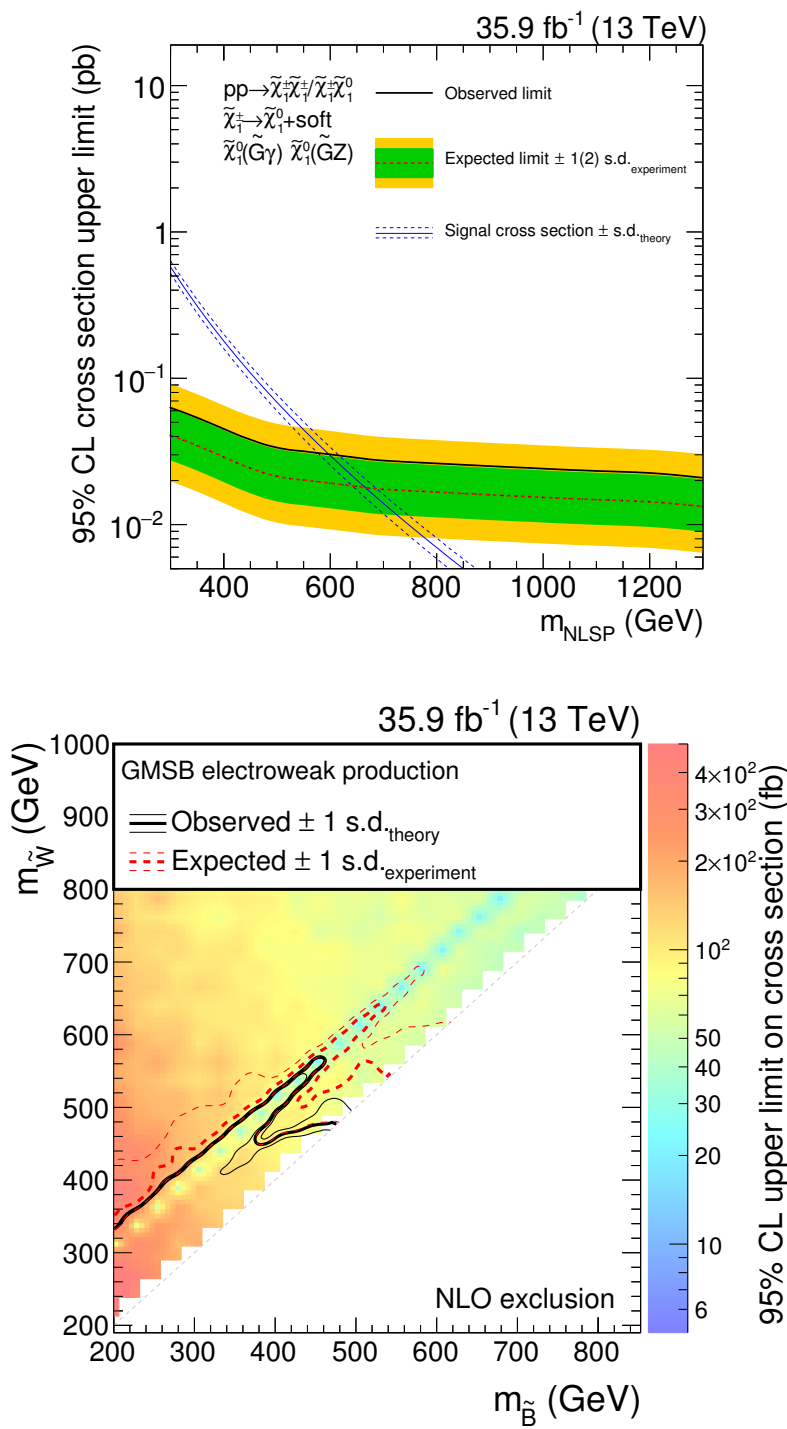


Figure 6.3.: Expected and observed upper limits for the TChiZG electroweak SMS (top) and the full GMSB model (bottom).

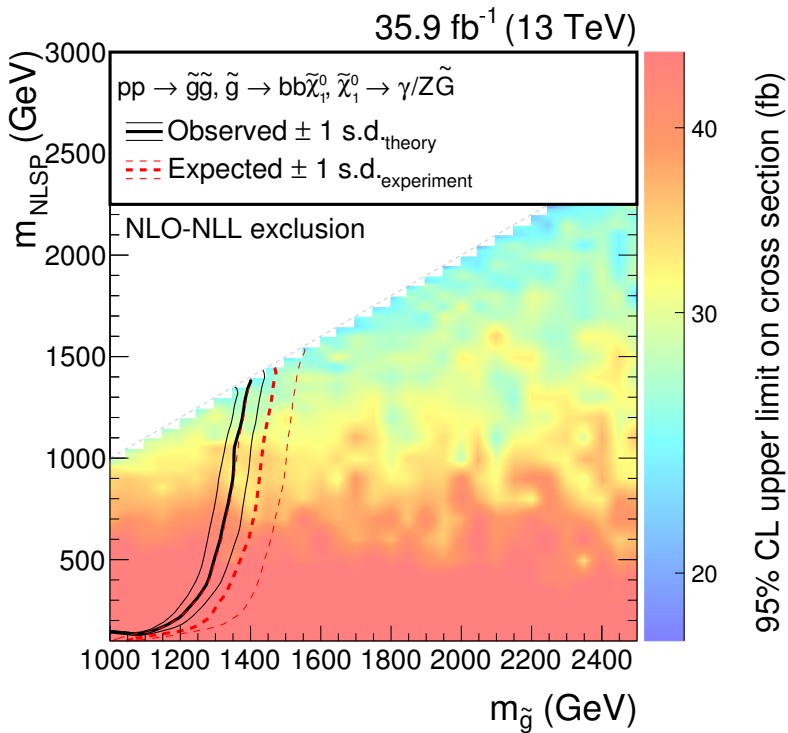


Figure 6.4.: Expected and observed upper limits for the T5bbbbZG SMS with strong production.

Limits on strong production of gluinos

In addition to the limits on EWK SUSY production, the results are interpreted in an SMS with gluino pair production. The cross section upper limits are shown in Figure 6.4 in the gluino-NLSP mass plane.

The analysis can exclude gluino masses up to 1.4 TeV, depending on the mass of the NLSP, and thus the mass splitting between them. For NLSP masses lower than 150 GeV, the sensitivity drops because of the applied M_{T2} threshold of 100 GeV. Because M_{T2} yields an estimate of the NLSP mass, but the M_{T2} distribution shows an endpoint at the NLSP mass and is broad due to the difficulty in the interpretation of $p_{\text{T}}^{\text{miss}}$ in the calculation, signal points with NLSP masses above 100 GeV are also affected by this requirement. With increased $\tilde{\chi}_1^0$ masses the sensitivity rises, since the final state products carry more energy. Again, the same effect between expected and observed limit contour is observable as for the electroweak models.

In addition, comparing the cross section limits over the parameter space, statistical fluctuations are present because of the limited number of events being simulated in the SMS. This reflects also the large fluctuation which was observed in the variation range of the statistical and systematic uncertainties. Moreover, the small differences in the cross section limit indicate that the sensitivity is almost similar for varying NLSP masses, and the exclusion contour is mainly determined by the production cross section and the small branching fraction of the Z boson to leptons.

Summary & Conclusion

A search for supersymmetry (SUSY) in final states with missing transverse momentum p_T^{miss} , a Z boson decaying to charged leptons ($Z \rightarrow ee/\mu\mu$), and photons based on a data set of proton-proton collisions with a center-of-mass energy of 13 TeV recorded with CMS in 2016 has been presented. The data set corresponds to an integrated luminosity of 35.9 fb^{-1} , and the relevant events are selected using same flavor dilepton triggers.

Events with photons, Z bosons, and p_T^{miss} are expected in gauge-mediated supersymmetry breaking (GMSB) scenarios, where the next-to-lightest supersymmetric particle (NLSP) is bino- or wino-like, and the NLSP decays to these standard model (SM) bosons and the lightest supersymmetric particle (LSP), which is the gravitino \tilde{G} . The gravitino is predicted to be stable in R-parity conserving SUSY scenarios and leaves the detector undetected, thus giving rise to a significant amount of p_T^{miss} in the event.

The search was developed such, that it is complementary to other CMS GMSB SUSY searches targeting different scenarios including photons. Therefore, this is the first CMS SUSY analysis investigating explicitly $Z(\rightarrow \ell\ell) + \gamma$ events. In addition, the analysis is designed to be sensitive to different production channels of gauginos, including strong and electroweak production channels. By restricting the search to events including three final state particles and p_T^{miss} , the requirements on the final states momenta can be low. The usage of the stransverse mass M_{T2} reconstructed from the Z boson candidate, the photon, and the missing transverse momentum, enables good discrimination between background and SUSY signals by estimating the NLSP mass.

The main background contributions for the search are $t\bar{t}(\gamma)$, DY/Z(γ), WZ, and ZZ production, while $t\bar{t}(\gamma)$ is by far the most important background, making up 70 – 80% of the total SM background in the signal region. Each of those backgrounds is estimated with an approach based on Monte-Carlo simulation, where each background is normalized to the observation in a dedicated control region. Data and prediction are observed to agree in each control region, and further studies such as χ^2 -fits are performed to investigate the modeling of different observables within the simulation.

The final background prediction is validated in a validation region, which is constructed as a kinematic sideband region to the signal region, by requiring the events to fail one of the two additional signal region requirements. The agreement between data and prediction in the validation region is also good, indicating that the background estimations is stable.

In the signal region, a counting experiment is performed comparing predicted and observed

event yields in each of the bins of the p_T^{miss} distribution. No significant deviation is observed.

Upper cross section and exclusion limits are calculated at 95% confidence level for three different signal models. The results are interpreted within an electroweak model based on the General Gauge Mediation framework, excluding bino and wino masses up to 400 – 560 GeV. Additional simplified models are used for interpretation, excluding NLSP masses up to 600 GeV in case of electroweak gaugino production. In cases of gluino pair production, gluino masses lower than 1.4 TeV are excluded for low mass differences between the gluino and the NLSP, decreasing for larger mass differences.

The results presented throughout this thesis are documented in [9]. The exclusion limits are comparative to different CMS SUSY searches [6] in the low bino and wino mass regions of the GMSB model, but are not as sensitive as other analyses for the simplified models discussed above due to the low $Z \rightarrow \ell\ell$ branching fraction. Since the analysis investigates a new final state with respect to all other CMS GMSB SUSY searches [5–7], it can be useful for a future statistical combination of analyses, which is under development [147] at the time of writing. With the full Run II data recorded at CMS in the years 2015–2018, a reperformance of this search on the much larger data set would be interesting, as the larger data set enables possibilities to optimize the background prediction, especially the search region definitions, and thus compensates the small branching fraction of the leptonic Z boson decays.

Bibliography

- [1] CMS Collaboration, “Observation of a new boson at a mass of 125 GeV with the CMS experiment at the LHC”, *Phys. Lett. B* **716** (2012) doi:10.1016/j.physletb.2012.08.021, arXiv:1207.7235.
- [2] ATLAS Collaboration, “Observation of a new particle in the search for the Standard Model Higgs boson with the ATLAS detector at the LHC”, *Phys. Lett. B* **716** (2012) 1–29, doi:10.1016/j.physletb.2012.08.020, arXiv:1207.7214.
- [3] ATLAS, CMS Collaboration, “Combined Measurement of the Higgs Boson Mass in pp Collisions at $\sqrt{s} = 7$ and 8 TeV with the ATLAS and CMS Experiments”, *Phys. Rev. Lett.* **114** (2015) 191803, doi:10.1103/PhysRevLett.114.191803, arXiv:1503.07589.
- [4] E. Noether, “Invariant Variation Problems”, *Gott. Nachr.* **1918** (1918) doi:10.1080/00411457108231446, arXiv:physics/0503066. [Transp. Theory Statist. Phys.1,186(1971)].
- [5] CMS Collaboration, “Search for supersymmetry in events with at least one photon, missing transverse momentum, and large transverse event activity in proton-proton collisions at $\sqrt{s} = 13$ TeV”, *JHEP* **12** (2017) 142, doi:10.1007/JHEP12(2017)142, arXiv:1707.06193.
- [6] CMS Collaboration, “Search for gauge-mediated supersymmetry in events with at least one photon and missing transverse momentum in pp collisions at $\sqrt{s} = 13$ TeV”, *Phys. Lett. B* **780** (2018) doi:10.1016/j.physletb.2018.02.045, arXiv:1711.08008.
- [7] CMS Collaboration, “Search for supersymmetry in events with a photon, jets, and missing transverse momentum in proton-proton collisions at 13 TeV”, Technical Report CMS-PAS-SUS-18-002, 2018.
- [8] CMS Collaboration, “Search for supersymmetry using events with a photon, a lepton, and missing transverse momentum in pp collisions at $\sqrt{s} = 13$ TeV”, Technical Report CMS-PAS-SUS-17-012, 2018.
- [9] S. Wuchterl, C. Autermann, and L. Feld, “Search for supersymmetry in events with photons and a leptonically decaying Z boson at $\sqrt{s} = 13$ TeV”, *CMS Analysis Note* **18-189** (2018).

- [10] F. Pisano and N. O. Reis, “Natural units, numbers and numerical clusters”, *ArXiv High Energy Physics - Phenomenology* (2001) [arXiv:hep-ph/0112097](https://arxiv.org/abs/hep-ph/0112097).
- [11] A. Pich, “The Standard model of electroweak interactions”, in *The Standard model of electroweak interactions*. 2008. [arXiv:0705.4264](https://arxiv.org/abs/0705.4264).
- [12] A. Einstein, “The Foundation of the General Theory of Relativity”, *Annalen Phys.* **49** (1916) doi:10.1002/andp.200590044, 10.1002/andp.19163540702. [65(1916)].
- [13] C. Burgard, “Standard model of physics”. Modified. Accessed: 2018-09-25. <http://www.texexample.net/tikz/examples/model-physics/>.
- [14] Particle Data Group Collaboration, “Review of Particle Physics”, *Chin. Phys. C* **40** (2016) 100001, doi:10.1088/1674-1137/40/10/100001.
- [15] K. G. Wilson, “Confinement of quarks”, *Phys. Rev. D* **10** (1974) doi:10.1103/PhysRevD.10.2445.
- [16] LHCb Collaboration, “Evidence for exotic hadron contributions to $\Lambda_b^0 \rightarrow j/\psi p\pi^-$ decays”, *Phys. Rev. Lett.* **117** (2016) 082003, doi:10.1103/PhysRevLett.117.082003.
- [17] S. Weinberg, “Effects of a neutral intermediate boson in semileptonic processes”, *Phys. Rev. D* **5** (1972) doi:10.1103/PhysRevD.5.1412.
- [18] S. Weinberg, “A model of leptons”, *Phys. Rev. Lett.* **19** (1967) doi:10.1103/PhysRevLett.19.1264.
- [19] A. Salam and J. Ward, “Electromagnetic and weak interactions”, *Physics Letters* **13** (1964) doi:[https://doi.org/10.1016/0031-9163\(64\)90711-5](https://doi.org/10.1016/0031-9163(64)90711-5).
- [20] S. L. Glashow, “Partial-symmetries of weak interactions”, *Nuclear Physics* **22** (1961) doi:[https://doi.org/10.1016/0029-5582\(61\)90469-2](https://doi.org/10.1016/0029-5582(61)90469-2).
- [21] C. S. Wu et al., “Experimental test of parity conservation in beta decay”, *Phys. Rev.* **105** (1957) doi:10.1103/PhysRev.105.1413.
- [22] M. Goldhaber, L. Grodzins, and A. W. Sunyar, “Helicity of neutrinos”, *Phys. Rev.* **109** (1958) doi:10.1103/PhysRev.109.1015.
- [23] P. W. Higgs, “Broken symmetries and the masses of gauge bosons”, *Phys. Rev. Lett.* **13** (1964) doi:10.1103/PhysRevLett.13.508.
- [24] F. Englert and R. Brout, “Broken symmetry and the mass of gauge vector mesons”, *Phys. Rev. Lett.* **13** (1964) doi:10.1103/PhysRevLett.13.321.
- [25] G. S. Guralnik, C. R. Hagen, and T. W. B. Kibble, “Global conservation laws and massless particles”, *Phys. Rev. Lett.* **13** (1964) doi:10.1103/PhysRevLett.13.585.
- [26] CMS Collaboration, “Precise determination of the mass of the Higgs boson and tests of compatibility of its couplings with the standard model predictions using proton collisions at 7 and 8 TeV”, *Eur. Phys. J. C* **75** (2015) 212, doi:10.1140/epjc/s10052-015-3351-7, [arXiv:1412.8662](https://arxiv.org/abs/1412.8662).
- [27] CMS Collaboration, “Observation of $t\bar{t}$ production”, *Phys. Rev. Lett.* **120** (2018) 231801, doi:10.1103/PhysRevLett.120.231801.
- [28] CMS Collaboration, “Observation of the Higgs boson decay to a pair of τ leptons with the CMS detector”, *Phys. Lett. B* **779** (2018) doi:10.1016/j.physletb.2018.02.004, [arXiv:1708.00373](https://arxiv.org/abs/1708.00373).

- [29] CMS Collaboration, “Observation of Higgs boson decay to bottom quarks”, *Phys. Rev. Lett.* (2018) [arXiv:1808.08242](#).
- [30] Planck Collaboration, “Planck 2015 results. XIII. Cosmological parameters”, *Astron. Astrophys.* **594** (2016) [doi:10.1051/0004-6361/201525830](#), [arXiv:1502.01589](#).
- [31] R. Massey, T. Kitching, and J. Richard, “The dark matter of gravitational lensing”, *Rept. Prog. Phys.* **73** (2010) 086901, [doi:10.1088/0034-4885/73/8/086901](#), [arXiv:1001.1739](#).
- [32] M. Persic, P. Salucci, and F. Stel, “The Universal rotation curve of spiral galaxies: 1. The Dark matter connection”, *Mon. Not. Roy. Astron. Soc.* **281** (1996) 27, [doi:10.1093/mnras/281.1.27](#), [10.1093/mnras/278.1.27](#), [arXiv:astro-ph/9506004](#).
- [33] L. Canetti, M. Drewes, and M. Shaposhnikov, “Matter and Antimatter in the Universe”, *New J. Phys.* **14** (2012) 095012, [doi:10.1088/1367-2630/14/9/095012](#), [arXiv:1204.4186](#).
- [34] G. R. Farrar and M. E. Shaposhnikov, “Baryon asymmetry of the universe in the minimal Standard Model”, *Phys. Rev. Lett.* **70** (1993) [doi:10.1103/PhysRevLett.71.210.2](#), [10.1103/PhysRevLett.70.2833](#), [arXiv:hep-ph/9305274](#). [Erratum: *Phys. Rev. Lett.* 71, 210(1993)].
- [35] A. D. Sakharov, “Violation of CP Invariance, C asymmetry, and baryon asymmetry of the universe”, *Pisma Zh. Eksp. Teor. Fiz.* **5** (1967) [doi:10.1070/PU1991v034n05ABEH002497](#). [*Usp. Fiz. Nauk* 161,no.5,61(1991)].
- [36] M. C. Gonzalez-Garcia and Y. Nir, “Neutrino masses and mixing: Evidence and implications”, *Rev. Mod. Phys.* **75** (2003) [doi:10.1103/RevModPhys.75.345](#), [arXiv:hep-ph/0202058](#).
- [37] S. P. Martin, “A Supersymmetry primer”, [doi:10.1142/9789812839657_0001](#), [10.1142/9789814307505_0001](#), [arXiv:hep-ph/9709356](#). [*Adv. Ser. Direct. High Energy Phys.* 18,1(1998)].
- [38] J. Wess and B. Zumino, “Supergauge Transformations in Four-Dimensions”, *Nucl. Phys. B* **70** (1974) [doi:10.1016/0550-3213\(74\)90355-1](#). [24(1974)].
- [39] S. Coleman and J. Mandula, “All possible symmetries of the s matrix”, *Phys. Rev.* **159** (1967) [doi:10.1103/PhysRev.159.1251](#).
- [40] R. Haag, J. T. Lopuszański, and M. Sohnius, “All possible generators of supersymmetries of the s-matrix”, *Nuclear Physics B* **88** (1975) [doi:https://doi.org/10.1016/0550-3213\(75\)90279-5](#).
- [41] S. P. de Alwis, “On Anomaly Mediated SUSY Breaking”, *Phys. Rev. D* **77** (2008) 105020, [doi:10.1103/PhysRevD.77.105020](#), [arXiv:0801.0578](#).
- [42] SNO Collaboration, “Constraints on nucleon decay via ‘invisible’ modes from the Sudbury Neutrino Observatory”, *Phys. Rev. Lett.* **92** (2004) 102004, [doi:10.1103/PhysRevLett.92.102004](#), [arXiv:hep-ex/0310030](#).
- [43] P. Meade, N. Seiberg, and D. Shih, “General Gauge Mediation”, *Prog. Theor. Phys. Suppl.* **177** (2009) [doi:10.1143/PTPS.177.143](#), [arXiv:0801.3278](#).
- [44] P. Meade, M. Reece, and D. Shih, “Prompt Decays of General Neutralino NLSPs at the Tevatron”, *JHEP* **05** (2010) 105, [doi:10.1007/JHEP05\(2010\)105](#), [arXiv:0911.4130](#).

- [45] S. Dimopoulos, S. D. Thomas, and J. D. Wells, “Sparticle spectroscopy and electroweak symmetry breaking with gauge mediated supersymmetry breaking”, *Nucl. Phys. B* **488** (1997) doi:10.1016/S0550-3213(97)00030-8, arXiv:hep-ph/9609434.
- [46] S. Ambrosanio et al., “Search for supersymmetry with a light gravitino at the Fermilab Tevatron and CERN LEP colliders”, *Phys. Rev. D* **54** (1996) doi:10.1103/PhysRevD.54.5395, arXiv:hep-ph/9605398.
- [47] D. A. and Nima Arkani-Hamedet al., “Simplified models for lhc new physics searches”, *Journal of Physics G: Nuclear and Particle Physics* **39** (2012).
- [48] CMS Collaboration, “Interpretation of searches for supersymmetry with simplified models”, *Phys. Rev. D* **88** (2013) 052017, doi:10.1103/PhysRevD.88.052017.
- [49] S. Ask, “A Review of the supersymmetry searches at LEP”, in *38th Rencontres de Moriond on Electroweak Interactions and Unified Theories Les Arcs, France, March 15-22, 2003*. arXiv:hep-ex/0305007.
- [50] X. P. Bueso, “Supersymmetry Searches at the Tevatron and the LHC Collider Experiments”, in *Proceedings, 31st International Conference on Physics in collisions (PIC 2011): Vancouver, Canada, August 28-September 1, 2011*. arXiv:1112.1723.
- [51] C. Autermann, “Experimental status of supersymmetry after the LHC Run-I”, *Prog. Part. Nucl. Phys.* **90** (2016) doi:10.1016/j.ppnp.2016.06.001, arXiv:1609.01686.
- [52] CMS Collaboration, “Search for Physics Beyond the Standard Model in Events with Two Leptons, Jets, and Missing Transverse Momentum in pp Collisions at $\sqrt{s} = 8$ TeV”, *JHEP* **04** (2015) 124, doi:10.1007/JHEP04(2015)124, arXiv:1502.06031.
- [53] LHCb, CMS Collaboration, “Observation of the rare $B_s^0 \rightarrow \mu^+ \mu^-$ decay from the combined analysis of CMS and LHCb data”, *Nature* **522** (2015) doi:10.1038/nature14474, arXiv:1411.4413.
- [54] CMS Collaboration, “Search for Physics Beyond the Standard Model in Events with High-Momentum Higgs Bosons and Missing Transverse Momentum in Proton-Proton Collisions at 13 TeV”, *Phys. Rev. Lett.* **120** (2018) 241801, doi:10.1103/PhysRevLett.120.241801, arXiv:1712.08501.
- [55] CMS Collaboration, “Search for new phenomena in final states with two opposite-charge, same-flavor leptons, jets, and missing transverse momentum in pp collisions at $\sqrt{s} = 13$ TeV”, *JHEP* **03** (2018) 076, doi:10.1007/s13130-018-07845-2, 10.1007/JHEP03(2018)076, arXiv:1709.08908.
- [56] CMS Collaboration, “Search for top squarks and dark matter particles in opposite-charge dilepton final states at $\sqrt{s} = 13$ TeV”, *Phys. Rev. D* **97** (2018) 032009, doi:10.1103/PhysRevD.97.032009, arXiv:1711.00752.
- [57] CMS Collaboration, “Search for electroweak production of charginos and neutralinos in multilepton final states in proton-proton collisions at $\sqrt{s} = 13$ TeV”, *JHEP* **03** (2018) 166, doi:10.1007/JHEP03(2018)166, arXiv:1709.05406.
- [58] CMS Collaboration, “The CMS experiment at the CERN LHC”, *Journal of Instrumentation* **3** (2008).
- [59] CMS Collaboration, “CMS Supersymmetry Physics Results”. Accessed: 2018-09-25. <https://twiki.cern.ch/twiki/bin/view/CMSPublic/PhysicsResultsSUS>.

- [60] ATLAS Collaboration, “Search for supersymmetry in events with four or more leptons in $\sqrt{s} = 13$ TeV pp collisions with ATLAS”, *Phys. Rev. D* **98** (2018) 032009, doi:10.1103/PhysRevD.98.032009, arXiv:1804.03602.
- [61] ATLAS Collaboration, “Search for pair production of higgsinos in final states with at least three b -tagged jets in $\sqrt{s} = 13$ TeV pp collisions using the ATLAS detector”, *Phys. Rev.* (2018) arXiv:1806.04030.
- [62] ATLAS Collaboration, “Search for photonic signatures of gauge-mediated supersymmetry in 13 TeV pp collisions with the ATLAS detector”, *Phys. Rev. D* **97** (2018) 092006, doi:10.1103/PhysRevD.97.092006, arXiv:1802.03158.
- [63] J. L. Feng, “Naturalness and the Status of Supersymmetry”, *Ann. Rev. Nucl. Part. Sci.* **63** (2013) doi:10.1146/annurev-nucl-102010-130447, arXiv:1302.6587.
- [64] L. R. F. Castillo, “The large hadron collider”, in *The Search and Discovery of the Higgs Boson*, 2053-2571, pp. 3–1 to 3–9. Morgan & Claypool Publishers, 2015. doi:10.1088/978-1-6817-4078-2ch3.
- [65] L. Evans and P. Bryant, “Lhc machine”, *Journal of Instrumentation* **3** (2008).
- [66] G. Bachy et al., “The LEP collider”, *Part. Accel.* **26** (1990).
- [67] ALICE Collaboration, “The ALICE experiment at the CERN LHC”, *Journal of Instrumentation* **3** (2008).
- [68] ATLAS Collaboration, “The ATLAS Experiment at the CERN Large Hadron Collider”, *Journal of Instrumentation* **3** (2008).
- [69] LHCb Collaboration, “The LHCb Detector at the LHC”, *Journal of Instrumentation* **3** (2008).
- [70] E. Mobs, “The CERN accelerator complex - August 2018”, 2018. General Photo, Modified. <http://cds.cern.ch/record/2636343>.
- [71] W. Herr and B. Muratori, “Concept of luminosity”, in *Intermediate accelerator physics. Proceedings, CERN Accelerator School, Zeuthen, Germany, September 15-26, 2003*. 2003.
- [72] CMS Collaboration, “Public CMS data quality information”. Accessed: 2018-09-25. https://twiki.cern.ch/twiki/bin/view/CMSPublic/DataQuality#Dataset_For_Morion17_Conference.
- [73] CMS Collaboration, “CMS Physics: Technical Design Report Volume 1: Detector Performance and Software”. Technical Design Report CMS. 2006.
- [74] CMS Collaboration, “Description and performance of track and primary-vertex reconstruction with the CMS tracker”, *JINST* **9** (2014) P10009, doi:10.1088/1748-0221/9/10/P10009, arXiv:1405.6569.
- [75] CMS Collaboration, “Performance and operation of the CMS electromagnetic calorimeter”, *Journal of Instrumentation* **5** (2010).
- [76] CMS Collaboration, “The CMS ECAL performance with examples”, Technical Report CMS-CR-2013-430, CERN, Geneva, 2013.

- [77] CMS Collaboration, “Performance of CMS muon reconstruction in pp collision events at $\sqrt{s} = 7$ TeV”, *JINST* **7** (2012) P10002, doi:10.1088/1748-0221/7/10/P10002, arXiv:1206.4071.
- [78] CMS Collaboration, “The CMS trigger system”, *Journal of Instrumentation* **12** (2017).
- [79] CMS Collaboration, “The CMS trigger in Run 2”, Technical Report CMS-CR-2017-340, 2017.
- [80] CMS Collaboration, “Mini-AOD: A New Analysis Data Format for CMS”, *J. Phys. Conf. Ser.* **664** (2015) 072052, doi:10.1088/1742-6596/664/7/072052, arXiv:1702.04685.
- [81] CMS Collaboration, “CMSSW Application Framework”. Accessed: 2018-10-01. <https://twiki.cern.ch/twiki/bin/view/CMSPublic/WorkBookCMSSWFramework>.
- [82] D. Spiga et al., “The cms remote analysis builder (crab)”, in *Proceedings of the 14th International Conference on High Performance Computing*, HiPC’07. Springer-Verlag, Berlin, Heidelberg, 2007.
- [83] I. Bird, “Computing for the large hadron collider”, *Annual Review of Nuclear and Particle Science* **61** (2011) doi:10.1146/annurev-nucl-102010-130059, arXiv:<https://doi.org/10.1146/annurev-nucl-102010-130059>.
- [84] R. Brun and F. Rademakers, “Root - an object oriented data analysis framework”, *Nuclear Instruments and Methods in Physics Research Section A: Accelerators, Spectrometers, Detectors and Associated Equipment* **389** (1997) doi:[https://doi.org/10.1016/S0168-9002\(97\)00048-X](https://doi.org/10.1016/S0168-9002(97)00048-X). New Computing Techniques in Physics Research V.
- [85] R. Placakyte, “Parton Distribution Functions”, in *Proceedings, 31st International Conference on Physics in collisions (PIC 2011): Vancouver, Canada, August 28-September 1, 2011*. arXiv:1111.5452.
- [86] A. Afqat et al., “The cms dataset bookkeeping service”, *Journal of Physics: Conference Series* **119** (2008).
- [87] J. Alwall et al., “The automated computation of tree-level and next-to-leading order differential cross sections, and their matching to parton shower simulations”, *JHEP* **07** (2014) 079, doi:10.1007/JHEP07(2014)079, arXiv:1405.0301.
- [88] J. Alwall et al., “Comparative study of various algorithms for the merging of parton showers and matrix elements in hadronic collisions”, *Eur. Phys. J. C* **53** (2008) doi:10.1140/epjc/s10052-007-0490-5, arXiv:0706.2569.
- [89] J. Alwall et al., “MadGraph 5 : Going Beyond”, *JHEP* **06** (2011) 128, doi:10.1007/JHEP06(2011)128, arXiv:1106.0522.
- [90] R. Frederix and S. Frixione, “Merging meets matching in MC@NLO”, *JHEP* **12** (2012) 061, doi:10.1007/JHEP12(2012)061, arXiv:1209.6215.
- [91] T. Sjostrand, S. Mrenna, and P. Z. Skands, “PYTHIA 6.4 Physics and Manual”, *JHEP* **05** (2006) 026, doi:10.1088/1126-6708/2006/05/026, arXiv:hep-ph/0603175.
- [92] S. Frixione, P. Nason, and C. Oleari, “Matching NLO QCD computations with Parton Shower simulations: the POWHEG method”, *JHEP* **11** (2007) 070, doi:10.1088/1126-6708/2007/11/070, arXiv:0709.2092.

- [93] S. Alioli, P. Nason, C. Oleari, and E. Re, “A general framework for implementing NLO calculations in shower Monte Carlo programs: the POWHEG BOX”, *JHEP* **06** (2010) 043, doi:10.1007/JHEP06(2010)043, arXiv:1002.2581.
- [94] CMS Collaboration, “Event generator tunes obtained from underlying event and multiparton scattering measurements”, *Eur. Phys. J. C* **76** (2016) 155, doi:10.1140/epjc/s10052-016-3988-x, arXiv:1512.00815.
- [95] NNPDF Collaboration, “Parton distributions for the LHC Run II”, *JHEP* **04** (2015) 040, doi:10.1007/JHEP04(2015)040, arXiv:1410.8849.
- [96] S. Agostinelli et al., “Geant4 - a simulation toolkit”, *Nuclear Instruments and Methods in Physics Research Section A: Accelerators, Spectrometers, Detectors and Associated Equipment* **506** (2003) doi:[https://doi.org/10.1016/S0168-9002\(03\)01368-8](https://doi.org/10.1016/S0168-9002(03)01368-8).
- [97] A. Giammanco, “The fast simulation of the cms experiment”, *Journal of Physics: Conference Series* **513** (2014).
- [98] CMS Collaboration, “Recent Developments in CMS Fast Simulation”, *PoS ICHEP2016* (2016) 181, doi:10.22323/1.282.0181, arXiv:1701.03850.
- [99] J. Alwall et al., “The automated computation of tree-level and next-to-leading order differential cross sections, and their matching to parton shower simulations”, *JHEP* **07** (2014) 079, doi:10.1007/JHEP07(2014)079, arXiv:1405.0301.
- [100] M. Czakon and A. Mitov, “Top++: A Program for the Calculation of the Top-Pair Cross-Section at Hadron Colliders”, *Comput. Phys. Commun.* **185** (2014) 2930, doi:10.1016/j.cpc.2014.06.021, arXiv:1112.5675.
- [101] M. Grazzini, S. Kallweit, D. Rathlev, and M. Wiesemann, “ $W^\pm Z$ production at the LHC: fiducial cross sections and distributions in NNLO QCD”, *JHEP* **05** (2017) 139, doi:10.1007/JHEP05(2017)139, arXiv:1703.09065.
- [102] F. Cascioli et al., “ZZ production at hadron colliders in NNLO QCD”, *Phys. Lett. B* **735** (2014) doi:10.1016/j.physletb.2014.06.056, arXiv:1405.2219.
- [103] F. Caola, K. Melnikov, R. Röntsch, and L. Tancredi, “QCD corrections to ZZ production in gluon fusion at the LHC”, *Phys. Rev. D* **92** (2015) 094028, doi:10.1103/PhysRevD.92.094028, arXiv:1509.06734.
- [104] J. M. Campbell, R. K. Ellis, M. Czakon, and S. Kirchner, “Two loop correction to interference in $gg \rightarrow ZZ$ ”, *JHEP* **08** (2016) 011, doi:10.1007/JHEP08(2016)011, arXiv:1605.01380.
- [105] T. Gehrmann et al., “ W^+W^- Production at Hadron Colliders in Next to Next to Leading Order QCD”, *Phys. Rev. Lett.* **113** (2014) 212001, doi:10.1103/PhysRevLett.113.212001, arXiv:1408.5243.
- [106] M. Grazzini, S. Kallweit, and D. Rathlev, “ZZ production at the LHC: fiducial cross sections and distributions in NNLO QCD”, *Phys. Lett. B* **750** (2015) doi:10.1016/j.physletb.2015.09.055, arXiv:1507.06257.
- [107] M. Grazzini, S. Kallweit, D. Rathlev, and M. Wiesemann, “ $W^\pm Z$ production at hadron colliders in NNLO QCD”, *Phys. Lett. B* **761** (2016) doi:10.1016/j.physletb.2016.08.017, arXiv:1604.08576.

- [108] W. Beenakker, R. Hopker, M. Spira, and P. M. Zerwas, “Squark and gluino production at hadron colliders”, *Nucl. Phys. B* **492** (1997) doi:10.1016/S0550-3213(97)80027-2, arXiv:hep-ph/9610490.
- [109] A. Kulesza and L. Motyka, “Threshold resummation for squark-antisquark and gluino-pair production at the LHC”, *Phys. Rev. Lett.* **102** (2009) 111802, doi:10.1103/PhysRevLett.102.111802, arXiv:0807.2405.
- [110] A. Kulesza and L. Motyka, “Soft gluon resummation for the production of gluino-gluino and squark-antisquark pairs at the LHC”, *Phys. Rev. D* **80** (2009) 095004, doi:10.1103/PhysRevD.80.095004, arXiv:0905.4749.
- [111] W. Beenakker et al., “Soft-gluon resummation for squark and gluino hadroproduction”, *JHEP* **12** (2009) 041, doi:10.1088/1126-6708/2009/12/041, arXiv:0909.4418.
- [112] W. Beenakker et al., “Squark and Gluino Hadroproduction”, *Int. J. Mod. Phys. A* **26** (2011) doi:10.1142/S0217751X11053560, arXiv:1105.1110.
- [113] C. Borschensky et al., “Squark and gluino production cross sections in pp collisions at $\sqrt{s} = 13, 14, 33$ and 100 TeV”, *Eur. Phys. J. C* **74** (2014) 3174, doi:10.1140/epjc/s10052-014-3174-y, arXiv:1407.5066.
- [114] W. Beenakker et al., “The Production of charginos / neutralinos and sleptons at hadron colliders”, *Phys. Rev. Lett.* **83** (1999) doi:10.1103/PhysRevLett.100.029901, 10.1103/PhysRevLett.83.3780, arXiv:hep-ph/9906298. [Erratum: Phys. Rev. Lett.100,029901(2008)].
- [115] B. Fuks, M. Klasen, D. R. Lamprea, and M. Rothering, “Gaugino production in proton-proton collisions at a center-of-mass energy of 8 TeV”, *JHEP* **10** (2012) 081, doi:10.1007/JHEP10(2012)081, arXiv:1207.2159.
- [116] B. Fuks, M. Klasen, D. R. Lamprea, and M. Rothering, “Precision predictions for electroweak superpartner production at hadron colliders with Resummino”, *Eur. Phys. J. C* **73** (2013) 2480, doi:10.1140/epjc/s10052-013-2480-0, arXiv:1304.0790.
- [117] CMS Collaboration, “Search for top-squark pair production in the single-lepton final state in pp collisions at $\sqrt{s} = 8$ TeV”, *Eur. Phys. J. C* **73** (2013) 2677, doi:10.1140/epjc/s10052-013-2677-2, arXiv:1308.1586.
- [118] CMS Collaboration, “Measurement of the differential cross section for $t\bar{t}$ production in the dilepton final state at $\sqrt{s} = 13$ TeV”, Technical Report CMS-PAS-TOP-16-011, 2016.
- [119] CMS Collaboration, “Measurement of differential cross sections for top quark pair production using the lepton+jets final state in proton-proton collisions at 13 TeV”, *Phys. Rev. D* **95** (2017) 092001, doi:10.1103/PhysRevD.95.092001, arXiv:1610.04191.
- [120] CMS Collaboration, “Measurement of the differential cross section for top quark pair production in pp collisions at $\sqrt{s} = 8$ TeV”, *Eur. Phys. J. C* **75** (2015) 542, doi:10.1140/epjc/s10052-015-3709-x, arXiv:1505.04480.
- [121] CMS Collaboration, “Measurement of the $t\bar{t}$ production cross section in the all-jets final state in pp collisions at $\sqrt{s} = 8$ TeV”, *Eur. Phys. J. C* **76** (2016) 128, doi:10.1140/epjc/s10052-016-3956-5, arXiv:1509.06076.
- [122] CMS Collaboration, “Particle-flow reconstruction and global event description with the CMS detector”, *JINST* **12** (2017) P10003, doi:10.1088/1748-0221/12/10/P10003, arXiv:1706.04965.

- [123] W. Adam, B. Mangano, T. Speer, and T. Todorov, “Track Reconstruction in the CMS tracker”, Technical Report CMS-NOTE-2006-041, 2006.
- [124] T. Speer et al., “Vertex Fitting in the CMS Tracker”, Technical Report CMS-NOTE-2006-032, CERN, Geneva, Feb, 2006.
- [125] CMS Collaboration, “MET Filter Recommendations for Run II”. Accessed: 2018-10-10.
<https://twiki.cern.ch/twiki/bin/view/CMS/MissingETOptionalFiltersRun2?rev=119>.
- [126] A. M. Sirunyan et al., “Performance of the CMS muon detector and muon reconstruction with proton-proton collisions at $\sqrt{s} = 13$ TeV”,.
- [127] CMS Collaboration, “Cut Based Electron ID for Run 2”. Accessed: 2018-10-08.
<https://twiki.cern.ch/twiki/bin/view/CMS/CutBasedElectronIdentificationRun2?rev=59>.
- [128] CMS Collaboration, “Cut Based Photon ID for Run 2”. Accessed: 2018-10-09. <https://twiki.cern.ch/twiki/bin/view/CMS/CutBasedPhotonIdentificationRun2?rev=46>.
- [129] M. Cacciari, G. P. Salam, and G. Soyez, “The anti- k_t jet clustering algorithm”, *JHEP* **04** (2008) 063, doi:10.1088/1126-6708/2008/04/063, arXiv:0802.1189.
- [130] M. Cacciari, G. P. Salam, and G. Soyez, “FastJet User Manual”, *Eur. Phys. J. C* **72** (2012) 1896, doi:10.1140/epjc/s10052-012-1896-2, arXiv:1111.6097.
- [131] M. Cacciari and G. P. Salam, “Dispelling the N^3 myth for the k_t jet-finder”, *Phys. Lett. B* **641** (2006) doi:10.1016/j.physletb.2006.08.037, arXiv:hep-ph/0512210.
- [132] CMS Collaboration, “Jet energy scale and resolution in the CMS experiment in pp collisions at 8 TeV”, *JINST* **12** (2017) P02014, doi:10.1088/1748-0221/12/02/P02014, arXiv:1607.03663.
- [133] CMS Collaboration, “Jet Identification for the 13 TeV data Run2016”. Accessed: 2018-10-09.
<https://twiki.cern.ch/twiki/bin/view/CMS/JetID13TeVRun2016?rev=11>.
- [134] A. Barr, C. Lester, and P. Stephens, “m(T2): The Truth behind the glamour”, *J. Phys. G* **29** (2003) doi:10.1088/0954-3899/29/10/304, arXiv:hep-ph/0304226.
- [135] C. G. Lester and D. J. Summers, “Measuring masses of semiinvisibly decaying particles pair produced at hadron colliders”, *Phys. Lett. B* **463** (1999) doi:10.1016/S0370-2693(99)00945-4, arXiv:hep-ph/9906349.
- [136] C. J. Clopper and E. S. Pearson, “The use of confidence or fiducial limits illustrated in the case of the binomial”, *Biometrika* **26** (1934).
- [137] “Kolmogorov–Smirnov Test”. Springer New York, New York, NY, 2008. doi:10.1007/978-0-387-32833-1_214.
- [138] CMS Collaboration, “CMS Luminosity Measurements for the 2016 Data Taking Period”, Technical Report CMS-PAS-LUM-17-001, 2017.
- [139] T.-P. Li and Y. Ma, “Analysis methods for results in gamma-ray astronomy”, *The Astrophysical Journal* **272** (1983) doi:10.1086/161295.

- [140] R. D. Cousins, J. T. Linnemann, and J. Tucker, “Evaluation of three methods for calculating statistical significance when incorporating a systematic uncertainty into a test of the background-only hypothesis for a poisson process”, *Nuclear Instruments and Methods in Physics Research Section A: Accelerators, Spectrometers, Detectors and Associated Equipment* **595** (2008) doi:<https://doi.org/10.1016/j.nima.2008.07.086>.
- [141] T. Junk, “Confidence level computation for combining searches with small statistics”, *Nucl. Instrum. Meth. A* **434** (1999) doi:[10.1016/S0168-9002\(99\)00498-2](https://doi.org/10.1016/S0168-9002(99)00498-2), arXiv:[hep-ex/9902006](https://arxiv.org/abs/hep-ex/9902006).
- [142] A. L. Read, “Presentation of search results: the cl s technique”, *Journal of Physics G: Nuclear and Particle Physics* **28** (2002).
- [143] The ATLAS Collaboration, The CMS Collaboration, The LHC Higgs Combination Group Collaboration, “Procedure for the LHC Higgs boson search combination in Summer 2011”, Technical Report CMS-NOTE-2011-005. ATL-PHYS-PUB-2011-11, 2011.
- [144] G. Cowan, K. Cranmer, E. Gross, and O. Vitells, “Asymptotic formulae for likelihood-based tests of new physics”, *Eur. Phys. J. C* **71** (2011) 1554, doi:[10.1140/epjc/s10052-011-1554-0](https://doi.org/10.1140/epjc/s10052-011-1554-0), doi:[10.1140/epjc/s10052-013-2501-z](https://doi.org/10.1140/epjc/s10052-013-2501-z), arXiv:[1007.1727](https://arxiv.org/abs/1007.1727). [Erratum: Eur. Phys. J.C73,2501(2013)].
- [145] E. Gross and O. Vitells, “Trial factors for the look elsewhere effect in high energy physics”, *The European Physical Journal C* **70** (2010) doi:[10.1140/epjc/s10052-010-1470-8](https://doi.org/10.1140/epjc/s10052-010-1470-8).
- [146] J. Neyman and E. S. Pearson, “Ix. on the problem of the most efficient tests of statistical hypotheses”, *Philosophical Transactions of the Royal Society of London A: Mathematical, Physical and Engineering Sciences* **231** (1933) doi:[10.1098/rsta.1933.0009](https://doi.org/10.1098/rsta.1933.0009), arXiv:<http://rsta.royalsocietypublishing.org/content/231/694-706/289.full.pdf>.
- [147] D. Meuser et al., “Combined search for supersymmetry with general gauge mediation in events with photons in pp collisions at 13 TeV”, *CMS Analysis Note* **18-287** (2018).

A

Data sets

In Table A.1 the DBS paths for all used data sets in the analysis are given. The data sets are divided into several primary data sets (PD), where the same-flavor data sets are used for the signal selection, the different-flavor data sets are used for the background prediction, and the p_T^{miss} and H_T data sets are used for the trigger efficiency measurement. Each group of data sets is subdivided into several run eras (B-H), and the 2017 version of reconstruction is used.

Table A.1.: DBS paths for the data sets used in the analysis. Their paths are similar, only the PD names vary. The dilepton data sets are used for the key analysis, whereas the H_T and p_T^{miss} data sets are used for the trigger efficiency measurement, see Section 4.6.

PDs	DoubleEG DoubleMu MuonEG HT MET
DBS path	/PD/Run2016B-03Feb2017_ver2-v2/MINIAOD /PD/Run2016C-03Feb2017-v1/MINIAOD /PD/Run2016D-03Feb2017-v1/MINIAOD /PD/Run2016E-03Feb2017-v1/MINIAOD /PD/Run2016F-03Feb2017-v1/MINIAOD /PD/Run2016G-03Feb2017-v1/MINIAOD /PD/Run2016H-03Feb2017_ver2-v1/MINIAOD /PD/Run2016H-03Feb2017_ver3-v1/MINIAOD

B

Simulated data sets

Simulated standard model data sets

In Table B.1 the DBS paths of the used SM simulated data sets are given together with their cross sections used for the normalization of the processes. In cases where NLO to NNLO k-factors are used, this is also stated in the table.

Simulated signal data sets

In Table B.2 the DBS paths for the used signal simulated data sets are given. Because in each signal data set very different parameter masses are used in the generation, many cross sections are used for the rescaling of the simulation, and are not quoted in the table.

Table B.1.: All SM MC samples used in the analysis with their cross section. In the case k-factors are applied, they are given separately. The abbreviation $\{\dots\}$ stands for `RunIISummer16MiniAODv2-PUMoriond17_80X_mcRun2_asymptotic_2016_TrancheIV_v6`. All samples are of the MINIAODSIM format. Additional k-factors to obtain NNLO cross sections for the ZZ samples are applied per event in dependence of the p_T of the diboson system.

process	data set	$\sigma \cdot k [\text{pb}]$
tt		
$t\bar{t} \rightarrow \ell^+ \nu b + \ell^- \bar{\nu} b$	/TTTo2L2Nu_Tune*_ttHtranche3_13TeV-powheg-pythia8/\{\dots\}-v1	87.31
ttγ		
$t\bar{t}\gamma$	/TTGamma_Dilept_Tune*_13TeV-amcatnlo-pythia8/\{\dots\}-v2	1.679
	/TTGamma_Hadronic_Tune*_13TeV-amcatnlo-pythia8/\{\dots\}-v2	3.482
	/TTGamma_SingleLeptFromT_Tune*_13TeV-amcatnlo-pythia8/\{\dots\}-v2	2.509
	/TTGamma_SingleLeptFromTbar_Tune*_13TeV-amcatnlo-pythia8/\{\dots\}-v2	2.509
Drell-Yan		
$Z/\gamma^* \rightarrow 2\ell$	/DYJetsToLL_M-50_TuneCUETP8M1_13TeV-amcatnloFXFX-pythia8/\{\dots\}_ext2-v1	5765.4
diboson		
$Z\gamma \rightarrow 2\ell\gamma$	/ZGTo2LG_Tune*_13TeV-amcatnloFXFX-pythia8/\{\dots\}_ext1-v1	117.864 · 1.06
	/ZGTo2LG_Tune*_13TeV-amcatnloFXFX-pythia8/\{\dots\}-v1	117.864 · 1.06
	/ZGTo2LG_PtG-130_Tune*_13TeV-amcatnloFXFX-pythia8/\{\dots\}-v1	0.1404 · 1.06
WZ	/WZTo3LNu_Tune*_13TeV-powheg-pythia8/\{\dots\}-v1	4.42965 · 1.109
	/WZTo3LNu_Tune*_13TeV-powheg-pythia8/\{\dots\}_ext1-v3	4.42965 · 1.109
$ZZ \rightarrow 2\ell 2\nu$	/ZZTo2L2Nu_13TeV_powheg_pythia8_ext1/\{\dots\}-v1	0.5644 · $k(p_T^{ZZ})$
	/ZZTo2L2Nu_13TeV_powheg_pythia8/\{\dots\}-v1	0.5644 · $k(p_T^{ZZ})$
$ZZ \rightarrow 4\ell$	/ZZTo4L_13TeV_powheg_pythia8/\{\dots\}-v1	1.212 · $k(p_T^{ZZ})$
	/ZZTo4L_13TeV_powheg_pythia8_ext1/\{\dots\}-v1	1.212 · $k(p_T^{ZZ})$
$WW \rightarrow 2\ell 2\nu$	/WWTo2L2Nu_13TeV-powheg/\{\dots\}-v1	12.178
$Wg \rightarrow \ell \nu g$	/WGToLNuG_Tune*_13TeV-amcatnloFXFX-pythia8/\{\dots\}_ext3-v1	489
W+jets		
$W + jets$	/WJetsToLNu_Tune*_13TeV-amcatnloFXFX-pythia8/\{\dots\}_ext2-v2	61526.7
	/WJetsToLNu_Tune*_13TeV-amcatnloFXFX-pythia8/\{\dots\}-v1	61526.7
triboson		
WWg	/WWG_Tune*_13TeV-amcatnlo-pythia8/\{\dots\}_ext1-v1	0.2147
WZg	/WZG_Tune*_13TeV-amcatnlo-pythia8/\{\dots\}-v1	0.04123
single top		
$W^+ \rightarrow t\bar{b}$	/ST_s-channel_4f_leptonDecays_13TeV-amcatnlo-pythia8_*/\{\dots\}-v1	3.36
$q\bar{b} \rightarrow q'\bar{t}$	/ST_t-channel_antitop_4f_incl*Decays_13TeV-powhegV2--pythia8_*/\{\dots\}-v1	80.95
$qb \rightarrow q'\bar{t}$	/ST_t-channel_top_4f_incl*Decays_13TeV-powhegV2--pythia8_*/\{\dots\}-v1	136.02
$\bar{b} \rightarrow W^+\bar{t}$	/ST_tW_antitop_5f_NoFullyHadronicDecays_13TeV-powheg_*/\{\dots\}_ext1-v1	11.7
$b \rightarrow W^-\bar{t}$	/ST_tW_top_5f_NoFullyHadronicDecays_13TeV-powheg_*/\{\dots\}_ext1-v1	11.7

Table B.2.: All SUSY MC samples used in the analysis. The abbreviation $\{\dots\}$ stands for `80X_mcRun2_asymptotic_2016`. All samples are of the MINIAODSIM format.

signal	data set
electroweak production	
TChiNG	/SMS-TChiNG_BF50N50G_*/RunIISpring16MiniAODv2-PUSpring16Fast_{\dots}_miniAODv2_v0-v1
GMSB	/GMSB_GravitinoLSP_N1decays_*/RunIISummer16MiniAODv2-PUSummer16Fast_{\dots}_TrancheIV_v6-v1
strong production	
T5bbbbZG	/SMS-T5bbbbZg_*/RunIISummer16MiniAODv2-PUSummer16Fast_{\dots}_TrancheIV_v6-v2

C

Signal properties

In this chapter, properties of the three signal models considered in the interpretation of this analysis are given.

Signal cross section

The production cross sections for the two simplified models and the GMSB model are shown in Figure C.1 in the corresponding parameter mass planes. For the GMSB model, the production cross section depends only on the wino mass, since $\tilde{\chi}_2^0 \tilde{\chi}_1^\pm$ and $\tilde{\chi}_1^\mp \tilde{\chi}_1^\pm$ are by far the most dominant production channels and both the chargino and the neutralino are wino-like, see Section 2.3.2. Since in the T5bbbbZG SMS only gluino production is considered, the gluino mass determines the cross section. In the TChizG SMS, only neutralino-chargino and chargino-chargino production is assumed.

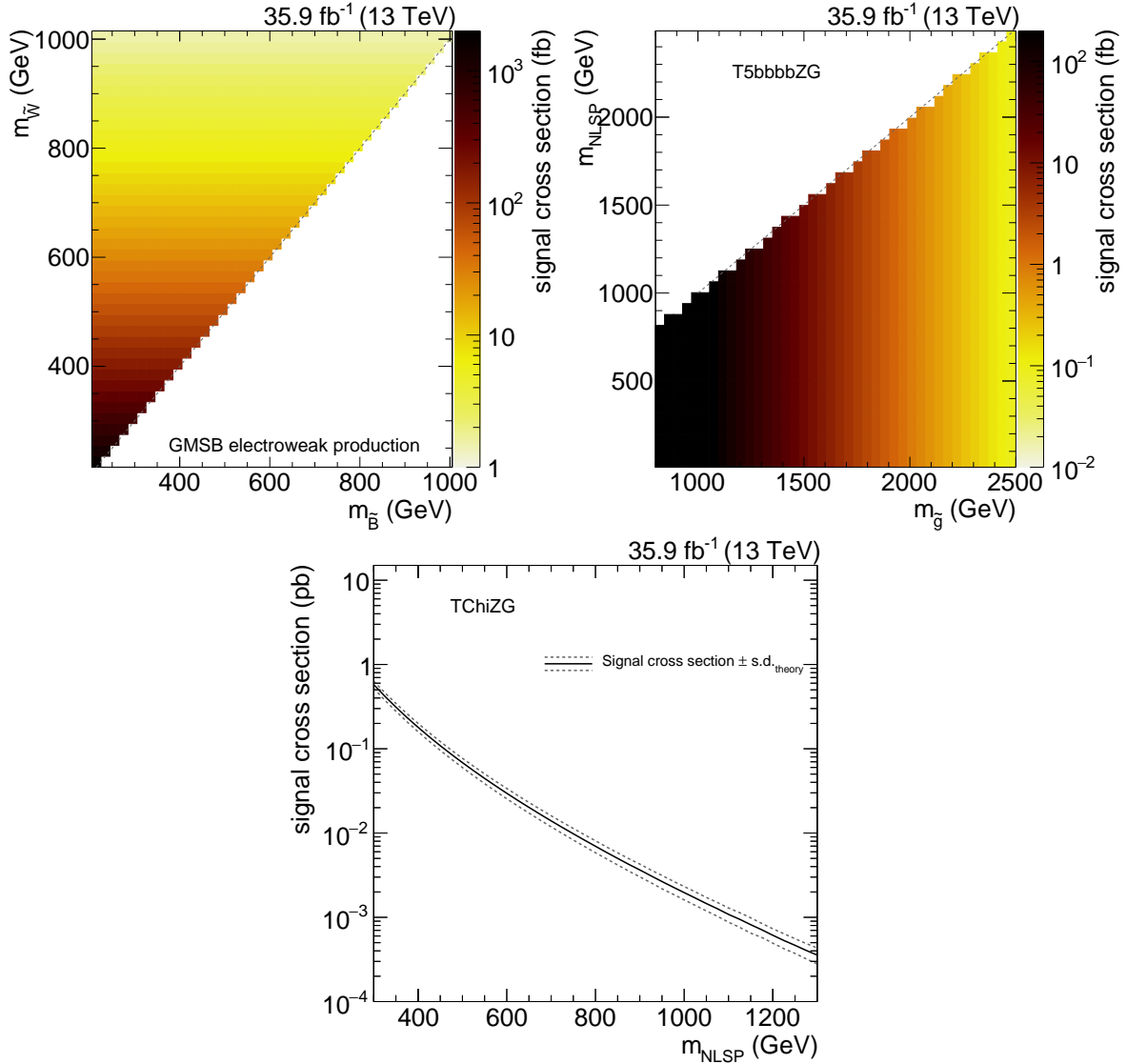


Figure C.1.: In the upper row, production cross sections for the GMSB model (left) and T5bbbbZG SMS are given in the $m(\tilde{B})$ - $m(\tilde{W})$ and $m(\text{NLSP})$ - $m(\tilde{g})$ mass plane, respectively. The considered production cross section for the TChiZG model is given in the lower row.

Event selection acceptance

The total event selection acceptances, see Section 6 for the definition, are shown in Figure C.2 for all three signal models. They are in the order of $\mathcal{O}(1\%)$, slightly depending on the sparticle masses. In general, for higher sparticle masses the acceptance increases, since the final state particles carry much more energy and the probability to be selected in the SR is larger. For low NLSP masses in case of the T5bbbbZG SMS, the acceptance decreases due to the M_{T2} requirement of 100 GeV. The acceptance is enhanced for the GMSB model, if the mass difference between the wino and bino is approximately 90 GeV, because additional Z bosons are produced in decays of sparticles in the cascades.

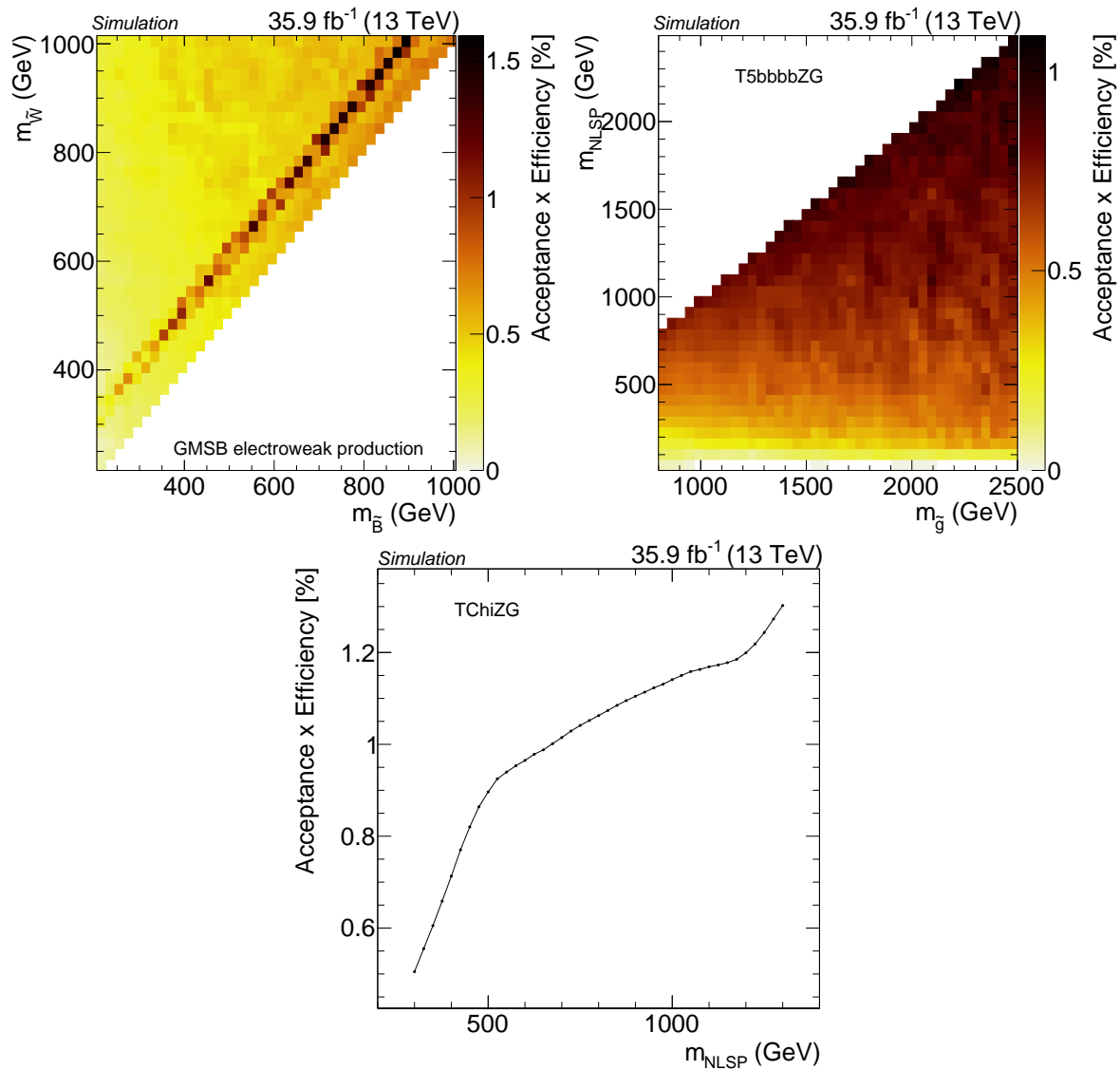


Figure C.2.: In the upper row, the event selection acceptance for the GMSB model (left) and T5bbbbZG SMS is shown in the $m(\tilde{B})$ - $m(\tilde{W})$ and $m(\text{NLSP})$ - $m(\tilde{g})$ mass plane, respectively. The acceptance for the TChiZG model is given in the lower row.

D

Trigger paths

In Tables D.1 and D.2 all HLT trigger paths used in the analysis are quoted. The trigger paths in the first table are relevant for the signal event selection and the background prediction, while the HLT paths stated in the second table are needed for the trigger efficiency measurement.

Table D.1.: Trigger paths used for the signal and control region event selection.

dielectron trigger	
HLT_Ele17_Ele12_CaloIdL_TrackIdL_IsoVL_DZ_v*	
HLT_Ele23_Ele12_CaloIdL_TrackIdL_IsoVL_DZ_v*	
HLT_DoubleEle33_CaloIdL_GsfTrkIdVL_v*	
HLT_DoubleEle33_CaloIdL_GsfTrkIdVL_MW_v*	
dimuon trigger	
HLT_Mu17_TrkIsoVVL_Mu8_TrkIsoVVL_v*	
HLT_Mu17_TrkIsoVVL_TkMu8_TrkIsoVVL_v*	
HLT_Mu17_TrkIsoVVL_Mu8_TrkIsoVVL_DZ_v*	
HLT_Mu17_TrkIsoVVL_TkMu8_TrkIsoVVL_DZ_v*	
HLT_TkMu17_TrkIsoVVL_TkMu8_TrkIsoVVL_DZ_v*	
HLT_Mu27_TkMu8_v*	
HLT_Mu30_TkMu11_v*	
electron-muon trigger	
HLT_Mu17_TrkIsoVVL_Ele12_CaloIdL_TrackIdL_IsoVL_v*	
HLT_Mu23_TrkIsoVVL_Ele8_CaloIdL_TrackIdL_IsoVL_v*	
HLT_Mu23_TrkIsoVVL_Ele8_CaloIdL_TrackIdL_IsoVL_DZ_v*	
HLT_Mu23_TrkIsoVVL_Ele12_CaloIdL_TrackIdL_IsoVL_v*	
HLT_Mu23_TrkIsoVVL_Ele12_CaloIdL_TrackIdL_IsoVL_DZ_v*	
HLT_Mu8_TrkIsoVVL_Ele17_CaloIdL_TrackIdL_IsoVL_v*	
HLT_Mu8_TrkIsoVVL_Ele23_CaloIdL_TrackIdL_IsoVL_v*	
HLT_Mu8_TrkIsoVVL_Ele23_CaloIdL_TrackIdL_IsoVL_DZ_v*	
HLT_Mu12_TrkIsoVVL_Ele23_CaloIdL_TrackIdL_IsoVL_v*	
HLT_Mu12_TrkIsoVVL_Ele23_CaloIdL_TrackIdL_IsoVL_DZ_v*	
HLT_Mu30_Ele30_CaloIdL_GsfTrkIdVL_v*	
HLT_Mu33_Ele33_CaloIdL_GsfTrkIdVL_v*	

Table D.2.: Trigger paths used for the trigger efficiency measurements.

HT trigger	
HLT_PFHT200_v*	
HLT_PFHT250_v*	
HLT_PFHT300_v*	
HLT_PFHT350_v*	
HLT_PFHT400_v*	
HLT_PFHT475_v*	
HLT_PFHT600_v*	
HLT_PFHT650_v*	
HLT_PFHT800_v*	
MET trigger	
HLT_PFMET110_PFMHT110_IDTight_v*	
HLT_PFMET120_PFMHT120_IDTight_v*	
HLT_PFMET170_NoiseCleaned_v	*
HLT_PFMET170_HBHECleaned_v*	
HLT_PFMET170_JetIdCleaned_v*	
HLT_PFMET170_NotCleaned_v*	
HLT_PFMET300_v*	
HLT_PFMET400_v*	
HLT_PFMET500_v*	
HLT_PFMET600_v*	

Trigger efficiency measurement

In Figure D.1, the trigger efficiency measurement for the leading lepton leg of the dilepton triggers is shown. As can be seen, the triggers are efficient for $p_T > 25 \text{ GeV}$ for the leading leptons. Additional distributions for the efficiency in the p_T^{miss} and H_T distribution are shown in Figure D.2 and Figure D.3, after applying both lepton p_T requirements (25 GeV for the leading, and 20 GeV for the trailing lepton). No inefficiencies are observed.

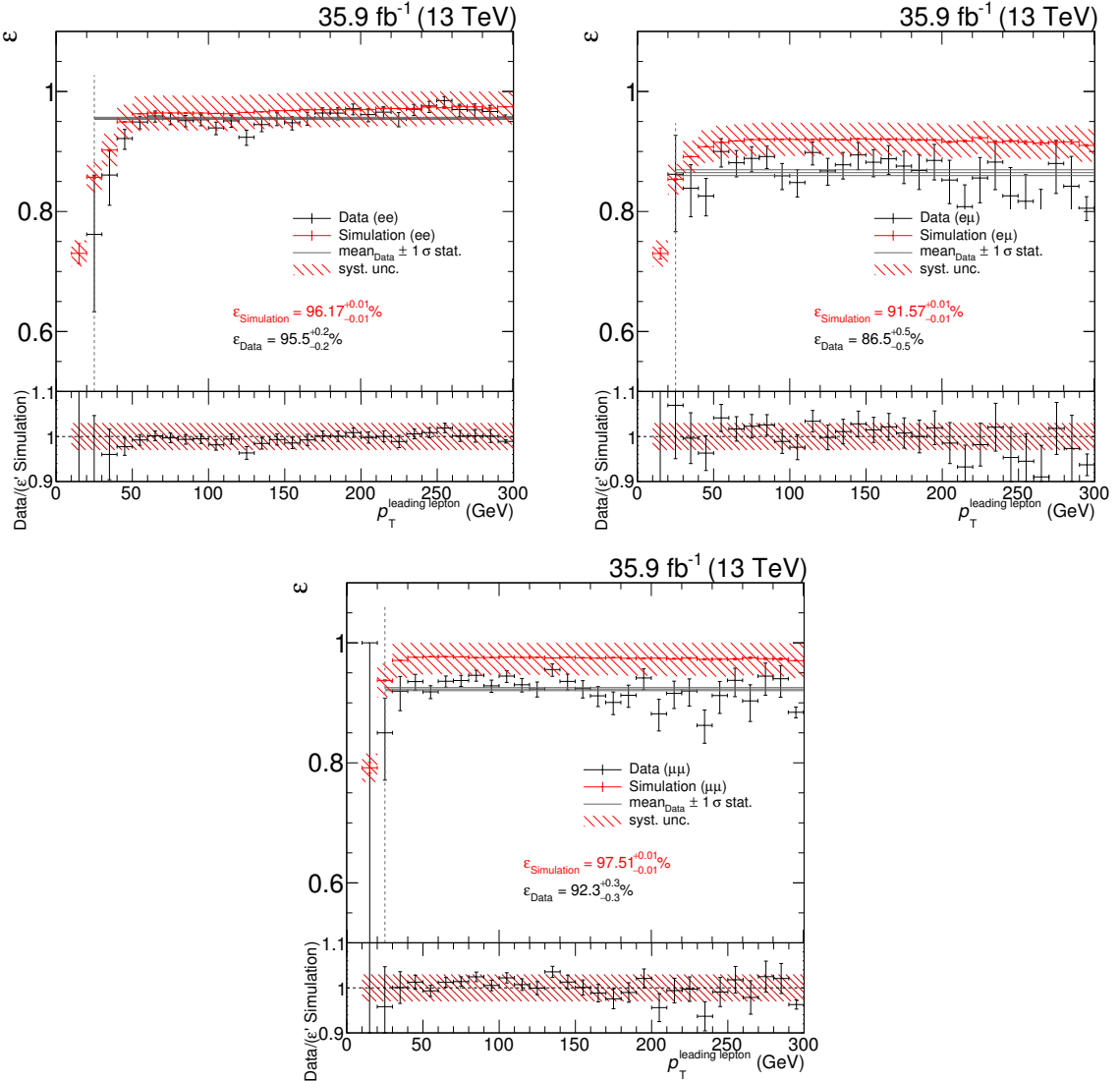


Figure D.1.: Measurement of the combined efficiency in the p_T distribution of the leading lepton for all dilepton trigger combinations on data (black) and simulation (red) for the ee (top left), e μ (top right), and $\mu\mu$ (bottom) channels. The measurement is performed using various H_T baseline triggers, while the selection consists of the lepton pair preselection, and a $H_T > 200$ GeV requirement. The mean of the data efficiency with its statistical uncertainty (gray band), and the 3% systematic uncertainty on the measurement (red band) are also shown. In the bottom panel of each plot, the ratio between the efficiency measured on data and the simulation scaled with the reweighting factor ϵ' is depicted.

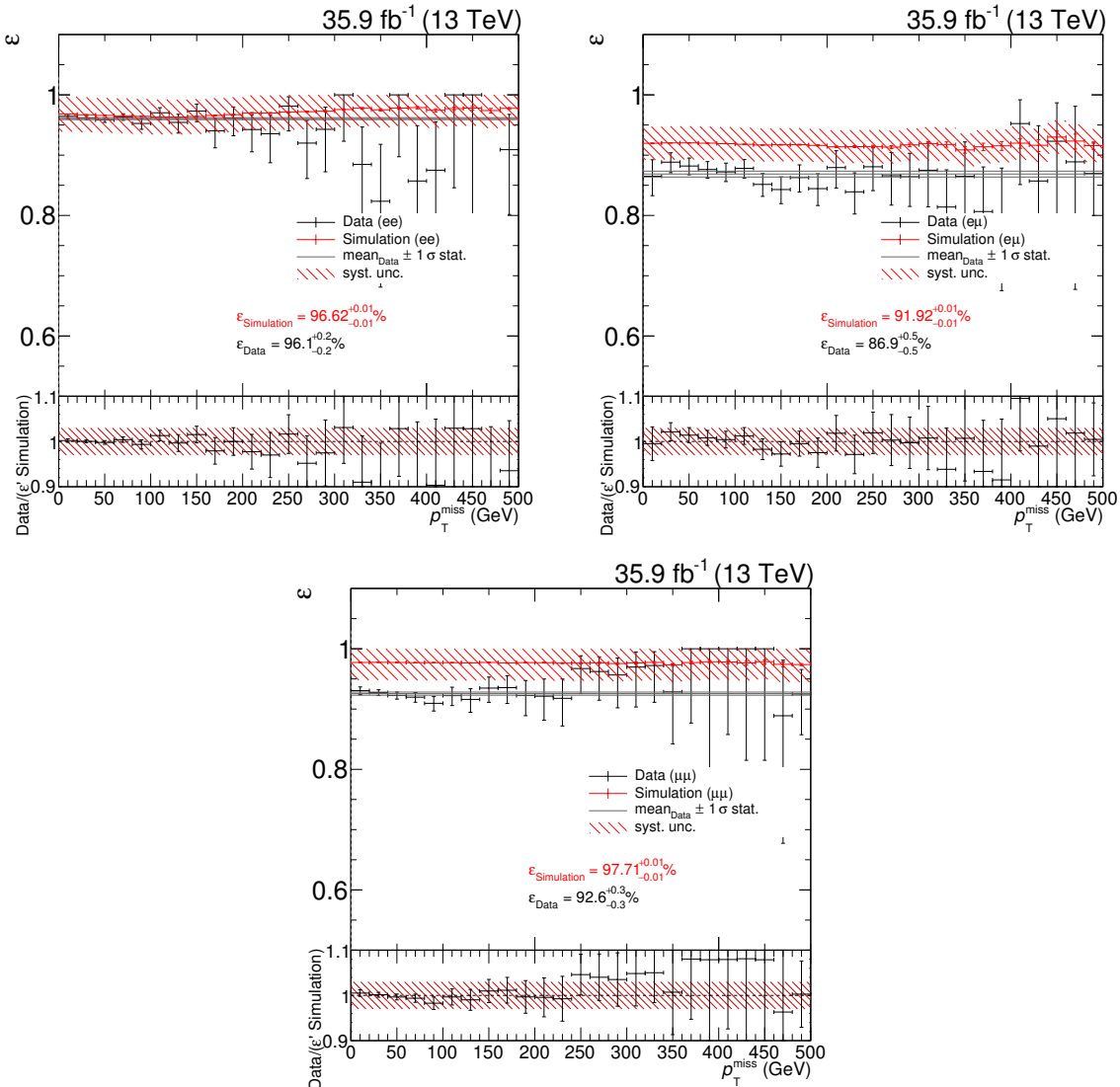


Figure D.2.: Measurement of the combined efficiency in the p_T^{miss} distribution for all dilepton trigger combinations on data (black) and simulation (red) for the ee (top left), e μ (top right), and $\mu\mu$ (bottom) channels. The measurement is performed using various H_T baseline triggers, while the selection consists of the lepton pair preselection, and a $H_T > 200 \text{ GeV}$ requirement. The mean of the data efficiency with its statistical uncertainty (gray band), and the 3% systematic uncertainty on the measurement (red band) are also shown. In the bottom panel of each plot, the ratio between the efficiency measured on data and the simulation scaled with the reweighting factor ϵ' is depicted.

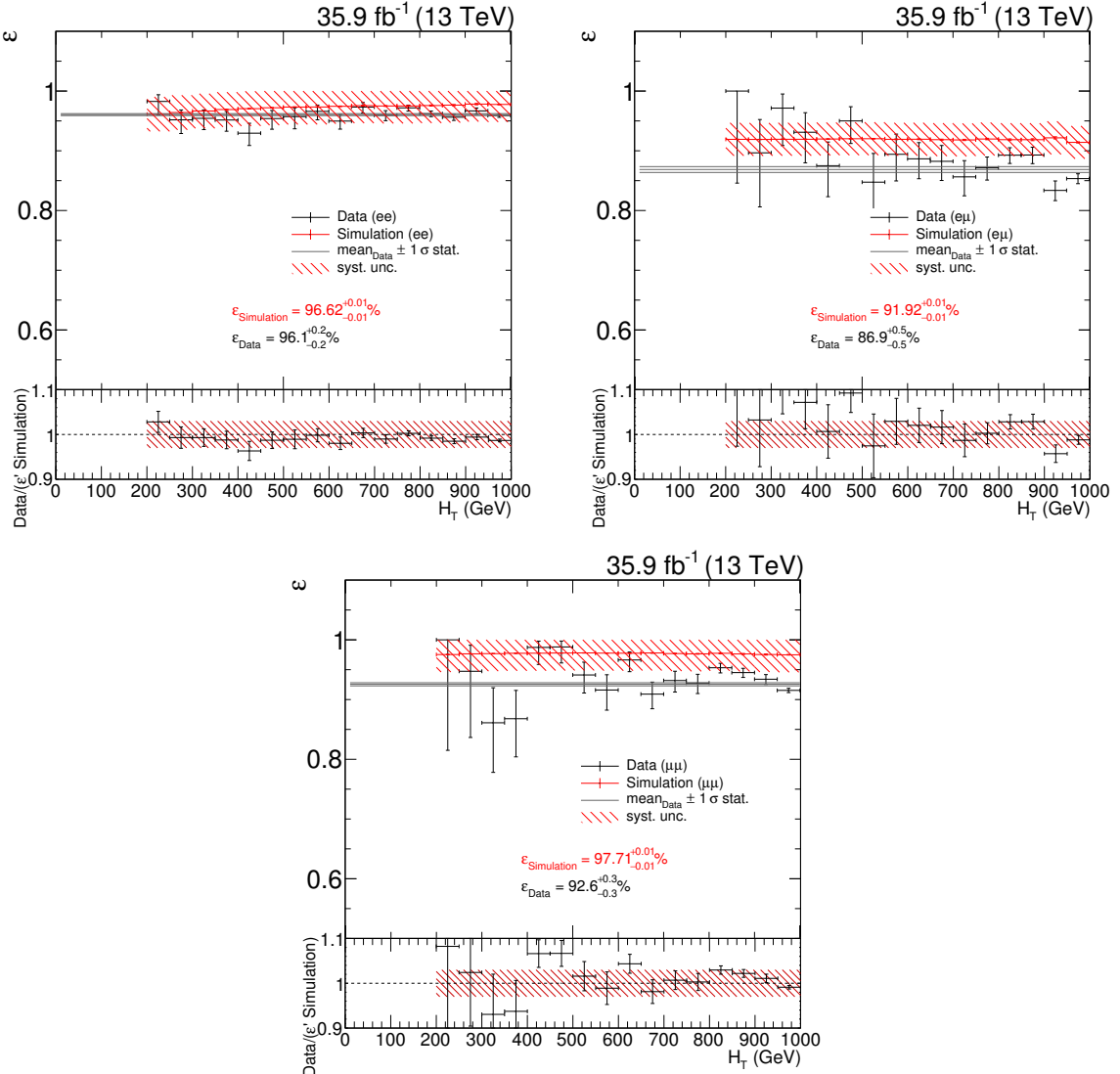


Figure D.3.: Measurement of the combined efficiency in the H_T distribution for all dilepton trigger combinations on data (black) and simulation (red) for the ee (top left), e μ (top right), and $\mu\mu$ (bottom) channels. The measurement is performed using various H_T baseline triggers, while the selection consists of the lepton pair preselection, and a $H_T > 200$ GeV requirement. The mean of the data efficiency with its statistical uncertainty (gray band), and the 3% systematic uncertainty on the measurement (red band) are also shown. In the bottom panel of each plot, the ratio between the efficiency measured on data and the simulation scaled with the reweighting factor ϵ' is depicted.

Eidesstattliche Versicherung

Statutory Declaration in Lieu of an Oath

Name, Vorname/Last Name, First Name

Matrikelnummer (freiwillige Angabe)

Matriculation No. (optional)

Ich versichere hiermit an Eides Statt, dass ich die vorliegende Arbeit/Bachelorarbeit/
Masterarbeit* mit dem Titel

I hereby declare in lieu of an oath that I have completed the present paper/Bachelor thesis/Master thesis* entitled

selbstständig und ohne unzulässige fremde Hilfe (insbes. akademisches Ghostwriting) erbracht habe. Ich habe keine anderen als die angegebenen Quellen und Hilfsmittel benutzt. Für den Fall, dass die Arbeit zusätzlich auf einem Datenträger eingereicht wird, erkläre ich, dass die schriftliche und die elektronische Form vollständig übereinstimmen. Die Arbeit hat in gleicher oder ähnlicher Form noch keiner Prüfungsbehörde vorgelegen.

independently and without illegitimate assistance from third parties (such as academic ghostwriters). I have used no other than the specified sources and aids. In case that the thesis is additionally submitted in an electronic format, I declare that the written and electronic versions are fully identical. The thesis has not been submitted to any examination body in this, or similar, form.

Ort, Datum/City, Date

Unterschrift/Signature

*Nichtzutreffendes bitte streichen

*Please delete as appropriate

Belehrung:

Official Notification:

§ 156 StGB: Falsche Versicherung an Eides Statt

Wer vor einer zur Abnahme einer Versicherung an Eides Statt zuständigen Behörde eine solche Versicherung falsch abgibt oder unter Berufung auf eine solche Versicherung falsch aussagt, wird mit Freiheitsstrafe bis zu drei Jahren oder mit Geldstrafe bestraft.

Para. 156 StGB (German Criminal Code): False Statutory Declarations

Whoever before a public authority competent to administer statutory declarations falsely makes such a declaration or falsely testifies while referring to such a declaration shall be liable to imprisonment not exceeding three years or a fine.

§ 161 StGB: Fahrlässiger Falscheid; fahrlässige falsche Versicherung an Eides Statt

(1) Wenn eine der in den §§ 154 bis 156 bezeichneten Handlungen aus Fahrlässigkeit begangen worden ist, so tritt Freiheitsstrafe bis zu einem Jahr oder Geldstrafe ein.

(2) Straflosigkeit tritt ein, wenn der Täter die falsche Angabe rechtzeitig berichtigt. Die Vorschriften des § 158 Abs. 2 und 3 gelten entsprechend.

Para. 161 StGB (German Criminal Code): False Statutory Declarations Due to Negligence

(1) If a person commits one of the offences listed in sections 154 through 156 negligently the penalty shall be imprisonment not exceeding one year or a fine.

(2) The offender shall be exempt from liability if he or she corrects their false testimony in time. The provisions of section 158 (2) and (3) shall apply accordingly.

Die vorstehende Belehrung habe ich zur Kenntnis genommen:

I have read and understood the above official notification:

Ort, Datum/City, Date

Unterschrift/Signature